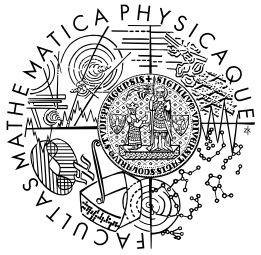

FACULTY
OF MATHEMATICS
AND PHYSICS
Charles University

DOCTORAL THESIS

Stanislav Poláček

Study of proton–proton interactions at the ATLAS experiment at CERN

Institute of Particle and Nuclear Physics

Supervisor of the doctoral thesis: Mgr. Daniel Scheirich, Ph.D
Study programme: Physics
Study branch: Particle and Nuclear Physics

Prague 2024

I declare that I carried out this doctoral thesis independently, and only with the cited sources, literature and other professional sources. It has not been used to obtain another or the same degree.

I understand that my work relates to the rights and obligations under the Act No. 121/2000 Sb., the Copyright Act, as amended, in particular the fact that the Charles University has the right to conclude a license agreement on the use of this work as a school work pursuant to Section 60 subsection 1 of the Copyright Act.

In ..... date ....

Author's signature

I want to thank Tomáš Davídek, Daniel Scheirich, and Vojtěch Pleskot for years of guidance during my studies and work on TileCal and the dijet analysis.

I thank the TileCal team for sharing their experience and knowledge with me and for their calorimeter-related help.

I thank the jet analysis group for many discussions and their work on the jet cross-section measurements.

Last, I want to thank my family, friends, my loving wife, and my two cats (both sitting next to me as I write this dedication).

Title: Study of proton–proton interactions at the ATLAS experiment at CERN

Author: Stanislav Poláček

Institute: Institute of Particle and Nuclear Physics

Supervisor: Mgr. Daniel Scheirich, Ph.D, Institute of Particle and Nuclear Physics

Abstract: The ATLAS experiment is a multi-purpose detector, recording particle collisions at the Large Hadron Collider (LHC) at CERN. It is designed to test the Standard Model of particle physics (SM) and to search for physics beyond the SM.
ATLAS consists of multiple sub-systems, one of which is the Tile Calorimeter (TileCal). TileCal is a hadronic calorimeter covering the central ATLAS region, used for measurements of energy and direction of jets and single hadrons. The time calibration of TileCal is crucial for the correct energy reconstruction, non-collision background removal, and time-of-flight measurements.
Jet measurements are important high-energy tests of quantum chromodynamics, probing the strong coupling constant and proton structure. The presented multi-differential inclusive dijet cross-section measurement uses the full LHC Run 2 dataset of 139 fb^{-1} of proton–proton collisions at the center-of-mass energy of 13 TeV. The cross-sections are measured double-differentially using the invariant dijet mass m_{jj} and either y^* or y_{boost} rapidity variables.

Keywords: CERN ATLAS TileCal QCD jet cross-section

Contents

Introduction

The ATLAS experiment is a multi-purpose detector, recording particle collisions at the Large Hadron Collider (LHC) at CERN. It is designed to test the Standard Model of particle physics (SM) and to search for physics beyond the SM.

ATLAS consists of multiple sub-systems, one of which is the ATLAS Tile Calorimeter (TileCal). TileCal is a sampling hadronic calorimeter consisting of steel absorbers and plastic scintillators, covering the central ATLAS region. It is used for measurements of energy and direction of jets and single hadrons and contributes to the missing transverse energy reconstruction, trigger systems, and muon identification.

The time calibration of TileCal is crucial for the correct energy reconstruction, non-collision background removal, and time-of-flight measurements. There are multiple methods of the time calibration, the final of which utilizes jets in proton–proton collision data.

Jet measurements are important high-energy tests of the quantum chromodynamics (QCD), probing the strong coupling constant and proton structure. The presented multi-differential inclusive dijet cross-section measurement uses the full LHC Run 2 dataset of 139 fb^{-1} of proton–proton collisions at the center-of-mass energy of 13 TeV. The cross-sections are measured double-differentially using the invariant dijet mass m_{jj} and either y^* or y_{boost} rapidity variables.

In this text, a brief introduction to QCD is presented in Chapter 1. The structure of the ATLAS experiment, including its sub-systems, is described in Chapter 2. A detailed description of TileCal is given in Chapter 3, including the signal reconstruction and the calibration and monitoring systems. The time calibration of TileCal, including the author's contributions, is described in Section 3.4. The reconstruction of jets and the methods of their calibration are explained in Chapter 4. The current state of the dijet analysis is summarised in Chapter 5, presenting the author's contributions to the measurement.

1. Theoretical background

The Standard Model of particle physics (SM) is a SU(3)×SU(2)×U(1) gauge field theory, describing all known elementary particles and their interactions. The SU(2)×U(1) part corresponds to the electroweak (EW) theory, describing interactions of particles with photons and with intermediate bosons $W^{\pm}$ and Z [1]. The SU(3) part corresponds to the quantum chromodynamics (QCD)—theory describing the strong interaction of color-charged massive quarks mediated by mass-less gluons.

The following sections are based on Ref. [2–4].

1.1 Quantum chromodynamics

The QCD describes interactions of quarks and gluons. Quarks are massive spin 1/2 fermions. There are six quark flavors—up (u), charm (c), and top (t) carrying an electric charge of $+2/3$ e and down (d), strange (s), and bottom (b) with $-1/3$ e, where e is the elementary charge. Quark masses range from $m_u = 2.16^{+0.49}_{-0.26}$ MeV to $m_t = 172.69 \pm 0.30$ GeV [5].

Gluons are mass-less spin 1 bosons without an electric charge. Both quarks and gluons carry a color charge and therefore can interact via the strong interaction, exchanging the color charges. There are three quark colors—red, green, and blue—and three corresponding anticolors of antiquarks. Eight types of gluons correspond to eight non-singlet (with respect to the SU(3) group) color–anticolor states.

1.1.1 QCD Lagrangian

The Lagrangian density of QCD is

$$\mathcal{L}_{\mathrm{QCD}} = -\frac{1}{4} F^a_{\mu\nu} F^{a\,\mu\nu} + \bar{\psi}_q \left(i\gamma^\mu D_\mu - m_q \right) \psi_q, \tag{1.1}$$

where $F^a_{\mu\nu}$ is a gluon field strength tensor with color index $a \in [1, \ldots, 8]$, ψ_q is a quark field with flavor index q ($\bar{\psi}_q$ denotes a Dirac adjoint defined for example in Ref. [1]), γ_μ are Dirac matrices (defined for example in Ref. [1]), D_μ is a covariant derivative and m_q is a quark mass.

The gluon field strength tensor is defined as

$$F^a_{\mu\nu} = \partial_\mu A^a_\nu - \partial_\nu A^a_\mu + g_{\mathrm{S}} f^{abc} A^b_\mu A^c_\nu, \tag{1.2}$$

where A^a_μ is a gluon field, g_{S} is a strong coupling constant, and f^{abc} are fully antisymmetric SU(3) structure constants [3]. Alternatively to the g_{S} as the strong coupling constant,

$$\alpha_{\mathrm{S}} = \frac{g_{\mathrm{S}}^2}{4\pi}$$

is also used.

In QCD, the covariant derivative D_μ takes form of

$$D_\mu = \partial_\mu - i g_{\mathrm{S}} T^a A^a_\mu, \tag{1.3}$$

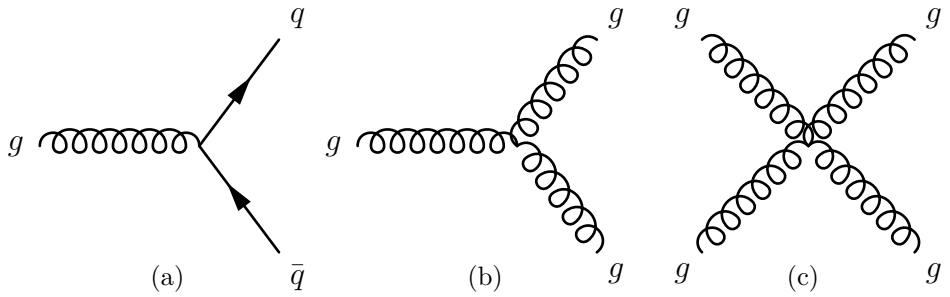

Figure 1.1: Feynman diagrams of (a) quark–gluon interaction and self-interactions of (b) three and (c) four gluons.

where T^a are eight generators of the SU(3) group. Quark fields

$$\psi_q = \begin{pmatrix} \psi_{q_\mathrm{R}} \\ \psi_{q_\mathrm{G}} \\ \psi_{q_\mathrm{B}} \end{pmatrix}$$

are triplets with respect to the SU(3) group. The R, G, and B indices denote the quark color charge.

Using the definition of the covariant derivative D_μ from Equation (1.3) and the gluon field density tensor $F^a_{\mu\nu}$ from Equation (1.2), the QCD Lagrangian density from Equation (1.1) written in terms of gluon fields A^a contains the kinetic term of the gluon fields

$$-\frac{1}{4}\left(\partial_\mu A^a_\nu - \partial_\nu A^a_\mu\right)\left(\partial^\mu A^{a\,\nu} - \partial^\nu A^{a\,\mu}\right),$$

the kinetic and mass terms of the quark field

$$\bar{\psi_q}\left(i\gamma^\mu\partial_\mu - m_q\right)\psi_q,$$

the quark–gluon interaction term (Figure 1.1a)

$$g_\mathrm{S}\bar{\psi_q}T^a\psi_q A^a_\mu,$$

and self-interaction terms of three and four gluons (Figures 1.1b and 1.1c)

$$-\frac{g_\mathrm{S}}{2}f^{abc}\left(\partial_\mu A^a_\nu - \partial_\nu A^a_\mu\right)A^{b\,\mu}A^{c\,\nu} - \frac{{g_\mathrm{S}}^2}{4}f^{abc}f^{ade}A^{b\,\mu}A^{c\,\nu}A^d_\mu A^e_\nu.$$

1.1.2 Running of coupling constant

Besides the quark masses m_q, the only free parameter of the QCD Lagrangian is the coupling constant α_S. Using the bare quantities m_q and α_S leads to ultraviolet (UV) divergences in higher orders of the perturbative QCD (pQCD) coming from loop contributions integrated over high momenta of the virtual particles. The renormalization procedure used to deal with the UV divergences effectively introduces renormalized quantities $m_q(\mu^2_\mathrm{R})$ and $\alpha_\mathrm{S}(\mu^2_\mathrm{R})$ dependent on a renormalization scale μ_R. In the case of coupling constant, the scale dependence is given by a renormalization group equation

$$\frac{\partial\alpha_\mathrm{S}(\mu^2_\mathrm{R})}{\partial\ln\mu^2_\mathrm{R}} = \beta(\alpha_\mathrm{S}) = b_0\alpha^2_\mathrm{S} + b_1\alpha^3_\mathrm{S} + b_2\alpha^4_\mathrm{S} + \ldots, \tag{1.4}$$

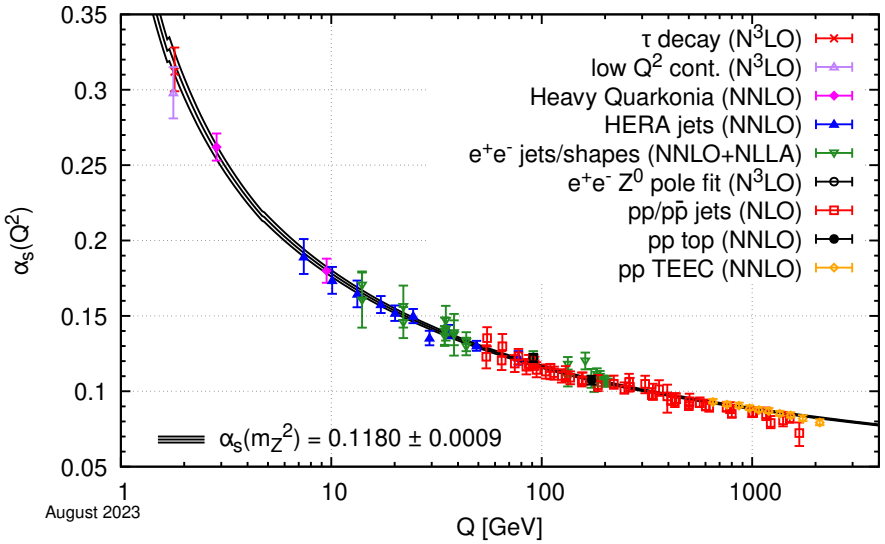

Figure 1.2: Strong coupling constant α_S determined using various experiments as a function of energy scale Q [5].

where $\beta(\alpha_S)$ function is written as an expansion in α_S using b_i, $i = 0, 1, \ldots$ coefficients (corresponding to the $i+1$-loop contributions). The b_i coefficients are theory-dependent. In the case of QCD, the 1-loop coefficient is

$$b_0 = -\frac{11N_C - 2n_f}{12\pi}, \tag{1.5}$$

where $N_C = 3$ is the number of colors and n_f is the number of quark flavors. The first term comes from gluon loops and the second from quark loops. The number n_f corresponds to the effective number of quark flavors available at a given energy scale, starting at $n_f = 3$ and increasing at charm, bottom, and top thresholds up to full $n_f = 6$.

The solution of Equation (1.4) at the leading order (LO) in the α_S expansion (in the sense of using only the b_0 term) is

$$\alpha_S(\mu_R^2) = \frac{1}{b_0 \ln \frac{\Lambda^2}{\mu_R^2}},$$

where $\Lambda \sim 200$ MeV is an integration constant representing the scale at which the perturbative coupling diverges. Thanks to the negative value of the b_0 coefficient from Equation (1.5), $\lim_{\mu_R \to \infty} \alpha_S(\mu_R^2) = 0$, resulting in asymptotic freedom—coupling constant gets weak at large energy scale.

The strong coupling constant is usually presented at a reference scale of Z boson mass $\alpha_S(m_Z^2) = 0.1180 \pm 0.0009$ [5]. Using

$$\alpha_S(Q^2) = \frac{\alpha_S(m_Z^2)}{1 - b_0 \alpha_S(m_Z^2) \ln(\frac{Q^2}{m_Z^2}) + \mathcal{O}(\alpha_S^2)},$$

the α_S can be evaluated at a different scale Q. It is measured at different scales (Figure 1.2), ranging from a few GeV using τ decays ($\alpha_S(m_\tau^2) \approx 0.3$) to a TeV scale using hadron colliders ($\alpha_S(1\ \text{TeV}^2) \approx 0.09$).

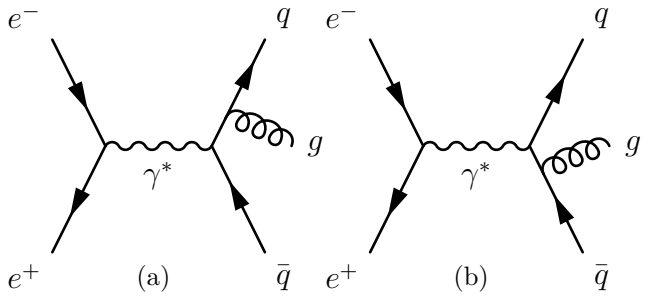

Figure 1.3: Tree-level Feynman diagrams of $e^+e^- \to q\bar{q}g$ process.

1.1.3 Mass singularities

Besides the UV divergences coming from loop contributions to the pQCD, the pQCD contains also infrared (IR) divergences originating from emissions of zero-mass gluons. This can be illustrated using a $e^+e^- \to q\bar{q}g$ process (Figures 1.3a and 1.3b). The cross-section of the process is

$$\frac{\mathrm{d}\sigma}{\mathrm{d}x_1\mathrm{d}x_2} = \sigma_0 \frac{4}{3}\frac{\alpha_\mathrm{S}}{2\pi}\frac{x_1^2 + x_2^2}{(1-x_1)(1-x_2)}, \tag{1.6}$$

where

$$\sigma_0 = 3\frac{4\pi}{3}\frac{\alpha_\mathrm{S}^2}{s}e_q^2$$

is the cross-section of the $e^+e^- \to q\bar{q}$ production of quark–antiquark pair with charge e_q at the center-of-mass energy of $\sqrt{s}$. The $x_i, i = 1, 2$ are dimensionless fractions defined as

$$x_i = \frac{2E_i}{\sqrt{s}},$$

where E_1 and E_2 are the quark and antiquark energies in the center-of-mass system, respectively.

The cross-section from Equation (1.6) contains two types of divergences for colinear gluon emissions—$x_1 \to 1$ ($x_2 \to 1$) corresponds to a gluon emission in parallel with the outgoing antiquark (quark)—and for soft gluon emissions $x_1 = x_2 = 1$ where the gluon energy vanishes, which can be regularized for example by introduction of a non-zero gluon mass.

Besides emissions of real gluons, the same type of IR divergences appear even in the contributions of virtual gluons in loops. The Kinoshita–Lee–Nauenberg (KLN) theorem [6–8] ensures cancellation of the IR divergences in the cross-section when summing over all degenerate states—the final states of $e^+e^- \to q\bar{q}$ and $e^+e^- \to q\bar{q}g$ are experimentally indistinguishable if the gluon is parallel to the quark (or antiquark) or has very small energy.

Defining the invariant antiquark–gluon mass

$$Q^2 = s(1-x_1),$$

Equation (1.6) can be rewritten in a colinear limit $x_1 \to 1$ as

$$\frac{\mathrm{d}\sigma}{\mathrm{d}x_2\mathrm{d}Q^2} = \sigma_0 \frac{\alpha_\mathrm{S}}{2\pi}\frac{1}{Q^2}P_{qq}^{(0)}(x_2),$$

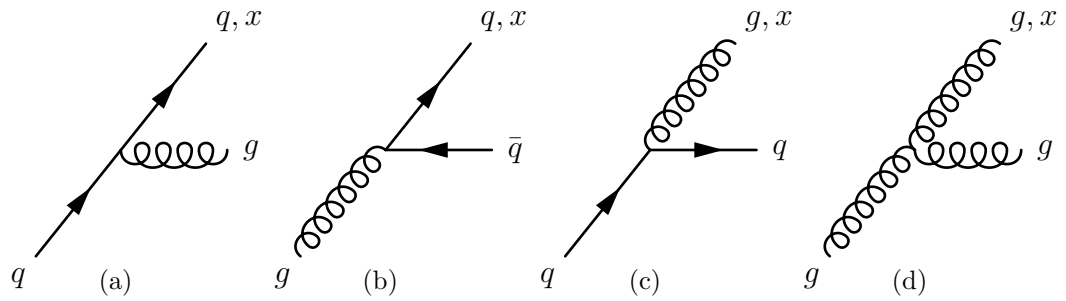

Figure 1.4: Quark and gluon emissions corresponding to the (a) $P_{qq}^{(0)}(x)$, (b) $P_{qg}^{(0)}(x)$, (c) $P_{gq}^{(0)}(x)$, and (d) $P_{gg}^{(0)}(x)$ splitting functions. The parton carries the energy fraction x after the splitting.

where

$$P_{qq}^{(0)}(x) = P_{\bar{q}\bar{q}}^{(0)}(x) = \frac{4}{3}\frac{1+x^2}{1-x}$$

is the LO quark–quark splitting function [9], describing the gluon emission from a quark or an antiquark (Figure 1.4a). Analogously, other splitting functions $P_{qg}^{(0)}(x) = P_{\bar{q}g}^{(0)}(x)$, $P_{gq}^{(0)}(x) = P_{g\bar{q}}^{(0)}(x)$, and $P_{gg}^{(0)}(x)$ are defined to describe other possible quark or gluon emissions (Figures 1.4b to 1.4d).

1.1.4 Parton distribution functions

The proton structure is described using parton distribution functions (PDFs)—distribution functions $q(x, \mu_{\mathrm{F}}^2)$ ($g(x, \mu_{\mathrm{F}}^2)$) of probability to find a quark (gluon) in a proton, carrying a fraction $x = p_{\mathrm{parton}}/p_{\mathrm{proton}}$ of proton's momentum. The PDFs are connected with parton dynamics inside the proton and they cannot be calculated using the pQCD and must be determined experimentally (Figure 1.5). Nevertheless, the dependence of PDFs on a factorization scale μ_{F} comes from a parton emission (Figure 1.6) and can be derived in terms of the pQCD.

Using the splitting functions described in Section 1.1.3, the dependence of quark, antiquark, and gluon distribution functions (q, $\bar{q}$, and g) takes the form of Dokshitzer–Gribov–Lipatov–Altarelli–Parisi (DGLAP) evolution equations

$$\frac{\partial q(x,\mu_{\mathrm{F}}^2)}{\partial \ln \mu_{\mathrm{F}}^2} = \frac{\alpha_{\mathrm{S}}(\mu_{\mathrm{F}}^2)}{2\pi}\int_x^1 \frac{dy}{y}\left[q(y,\mu_{\mathrm{F}}^2)P_{qq}^{(0)}\left(\frac{x}{y}\right) + g(y,\mu_{\mathrm{F}}^2)P_{qg}^{(0)}\left(\frac{x}{y}\right)\right],$$

$$\frac{\partial \bar{q}(x,\mu_{\mathrm{F}}^2)}{\partial \ln \mu_{\mathrm{F}}^2} = \frac{\alpha_{\mathrm{S}}(\mu_{\mathrm{F}}^2)}{2\pi}\int_x^1 \frac{dy}{y}\left[\bar{q}(y,\mu_{\mathrm{F}}^2)P_{qq}^{(0)}\left(\frac{x}{y}\right) + g(y,\mu_{\mathrm{F}}^2)P_{qg}^{(0)}\left(\frac{x}{y}\right)\right],$$

$$\frac{\partial g(x,\mu_{\mathrm{F}}^2)}{\partial \ln \mu_{\mathrm{F}}^2} = \frac{\alpha_{\mathrm{S}}(\mu_{\mathrm{F}}^2)}{2\pi}\int_x^1 \frac{dy}{y}\left[g(y,\mu_{\mathrm{F}}^2)P_{gg}^{(0)}\left(\frac{x}{y}\right) + \sum_{q,\bar{q}}\left(q(y,\mu_{\mathrm{F}}^2) + \bar{q}(y,\mu_{\mathrm{F}}^2)\right)P_{gq}^{(0)}\left(\frac{x}{y}\right)\right].$$

1.1.5 Hadronization

After the hard-scattering process, which is calculable within the framework of the pQCD, the final state partons are quickly converted into hadrons—the hadronization happens on a scale of roughly ~ 1 fm ($\sim 10^{-24}$ s) [10]. The non-perturbative process of hadronization is described using phenomenological models.

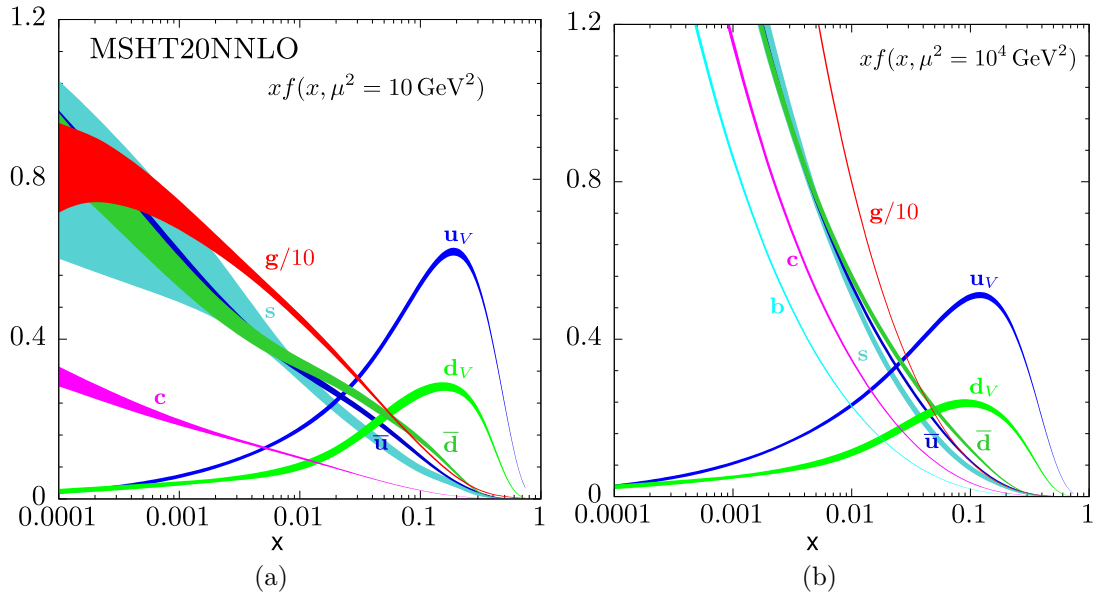

Figure 1.5: The PDFs multiplied by x for different partons ($u_{\rm V} = u - \bar{u}$, $d_{\rm V} = d - \bar{d}$, $\bar{u}$, $\bar{d}$, $s \simeq \bar{s}$, $c = \bar{c}$, $d = \bar{d}$, g) as a function of x for two scales (a) $\mu_{\rm F}^2 = 10$ GeV^2 and (b) $\mu_{\rm F}^2 = 10^4$ GeV^2.

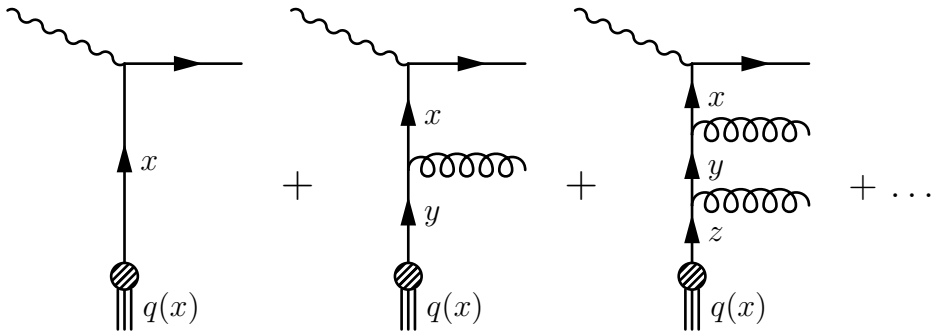

Figure 1.6: Gluon emissions resulting in the factorization scale $\mu_{\rm F}$ dependence of the initially bare PDF $q(x)$. The x, y, and z denote the fractions of the proton's momentum carried by the quark.

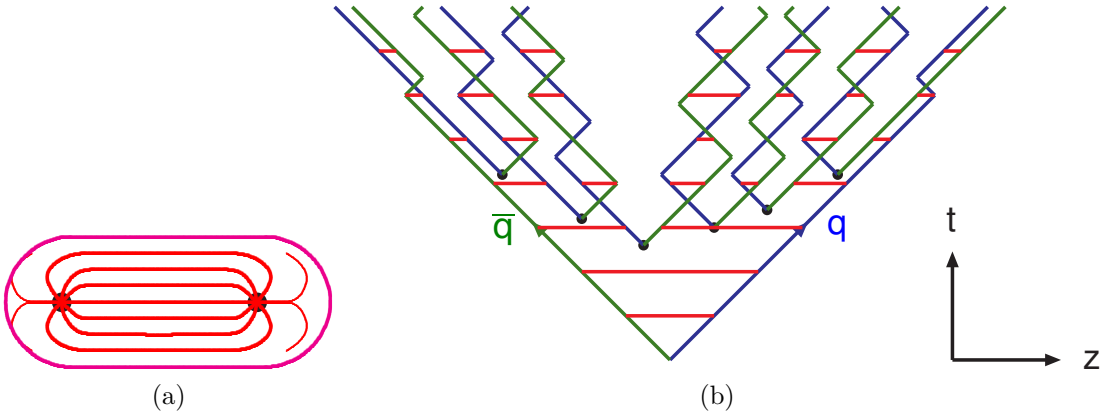

(a) (b)

Figure 1.7: (a) The field lines of the effective QCD potential and (b) particle production in the string fragmentation model [14]. The (massless) quarks evolve in time t, oscillating in a z direction.

An example of such a model is the Lund string fragmentation [11], used for example in the PYTHIA Monte Carlo (MC) generator [12]. The effective QCD potential of a quark–antiquark pair interaction separated by distance r

$$V_{\mathrm{QCD}}^{\mathrm{eff}} = V_{\mathrm{C}}(\alpha_{\mathrm{S}}) + \kappa r \tag{1.7}$$

consists of a Coulombic term

$$V_{\mathrm{C}}(\alpha_{\mathrm{S}}) \propto -\frac{\alpha_{\mathrm{S}}}{r},$$

connected with the internal structure of hadrons, and a linear term κr, connected with free-quark dynamics, where $\kappa \approx 1$ GeV/fm [2]. The field lines of the interaction correspond to a thin string with the energy density κ (Figure 1.7a). Under this tension, the quark and antiquark oscillate with a string stretched between them. As the string stretches, the energy stored in it linearly increases with the q–$\bar{q}$ distance according to Equation (1.7). In the string fragmentation model, the string may break, producing a new q–$\bar{q}$ pair (Figure 1.7b)—the production of heavy quarks is exponentially suppressed according to their mass. This process continues until no more pair production is possible and the close quarks and antiquarks are combined to form mesons—the meson mass corresponds to the invariant mass of the q–$\bar{q}$ system. The model can be modified to describe baryon production—for example, a q–$\bar{q}$ pair can be created on the string as a vacuum fluctuation without it breaking [13].

2. The ATLAS experiment

With a circumference of approximately 27 km, the Large Hadron Collider (LHC) [15] is the largest particle accelerator at the CERN laboratory.

Before protons can be accelerated in the LHC, they go through the injector chain composed of multiple smaller accelerators (Figure 2.1). During the Run 2 data taking (2015–2018), hydrogen atoms were stripped of electrons using an electric field. The resulting protons then passed through the Linear accelerator 2 (Linac2) and multiple circular accelerators—the Proton Synchrotron Booster (PSB), Proton Synchrotron (PS), and Super Proton Synchrotron (SPS)—gradually increasing their energy to the final value of 450 GeV, at which point they were injected into the LHC and further accelerated.

During Run 2, bunches of approximately 10^{11} protons were accelerated to the energy of 6.5 TeV per beam, corresponding to collisions at the center-of-mass energy of 13 TeV with maximum instantaneous luminosity at the level of 2×10^{34} cm^{-2}s^{-1}. In between years 2015–2018, the LHC delivered approximately 160 fb^{-1} of integrated luminosity of proton–proton (p–p) collision data.

2.1 ATLAS

A Toroidal LHC ApparatuS (ATLAS) experiment (Figure 2.2) [17] is one of four main detectors positioned around the LHC. It is a multi-purpose detector designed to test the Standard Model of particle physics (SM) and to search for new physics beyond the SM.

The following coordinate system [17] is used to describe the ATLAS experiment. The nominal interaction point (IP) of the LHC defines the coordinate system origin. The x–y plane is transverse to the beam direction, where the x-axis points towards the center of the LHC ring and the y-axis points upwards. The z-axis coincides with the beam direction, pointing counter-clockwise. The azimuthal angle ϕ is measured in the x–y plane around the z-axis. The pseudo-rapidity

$$\eta = -\ln \tan(\theta/2)$$

is usually used instead of the polar angle θ. It is equal to the massless limit of the rapidity

$$y = \frac{1}{2} \ln \frac{E + p_z}{E - p_z},$$

where E is the energy of a particle and p_z is its momentum along the z-axis. The angular distance of two particles i and j is measured using

$$\Delta R_{ij} = \sqrt{{\Delta\eta_{ij}}^2 + {\Delta\phi_{ij}}^2}, \tag{2.1}$$

where $\Delta\eta_{ij}$ and $\Delta\phi_{ij}$ are their η and ϕ separations. Both $\Delta\phi_{ij}$ and Δy_{ij} (and therefore even $\Delta\eta_{ij}$ and ΔR_{ij} in the massless limit) are Lorentz invariant under boosts in the direction of the z-axis. All transverse variables (like the transverse energy E_{T} and momentum p_{T}) are defined as a projection of the corresponding variable to the x–y plane.

ATLAS consists of multiple specialized sub-systems, each measuring specific aspects of the LHC collisions.

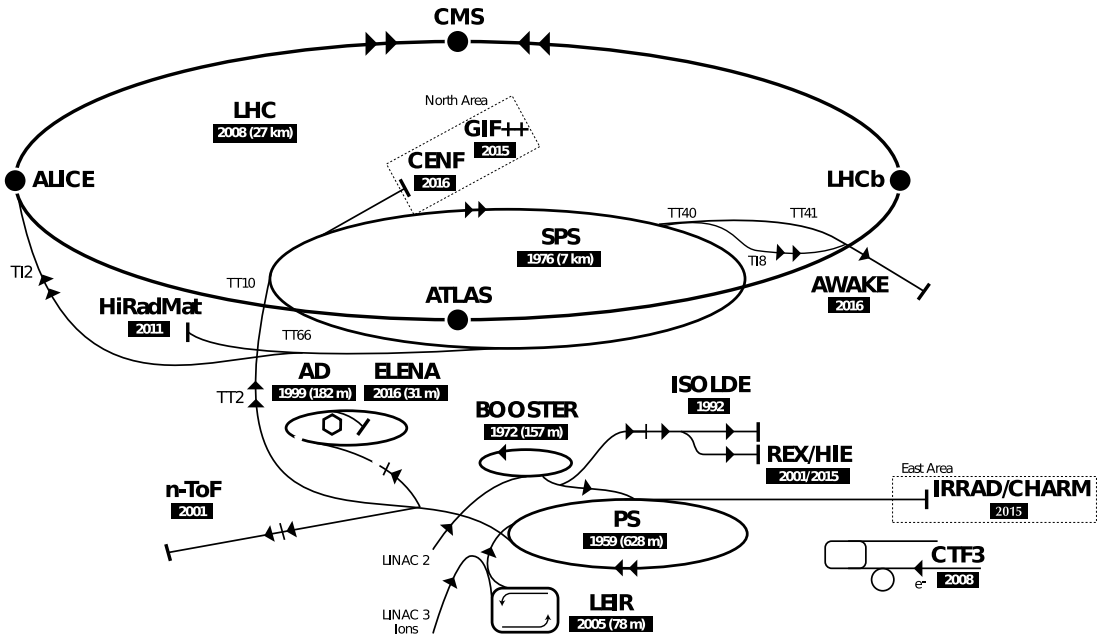

Figure 2.1: The accelerator complex at CERN during the LHC Run 2 [16].

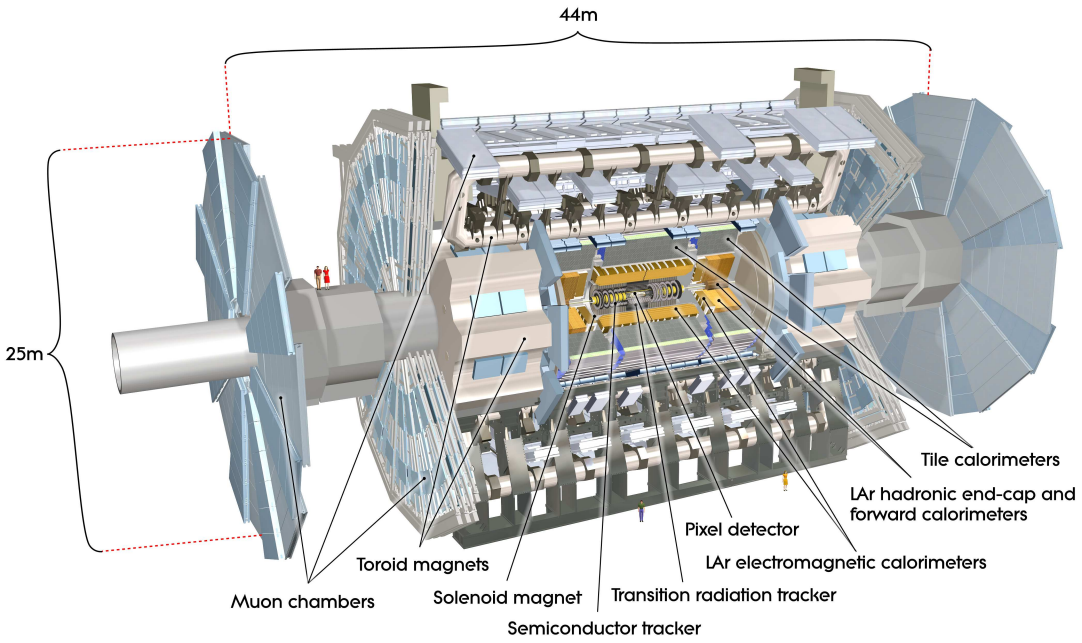

Figure 2.2: The ATLAS experiment [17].

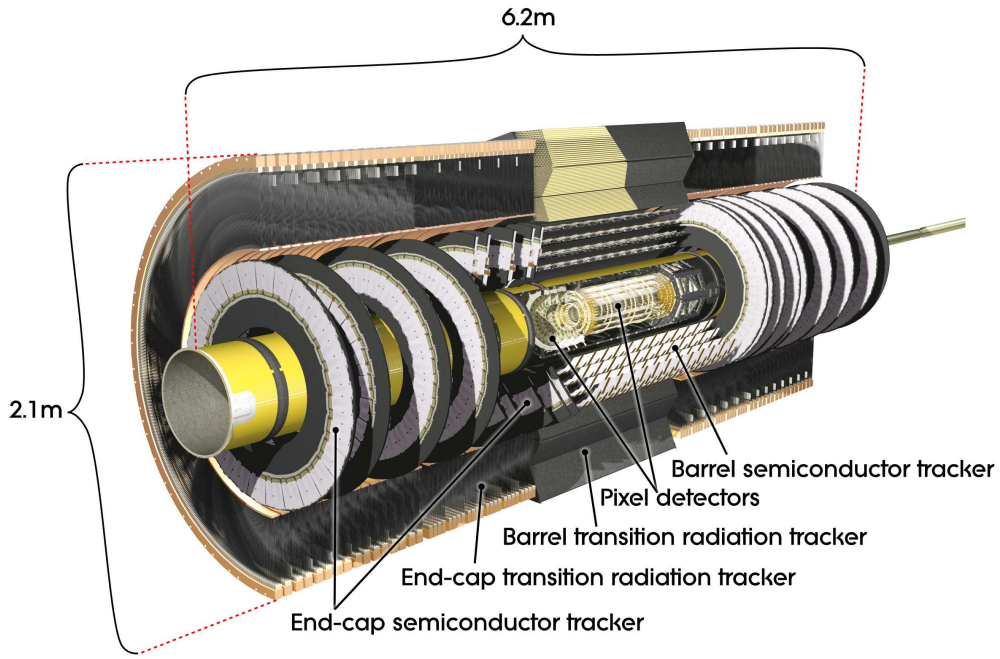

Figure 2.3: The Inner Detector of the ATLAS experiment [17].

2.1.1 Inner Detector

The ATLAS Inner Detector (ID) [18–20] (Figure 2.3) directly surrounds the ATLAS IP and covers the pseudorapidity range of $|\eta| < 2.5$. It is immersed in the 2 T axial magnetic field provided by the superconducting solenoid magnet (Figure 2.2) [21–23]. The purpose of the ID is to reconstruct tracks of charged particles passing through the detector. The tracks are used to reconstruct interaction vertices and transverse momenta p_{T} of particles, with designed resolution of $\sigma(p_{\mathrm{T}})/p_{\mathrm{T}} = 0.05\% \cdot p_{\mathrm{T}} \oplus 1\%$, where momentum p_{T} is in GeV and $\oplus$ denotes a quadratic sum [17].

The ID consists of three parts—Pixel Detector, Semiconductor Tracker (SCT), and Transition Radiation Tracker (TRT).

The Pixel Detector is the innermost component of the ID. It is made of silicon pixels arranged into four coaxial cylinders in the central region (including the insertable B-layer (IBL) upgrade for Run 2 [24]) and three disks in each end cap. It has the highest granularity of the ID components with 50×250 $\mu\mathrm{m}^2$ pixels in the IBL layer and 50×400 $\mu\mathrm{m}^2$ pixels in the remaining layers [20].

The SCT is made of silicon strips arranged similarly as in the case of the Pixel Detector—into four coaxial cylinders in the central region and nine disks in each end cap [20].

The TRT is the outermost component of the ID, consisting of gas-filled drift tubes. Besides the tracking measurements, the electron identification is enhanced using the detection of the transition radiation.

2.1.2 Calorimeters

Calorimeters of the ATLAS experiment (Figure 2.4) are designed to absorb most of the particles produced in the LHC collisions, measuring their energy and di-

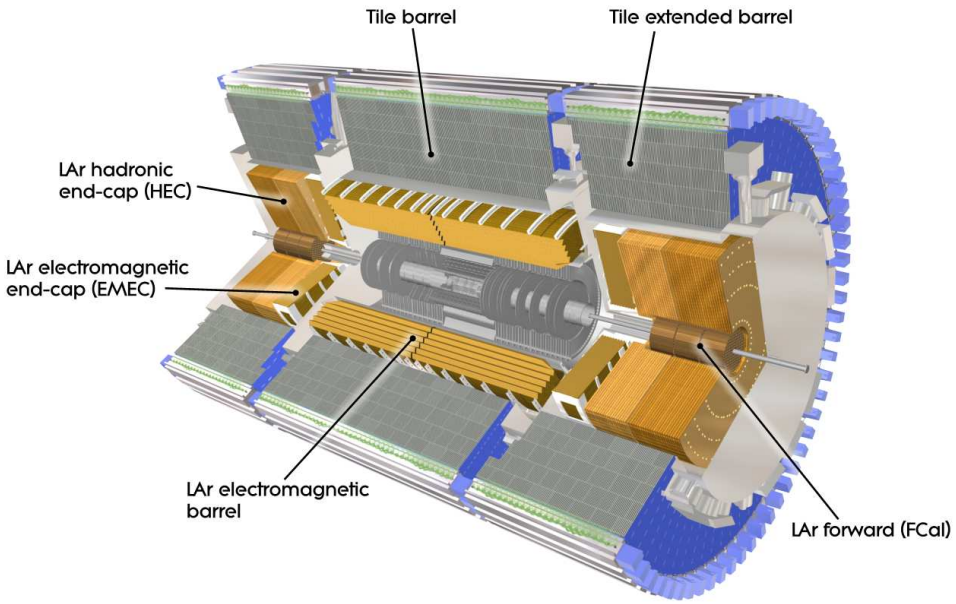

Figure 2.4: Calorimeters of the ATLAS experiment [17].

rection of travel. The calorimeter system consists of electromagnetic (EM) and hadronic calorimeters, covering the pseudorapidity range of $|\eta| < 4.9$ [17]. EM calorimeters measure the energy of electrons and photons and hadronic calorimeters (with a contribution of EM ones) focus on jet measurements. All of the ATLAS calorimeters are sampling calorimeters. They consist of alternating layers of a passive absorber material, in which particles interact, developing particle showers, and layers of an active medium, sampling the energy of particles.

The Liquid Argon Calorimeter (LAr) calorimeter [25, 26] uses liquid argon as an active medium. It consists of a high-granularity EM calorimeter—divided into the Electromagnetic Barrel (EMB) and Electromagnetic End-Cap (EMEC)—with lead absorbers (covering the $|\eta| < 3.2$ region), the Hadronic End-Cap (HEC) with copper absorbers in the end-cap region ($1.5 < |\eta| < 3.2$), and the Forward Calorimeter (FCal) with copper and tungsten absorbers in the forward region ($3.1 < |\eta| < 4.9$). The energy resolution $\sigma(E)/E$ is designed to be $10\%/\sqrt{E} \oplus 0.7\%$ in the EM calorimeter, $50\%/\sqrt{E} \oplus 3\%$ in HEC, and $100\%/\sqrt{E} \oplus 10\%$ in FCal, where energy E is in GeV and $\oplus$ denotes a quadratic sum [17].

The Tile Calorimeter (TileCal) is described in detail in Chapter 3.

2.1.3 Muon Spectrometer

The Muon Spectrometer (MS) (Figure 2.2) [27] forms the outermost layer of the ATLAS experiment, covering the pseudorapidity range of $|\eta| < 2.7$. It consists of a magnet system—three superconducting toroids [21, 22], one in the barrel region [28] and two in the end-cap regions [29]—and multiple types of tracking chambers used for precision measurements and triggering. It is designed to reconstruct tracks and transverse momenta of muons that pass through the inner layers of ATLAS. The relative momentum resolution of the MS is approximately 2–3% over most of the kinematic range, increasing to approximately 10% at the muon

transverse momentum $p_{\mathrm{T}} = 1$ TeV [27].

2.1.4 Forward detectors

In addition, there are four smaller detectors in the ATLAS forward region.

The LUminosity Cherenkov Integrating Detector (LUCID) [30] consists of two modules located around the LHC beam pipe in a distance of ±17 m from the ATLAS IP. It measures the integrated luminosity delivered to ATLAS and monitors the instantaneous luminosity and beam conditions using the inelastic p–p collisions in the forward region.

The Zero Degree Calorimeter (ZDC) [17] is located in between the two LHC beam pipes in a distance of ±140 m from the IP, covering the pseudorapidity range of $|\eta| > 8.3$. It consists of four modules—one EM and three hadronic—at each side. ZDC is used to detect neutrons and other neutral particles in the far forward region, mainly to determine the centrality of the heavy ion collisions.

The ATLAS Forward Proton (AFP) [31, 32] is located around the LHC beam pipe approximately ±210 m from the IP. It consists of two detectors at each side of the IP, containing silicone trackers and time-of-flight detectors. AFP is used to measure elastic and diffractive p–p scattering in standard p–p collision runs.

The Absolute Luminosity For ATLAS (ALFA) [17, 33] was located around the LHC beam pipe approximately ±240 m from the IP. It consisted of two detectors at each side of the IP. ALFA was used to measure elastic p–p scattering during special runs and was decommissioned after the 2023 data-taking period.

2.1.5 Trigger system

Due to a very high collision rate of 40 MHz at LHC, it is not possible to record all of the events. The trigger system [34, 35] is responsible for selecting events of interest that are kept for further analysis, effectively reducing the initial event rate to a manageable level. The trigger system consists of two levels—the Level-1 (L1) trigger and High-Level Trigger (HLT).

The hardware-based L1 trigger uses reduced information from calorimeters and muon detectors. Events are kept based on the presence of objects like muons or jets with large transverse momenta, or large total or missing transverse energy in the calorimeters. The L1 trigger reduces the event rate to a maximum detector read-out rate of 100 kHz with a latency of 2.5 µs. It also provides regions of interest to be investigated by the next level of the trigger system—the HLT.

The HLT is software-based. Events selected by the L1 trigger are reconstructed online in more detail than at L1, using dedicated reconstruction algorithms. The HLT makes a decision within a few hundred µs, reducing the event rate on average to 1.2 kHz during Run 2 [35] and approximately 3 kHz during Run 3 [36]. Events accepted by the HLT are stored for the full offline reconstruction.

3. The ATLAS Tile Calorimeter

The Tile Calorimeter (TileCal) [17, 37] is the central hadronic calorimeter of the ATLAS experiment. TileCal plays a major role in the identification of hadronic jets and single hadrons and the measurement of their energy and direction of travel. It also contributes to the missing transverse energy reconstruction, ATLAS trigger systems, and muon identification.

3.1 Calorimeter structure

TileCal has the shape of three hollow cylinders directly surrounding the Liquid Argon Calorimeter (Figure 2.4)—the long barrel in the center and two extended barrels at its sides. The long barrel with its length of 5.8 m covers the pseudorapidity region of $|\eta| < 1.0$. It is divided into two halves—LBA and LBC—the A (C) side being the one with the positive (negative) z-coordinate. Both extended barrels—EBA and EBC—are 2.6 m long and cover a pseudorapidity region of $0.8 < |\eta| < 1.7$. All barrels have an inner radius of 2.28 m and outer radius of 4.23 m and are divided into 64 modules in the angular direction ϕ [17] (Figures 3.1a and 3.1b).

Each module consists of 11 rows of 3 mm thick plastic scintillator tiles, periodically arranged inside a steel absorber structure [38] (Figure 3.1a). Charged particles traversing the tiles produce an ultraviolet scintillation light that is converted into a visible spectrum (blue light). The wavelength-shifting (WLS) fibers collect the light from exposed edges of the tiles, shifting it further to a longer wavelength (yellow-green light) and transporting it to photomultiplier tubes (PMTs) located in steel support girders at the outer radii of the calorimeter modules (Figure 3.1a).

Groupings of WLS fibers to the same PMTs define the TileCal readout cells. There are three rows of standard readout cells (Figure 3.2) of variable sizes—A, BC, and D in the long barrel (corresponding to three, six, and two rows of scintillator tiles, respectively) and A, B, and D in extended barrels (three, four, and four rows of tiles) [38]. The dimensions of cells in $\Delta\eta \times \Delta\phi$ ($\Delta\phi$ is given by the module thickness) are approximately 0.1×0.1 in the two inner layers and 0.2×0.1 in the outermost layer. In the transitional region between the long and extended barrels, there are smaller D4 and C10 cells and gap (E1, E2) and crack (E3, E4) scintillators. Cells are usually connected to two PMTs, resulting in 9852 readout channels for 5182 cells [38].

Using isolated pions, the standalone energy resolution of TileCal was measured to be

$$\frac{\sigma(E)}{E} = \frac{56.4\%}{\sqrt{E}} \oplus 5.5\%,$$

where the first term corresponds to stochastic fluctuations of the energy deposited in the active environment of the calorimeter, the second term corresponds to the cell response non-uniformity, energy E is in GeV, and $\oplus$ denotes a quadratic sum [17].

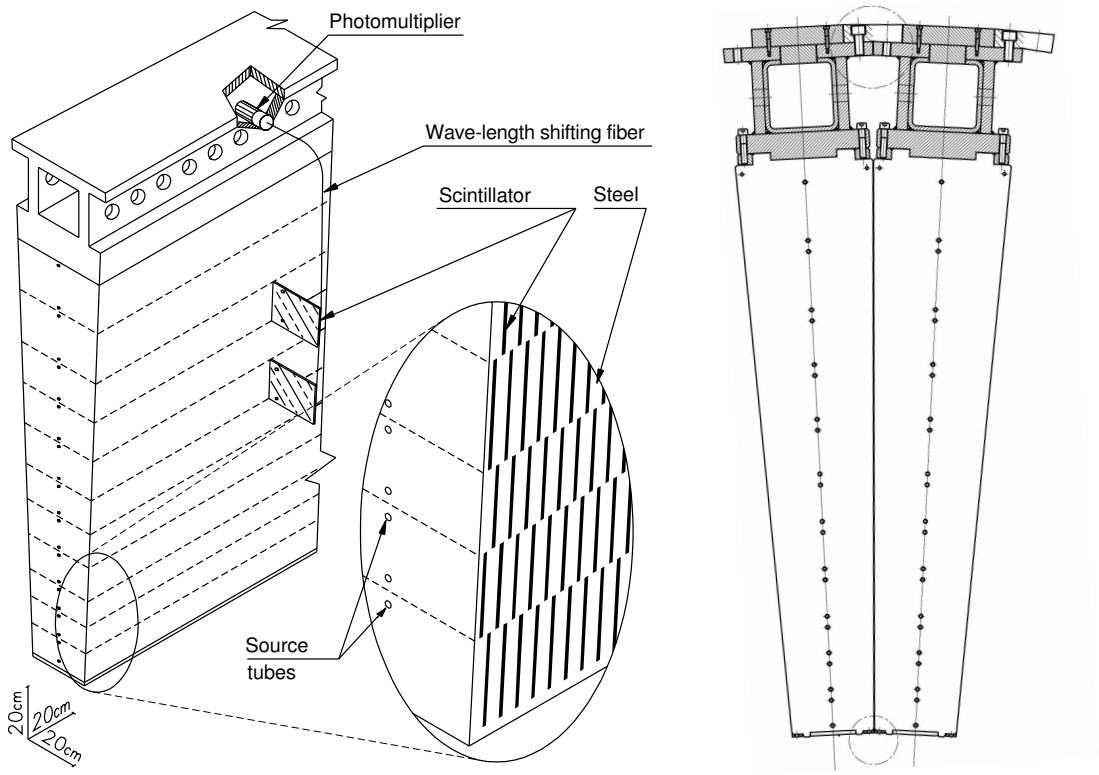

Figure 3.1: Schematics of (a) a TileCal module, displaying 11 rows of the scintillator tiles (dashed lines) and other optical readout components, and (b) a connection of two modules in the azimuthal plane [17].

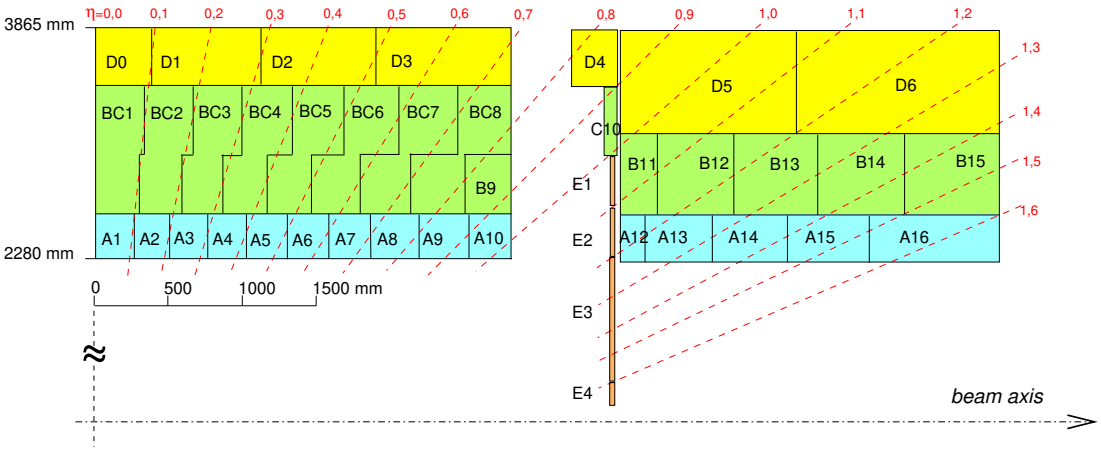

Figure 3.2: Three rows of readout cells (A, B/BC, and D) and special D4, C10, and E cells of TileCal displayed in half of a module of the long barrel and a module of the extended barrel, as used in Run 3 [39].

3.2 Signal reconstruction

Particles traveling through the calorimeter interact with the steel-absorber plates, developing a particle shower. A light produced in the scintillator tiles by charged shower components is transported by the WLS fibers to the PMTs, which are (together with the readout electronics) located at the outer sides of the calorimeter modules.

3.2.1 Readout electronics

The front-end electronics components of TileCal are housed in removable aluminum super-drawers in the steel girders of each module. In both (A and C) sides of the long barrel modules and each of the extended barrel modules there is one super-drawer, which contains 45 (32) readout channels in the long (extended) barrel [38].

Each channel consists of a PMT block, containing a light mixer, PMT, high-voltage divider, and 3-in-1 card [40–42]. The light mixer provides uniform illumination of the photocathode of the PMT by mixing the light from the corresponding readout fibers. In the 3-in-1 card, the electric pulse signal of the PMT is shaped to have a constant width and divided into two branches—high gain (HG) and low gain (LG)—in which it is amplified with a relative gain ratio of 64:1. Additionally, the 3-in-1 card provides a signal to the integrator readout (averaging the signal over 10–20 ms, used by calibration and monitoring systems, Section 3.3) and contains an input path for the charge injection system (CIS) (Section 3.3.3).

The HG and LG signals are sent to a digitizer system [43]. The digitizer samples the pulse every 25 ns using two 10-bit analog-to-digital converters (ADCs) (one for each gain, effectively providing a 16-bit dynamic range). The sampled values are stored in a pipeline memory and in the case of Level-1 (L1) trigger accept, they are sent to an off-detector readout driver (ROD) system. Each super-drawer contains eight digitizer boards, each servicing up to six channels. The digitizer board contains two data management units (DMUs), each processing signal from up to three channels. The LHC clock, L1 trigger decisions, and configuration commands are distributed via the ATLAS timing, trigger, and control (TTC) system to a TTC receiver chip (TTCrx) in each digitizer board.

The back-end electronics (located outside of the detector in the main services cavern USA15) consist of the ROD and TTC systems. The ROD system contains digital signal processor (DSP) chips, which reconstruct the deposited energy and the timing information in each cell in real time (online) using the optimal filtering (OF) algorithm (Section 3.2.2). The DSP energy and time are provided to the ATLAS High-Level Trigger.

3.2.2 Optimal filtering algorithm

The OF algorithm [44] is used to reconstruct the signal parameters from the seven ADC samples $S_i, i = 1, \ldots, 7$ centered around the expected pulse peak

$$A = \sum_{i=1}^{7} a_i S_i, \qquad t = \frac{1}{A} \sum_{i=1}^{7} b_i S_i, \qquad P = \sum_{i=1}^{7} c_i S_i, \tag{3.1}$$

where A is the signal amplitude in the ADC counts, t is the time phase relative to the expected signal peak, P is the pedestal, and a_i, b_i, and c_i are constants derived (separately for HG and LG) using the precise shape of the pulse obtained from the test beam data (Figure 3.3).

There are two versions of the OF algorithm—with and without iterations. The non-iterative version shows better stability with increasing pileup, as it depends on the pulse being synchronized with the LHC clock and centered around the middle ADC sample. It is used during the standard data-taking conditions. The version with iterations uses the time of the maximal sample as the initial time offset and the calculated t in the subsequent iterations, converging to the true pulse peak time. It is used for the reconstruction of events that are asynchronous with respect to the LHC clock in low pileup conditions (e.g. cosmic-ray muon data).

By default, the HG signal is used. If any of the seven samples saturate the HG ADC, the LG signal is used instead. In standard cells, the gain-switch threshold corresponds to approximately 10–12 GeV of channel energy, depending on the nominal gain value of the channel.

The pulse amplitude A from Equation (3.1) is converted to the channel energy

$$E_{\mathrm{ch}}[\mathrm{GeV}] = \frac{A[\mathrm{ADC}]}{C_{\mathrm{Cs}} \cdot C_{\mathrm{laser}} \cdot C_{\mathrm{MB}} \cdot C_{\mathrm{ADC}\to\mathrm{pC}}[\mathrm{ADC/pC}] \cdot C_{\mathrm{pC}\to\mathrm{GeV}}[\mathrm{pC/GeV}]} \tag{3.2}$$

using constants C_{Cs}, C_{laser}, C_{MB}, and $C_{\mathrm{ADC}\to\mathrm{pC}}$ obtained with TileCal calibration systems (Sections 3.3.1 to 3.3.4) and constant $C_{\mathrm{pC}\to\mathrm{GeV}}$ measured using electron beams during test beams (Section 3.3.5) [38, 45].

The cell energy E_{cell} is given as a sum and the cell time t_{cell} as an average of signals of the corresponding readout channels

$$E_{\mathrm{cell}} = E_{\mathrm{ch1}} + E_{\mathrm{ch2}}, \qquad t_{\mathrm{cell}} = \left(t_{\mathrm{ch1}} + t_{\mathrm{ch2}}\right)/2.$$

If a signal of one of the channels is unavailable, the cell energy is calculated as twice the energy of the remaining channel. The energy is interpolated using signals from neighboring cells if the signal reconstruction in a given cell is not possible.

3.3 Energy calibration and monitoring

Multiple calibration systems are used to calibrate different steps of the signal reconstruction chain (Figure 3.4), resulting in corresponding calibration constants in Equation (3.2) so that the response of TileCal is stable and uniform across all its cells.

Besides the calibration, the systems are also used to monitor the calorimeter response. During the LHC collision periods, the response down drift is observed due to the degradation of scintillators, WLS fibers, and PMTs, which is caused by irradiation of the components. Components partially recover during periods without collisions and the response drifts upwards.

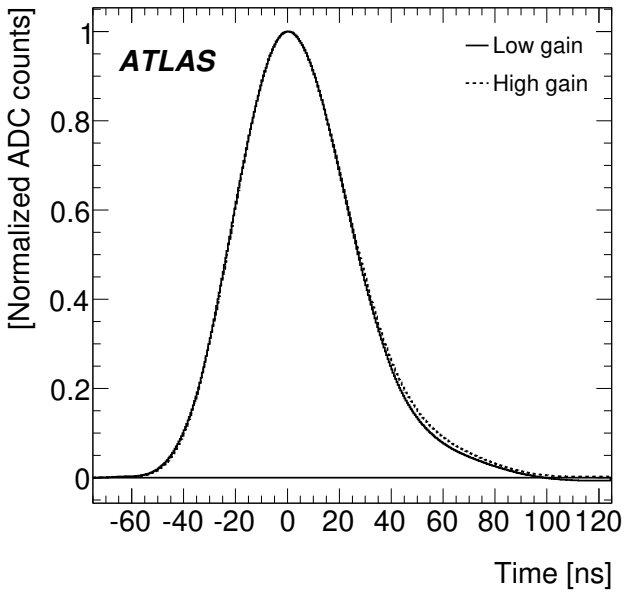

Figure 3.3: The HG and LG pulse shapes obtained from the test beam data [46].

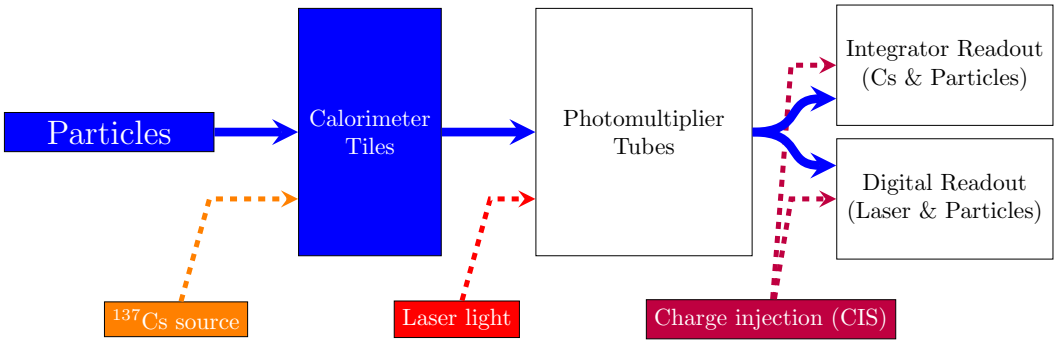

Figure 3.4: Three TileCal calibration systems (^{137}Cs source, laser light, and CIS) introduced at different steps of the signal reconstruction chain [38].

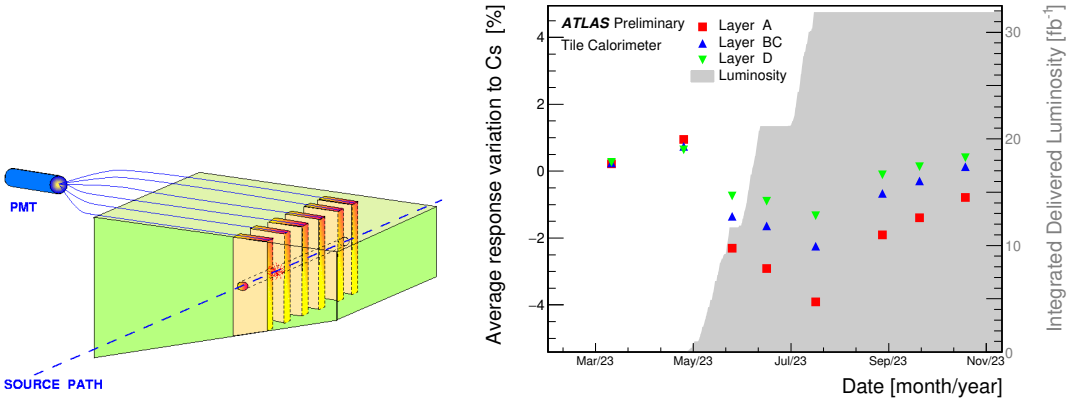

(a) (b)

Figure 3.5: (a) A schematic of a ^{137}Cs source path through the TileCal scintillator tiles [37]. (b) The average TileCal response variation to the ^{137}Cs source as a function of time during 2023 in the three radial layers (A, BC, D) of the calorimeter [39]. Results are normalized to the first measurement. The LHC delivered integrated luminosity is plotted in grey.

3.3.1 Cesium system

The cesium calibration system [47] uses movable capsules with ^{137}Cs γ-radiation source. The capsules are hydraulically driven through a circuit of stainless-steel tubes running through all rows of the calorimeter tiles (Figure 3.5a).

While traversing the scintillator tiles, ^{137}Cs produces γ-rays at 0.662 MeV (^{137}Cs decays into ^{137}Ba, which emits the photon while transitioning to its ground state) that are converted into Compton electrons inducing the scintillation light [47]. The light is transported by the WLS fibers to the PMTs and read out by the integrator system (Section 3.2.1). The signal produced in the calorimeter tiles is averaged over the readout cell, measuring the response of the corresponding channels.

Since the ^{137}Cs source directly illuminates the calorimeter tiles, all optics components—tiles and WLS fibers—and PMTs are monitored. The deviation of the calorimeter cells from the expected response (corrected for the $\sim 2.3\%$ of intensity loss per year of the ^{137}Cs source [47]) is caused by the degradation of the optical components and by the gain variation of the PMTs (Figure 3.5b). The largest effect is observed in the innermost radial layer (layer A) as it is the most irradiated one. To ensure an uniform calorimeter response, the constant C_{Cs} from Equation (3.2) is introduced in each channel.

The precision of the cesium calibration system is approximately 0.3% in a standard TileCal cell [38].

3.3.2 Laser system

The laser source of the TileCal laser calibration system is located in the USA15 cavern [48]. The 532 nm green light pulses emitted by the source are simultaneously distributed to the calorimeter PMTs by clear optical fibers. Each module

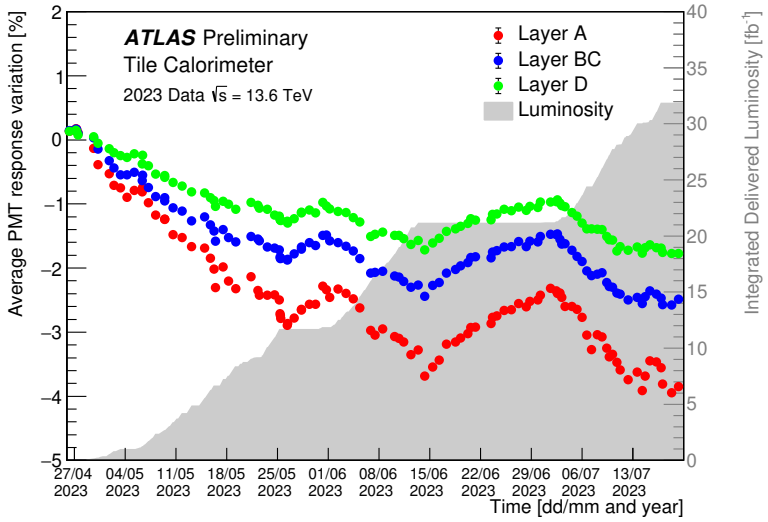

Figure 3.6: The average relative response variation of TileCal to the laser signal as a function of time during 2023 in the three radial layers (A, BC, D) of the calorimeter [39]. Results are normalized to a set of reference runs taken prior to the initial date. The LHC delivered integrated luminosity is plotted in grey.

of the extended barrel is connected to two fibers—one fiber for even PMTs and another fiber for odd PMTs. In the case of the long barrel, two fibers are used for the full module (both A and C sides combined)—one fiber for even (odd) PMTs in the A (C) side and another fiber for odd (even) PMTs in the A (C) side.

The laser system can be run in a standalone mode (in the absence of the LHC collisions), used to perform dedicated calibration runs or in a laser-in-gap mode used for the detector monitoring during the data taking (more in Section 3.4). The calibration constant C_{laser} from Equation (3.2) is derived using the standalone calibration runs in each channel—an average channel response is compared to a response in a reference laser calibration run taken close to a cesium scan (Section 3.3.1)—correcting for the drift of the PMT response (Figure 3.6).

The precision of this method is approximately at the level of 0.5% [38, 49].

3.3.3 Charge injection system

The conversion factor $C_{\text{ADC}\to\text{pC}}$ is measured by CIS [44, 46], which injects a signal with a well-defined charge to the readout electronics of all channels through the 3-in-1 cards, in a dedicated calibration runs. The charge magnitude is varied in discrete steps to cover the whole dynamic range of ADCs of both gains in each channel. The dependence of the reconstructed amplitude in ADC counts on the injected charge in pC is fitted by a linear function separately for the HG and LG. The slope of the fit determines the $C_{\text{ADC}\to\text{pC}}$ conversion factor of ADC in each gain of each channel.

The precision of CIS is approximately 0.7% [38] and the $C_{\text{ADC}\to\text{pC}}$ constant is very stable over time (Figures 3.7a and 3.7b).

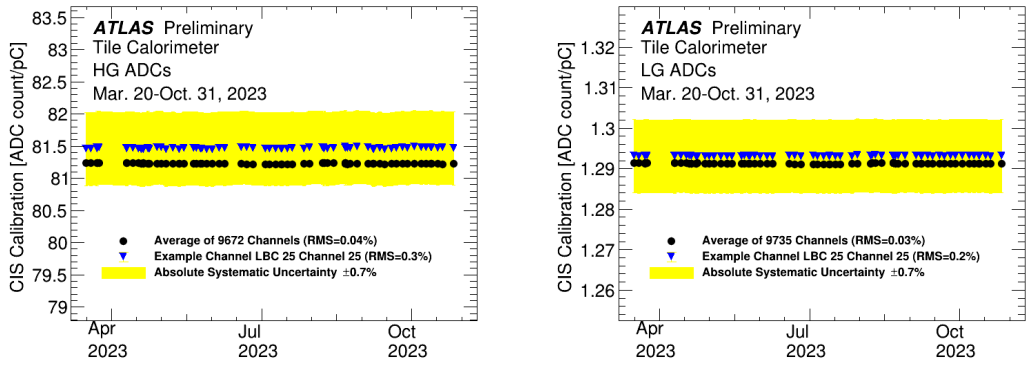

(a) (b)

Figure 3.7: The average conversion factor $C_{\mathrm{ADC}\to\mathrm{pC}}$ of the charge injection system for the (a) HG and (b) LG as a function of time during 2023 [39].

3.3.4 Minimum bias system

The minimum bias (MB) system [38] uses a signal created in the calorimeter by MB events—inelastic proton–proton (p–p) collisions at low energy transfers—read out by the integrator system (Section 3.2.1). The rate of the MB events and therefore the MB current in the PMTs is proportional to the LHC instantaneous luminosity and is used for monitoring of the response of optics components over time, validation of the response changes observed by the cesium system (since both share the same readout path), and calibration of special cells inaccessible by the ^{137}Cs source. In each cell type, the average deviation of the calorimeter response due to the degradation of the optics components is used as a calibration constant C_{MB} from Equation (3.2) during the ATLAS data reprocessing—dedicated campaigns during which the data are reprocessed with improved calibrations, reconstruction algorithms, and detector status information.

The precision of the MB measurements is approximately 1.2% [38].

3.3.5 Electromagnetic scale calibration

The constant $C_{\mathrm{pC}\to\mathrm{GeV}}$, calibrating the calorimeter response at the electromagnetic (EM) scale, was derived from the test beam data [45, 50]. The TileCal modules were placed on a movable scanning table in the CERN SPS North Area in a path of electron beams with energies of 20 to 180 GeV, hitting centers of A cells of the modules at an angle of 20°.

A sample of TileCal modules was used to derive the

$$C_{\mathrm{pC}\to\mathrm{GeV}} = 1.050 \pm 0.003 \text{ pC/GeV}$$

constant as a mean value of the distribution of the cells' responses (Figure 3.8). The root mean square (RMS) of the distribution is $2.4 \pm 0.1\%$.

Since most of the EM showers induced by the electrons are contained within the A layer of the module, the $C_{\mathrm{pC}\to\mathrm{GeV}}$ measurement was extended to the remaining radial layers of the calorimeter using measurements with muons traveling parallel to the module tile rows [45].

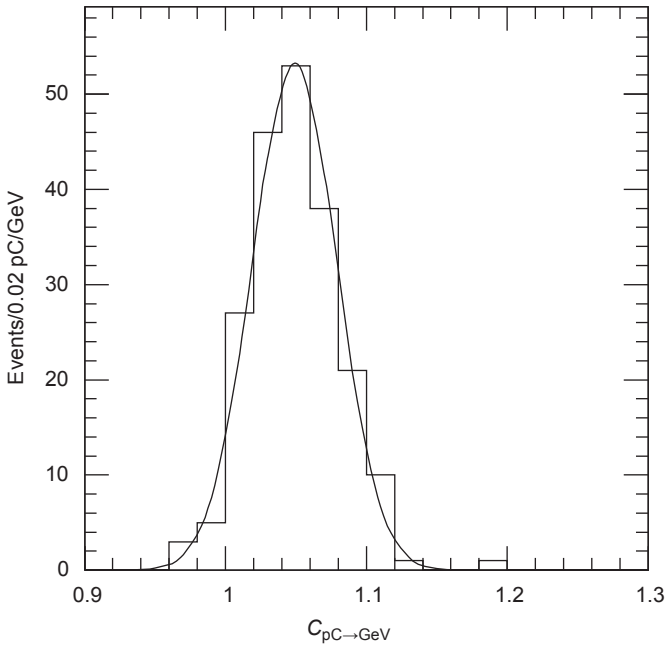

Figure 3.8: The TileCal cell response to 20° electrons obtained in a test beam data using electron beams with different energies [45].

3.4 Time calibration and monitoring

Since the correct energy reconstruction of the OF algorithm depends on the precise knowledge of the time phase of the signal with respect to the LHC clock, the time setting of each TileCal channel is adjusted so that the particles traveling at the speed of light that originated from the ATLAS interaction point (IP) generate a signal pulse with the time phase equal to zero. Besides the energy reconstruction, time calibration is also important for non-collision background removal and time-of-flight measurements.

The time calibration is performed using multiple types of data (e.g. laser system and beam-splash events), the final of which uses jets in p–p collision data.

3.4.1 Time calibration using jets

The final method of the time calibration utilizes the physics data. To mitigate effects of pileup and non-collision background, only cells corresponding to well-reconstructed jets are used—$R = 0.4$ anti-k_{T} EMTopo jets (defined in Chapter 4) with transverse momentum of $p_{\mathrm{T}} > 20$ GeV, passing standard quality cuts [51].

The HG and LG are calibrated separately in each channel. Since the cell reconstructed time slightly depends on the energy deposited in the cell, additional cut on channel energy $2 < E_{\mathrm{ch}} < 4$ GeV is used for HG and $15 < E_{\mathrm{ch}} < 50$ GeV for LG. The time dependence on the channel energy is steeper in the HG section than in the LG, therefore the selected E_{ch} range is narrower for the HG than for the LG. The reconstructed time distributions are produced by a dedicated time monitoring tool (Figures 3.9a and 3.9b) and have a Gaussian core with a small fraction of events at both tails of the distribution. The non-Gaussian tails—caused by slow components of the hadronic shower and the pileup—are more apparent for low-energy deposits in cells. The E_{ch} cut is chosen to minimize

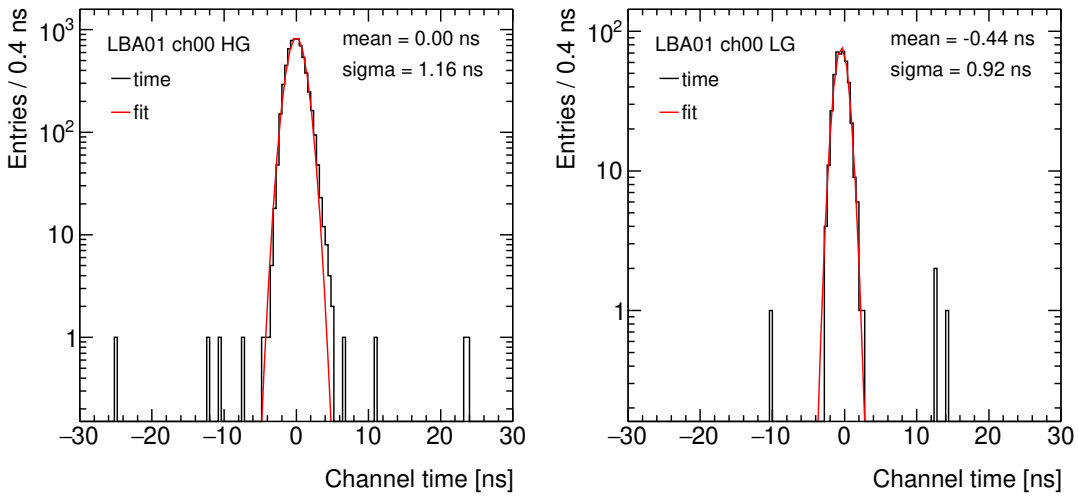

(a) (b)

Figure 3.9: Examples of the reconstructed channel time distributions in 2023 p–p collision data (black line) in (a) HG using $2 < E_{\text{ch}} < 4$ GeV and (b) LG using $15 < E_{\text{ch}} < 50$ GeV fitted by a Gaussian function (red line). Gaussian mean and sigma are displayed.

the distribution tails in the low-energy bins while avoiding lower statistics of the high-energy bins (Appendix A, Figure A.1).

The core of the reconstructed time distributions is fitted by a Gaussian function. The time calibration constants are adjusted according to the Gaussian mean. During the reconstruction, the calibration constants are subtracted from the time synchronized with the LHC clock, resulting in the pulse peak being close to the middle of the seven ADC samples.

Due to different signal paths in the HG and LG, there is an average time difference of

$$t^{\text{las}}_{\text{HG}-\text{LG}} = 2.3 \text{ ns}$$

between the gains, which was measured using special laser runs [52]. The time difference between the gains due to the deposited energy dependence was measured to be

$$t^{\text{phys}}_{\text{HG}-\text{LG}} = -0.48 \text{ ns}$$

on average, using the 2–4 GeV (HG) and 15–50 GeV (LG) channel energy cuts in physics runs. Therefore, the average difference between the HG and LG time constants is

$$t^{\text{const}}_{\text{HG}-\text{LG}} = t^{\text{las}}_{\text{HG}-\text{LG}} + t^{\text{phys}}_{\text{HG}-\text{LG}} = 1.82 \text{ ns}. \tag{3.3}$$

After the final time calibration using jets in collision data, the reconstructed time as a function of cell energy is consistent across the TileCal partitions (Figure 3.10a). The time resolution improves with increasing energy deposited in a cell (Figure 3.10b). It is better than 1 ns for energy larger than a few GeV and approaches 0.4 ns for large energies. The resolution in the extended barrel is systematically slightly worse due to larger calorimeter cells.

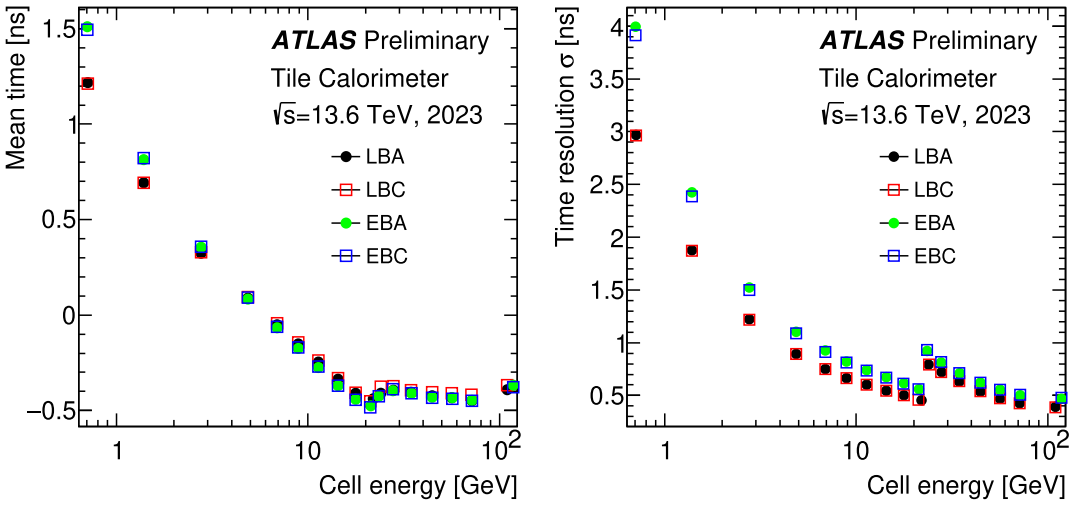

(a) (b)

Figure 3.10: (a) The mean partition reconstructed cell time and (b) the cell time resolution as functions of the cell energy using jets in 2023 13.6 TeV p–p collision data [53].

Time calibration in 2022

At the beginning of the Run 3 data taking in 2022, the initial 900 GeV p–p collision runs were used for the first rough time setting. Due to a very low statistic, a wider channel energy cut of 1–6 GeV was used instead of the standard 2–4 GeV. The time was reconstructed using an OF algorithm with iterations, as it performs better for large time offsets. The time setting was adjusted according to the mean partition times, shifting the reconstructed time closer to the center of the ADC readout window.

Later, the HG time constants were set separately in each channel with jets from the initial lower-luminosity 13.6 TeV p–p collision runs using the standard procedure. The LG constants were set using corresponding HG constants and the average HG−LG difference from Equation (3.3).

The HG calibration was later validated using 13.6 TeV runs at the nominal luminosity, providing enough statistics so that the LG was also calibrated on a per-channel basis instead of using the average gain difference, improving the LG time resolution to the expected level compatible with the Run 2 resolution. The HG−LG differences (1.77 ns on average, compatible with Equation (3.3) within 0.05 ns) were used also for the whole 2022 dataset reprocessing.

Time calibration in 2023

The initial 2023 time calibration was derived with the first 13.6 TeV collision data using the HG reconstructed time. Instead of the average HG−LG difference, the differences calculated from the 2022 data (Figure 3.11a) were used in each channel for the initial LG calibration, resulting in a better LG time resolution.

Both the HG and LG calibrations were validated using later runs at higher luminosity. New HG−LG constant differences (1.84 ns on average, compatible

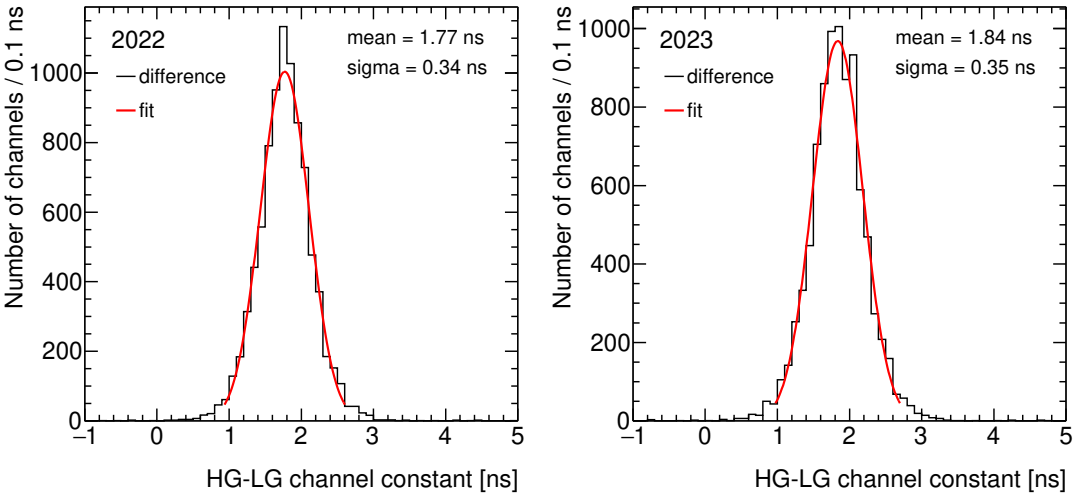

(a) (b)

Figure 3.11: The time constant differences between HG and LG in normal TileCal cells (black line) in (a) 2022 and (b) 2023 p–p collision data fitted by a Gaussian function (red line). Gaussian mean and sigma are displayed.

with Equation (3.3) within 0.02 ns) calculated for 2023 data (Figure 3.11b) were used for the reprocessing.

The use of the HG−LG differences from the previous year for the initial LG calibration was confirmed to be reasonable, comparing the differences from 2022 and 2023. The $t_{\mathrm{HG-LG}}^{\mathrm{const,\ 2023}} - t_{\mathrm{HG-LG}}^{\mathrm{const,\ 2022}}$ distribution (Figure 3.12) has a mean value of 0.07 ns and RMS of 0.10 ns, showing a good stability over time.

Time calibration in 2024

Similarly to the previous year, the initial 2024 time calibration was derived with the first 13.6 TeV collision data using the HG reconstructed time in each channel and the HG−LG channel time constant differences from 2023.

The 2024 data taking is currently in progress. The initial calibration will be validated using future runs, using the channel time distributions in both the HG and LG, providing new 2024 HG−LG constant differences that will be used for the 2024 reprocessing.

3.4.2 Time monitoring

To monitor the time calibration and to correct for timing instabilities and other problems (e.g. timing jumps, bunch-crossing offset (BCO) problem, more in Ref. [38] and Section 3.4.3), two complementary methods utilizing laser-in-gap events and jets from physics data are used.

The laser-in-gap events are recorded during physics data taking during empty LHC bunch crossings (separated from filled bunches by a few bunch crossings so the detector is clear of the collision signals). As a result, the HG reconstructed time is obtained in each channel as a function of the luminosity block (LB) (Figure 3.13a). The LB is a segment of data corresponding to roughly one minute of

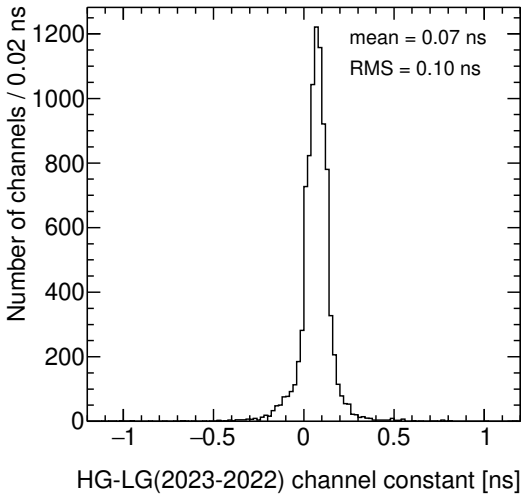

Figure 3.12: Comparison of the time constant HG−LG differences in normal TileCal cells between 2023 and 2022 p–p collision data. Histogram mean and RMS are displayed.

data taking, during which the detector conditions remain approximately constant.

The second method uses jets from physics data to obtain the average reconstructed HG time in each channel (Figure 3.13b).

3.4.3 Time problems

Besides the routine time calibration in the sense of setting the correct time constants in each TileCal channel (described in Section 3.4.1), there are multiple timing issues—like problem of timing jumps (more in Ref. [38, 48]), the BCO problem, and more—that have to be accounted for.

Bunch-crossing offset

During Run 2, the laser-in-gap monitoring system observed channels with reconstructed time shifted by one or two bunch crossings (±25 or ±50 ns, Figure 3.14a). The offset is intermittent, occurring at a rate of approximately 1%. It is fully correlated across groups of three channels corresponding to a common DMU. Affected DMUs are flagged using laser data and a dedicated software tool using physics data was developed to identify the affected events in problematic channels so they are excluded from the subsequent reconstruction.

Standard TileCal cells are read out by two PMTs corresponding to two readout channels. In most cases, the channels are grouped to the DMUs so that two channels of one cell and one channel of a neighboring cell are present. For the use of the BCO tool, a reference channel is defined—a second channel in a different DMU of the cell with only one channel corresponding to the affected DMU. In some cases, there could be more than one reference channel for DMUs containing only one channel of multiple standard cells. In that case, the channel with the largest energy is chosen in a given event.

The BCO tool is based on a comparison of the reconstructed time of the affected channels to the time t_{ref} of the corresponding reference channel. Selec-

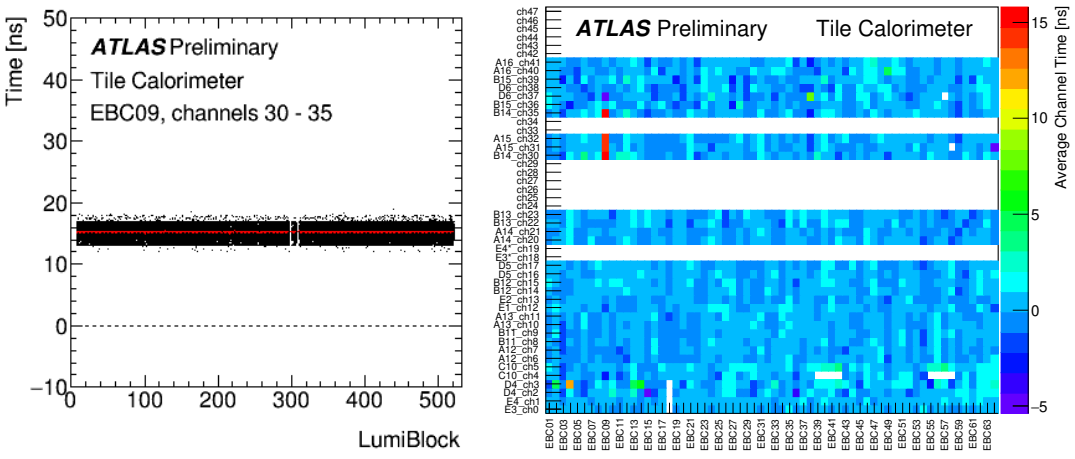

(a) (b)

Figure 3.13: TileCal reconstructed time (a) as a function of luminosity block monitored using laser-in-gap events [39] and (b) as a function of module and channel numbers monitored using physics data in the same run [53]. Both time monitoring methods simultaneously observe a timing jump [38] of approximately 15 ns in channels 30–35 of module EBC09.

tion criteria were optimized to flag as many affected events as possible without producing false positives.

First, only events with sufficient energy in the problematic cells are considered. At least one channel from the affected DMU or the reference channel has to have the energy E_{ch} above 1 GeV. In the case of affected DMUs containing only one channel, a tighter cut using a threshold of 3 GeV is used instead.

To ensure a correct time reconstruction in the reference channel, the difference of the maximal and minimal ADC samples in the case of a HG signal has to be larger than or equal to 15 ADC counts—the threshold above which the DSP time is calculated. Below the threshold, the time is set to 0 ns. The cut is not needed for the LG as the LG DSP time is calculated in any case. Only the in-time signal is utilized—the cut $|t_{\text{ref}}| < 10$ ns on the reference channel time is used.

The offset is correlated across the DMU, the reconstructed times of the corresponding channels therefore have to be within 15 ns of each other. Using only channels with energy above 0.5 GeV, an average DMU time is calculated.

Besides flagging the affected DMUs, the laser monitoring tool also provides an expected offset sign. According to the expected sign, the average DMU time has to be larger or smaller than the reference channel time by at least 15 ns.

The performance of the tool depends on the geometry of cells corresponding to the affected DMU. As an example, in the case of channels 39–41 of module EBA40 that exhibited the BCO problem with expected offset of +25 ns during Run 2 (Figure 3.14b), two cells are affected—A16 (channels 40 and 41) and B15 (channel 39, corresponding reference channel 36 in a different DMU). As the reference channel is in the B layer of the calorimeter, on average, its reconstructed energy will be lower than in channels of the A16 cell. Therefore a situation can occur in which the BCO is present in a given event with significant energy in the A16 cell but the reference channel signal is below the BCO tool threshold and

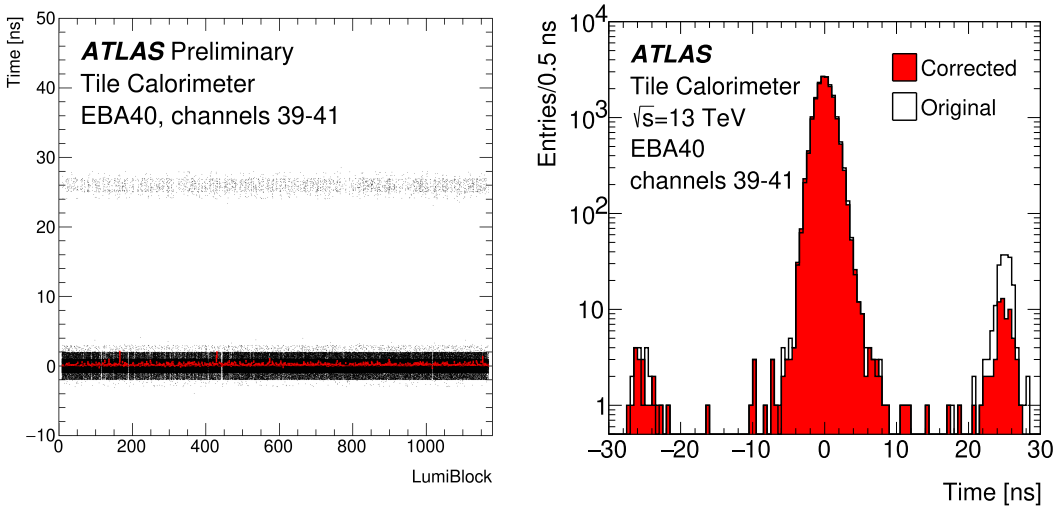

(a) (b)

Figure 3.14: (a) The BCO observed in the laser-in-gap reconstructed time as a function of LB number in three channels corresponding to one DMU [38]. Fraction of events are present at 25 ns. (b) The time in physics collision data in three channels with energy of 2–4 GeV corresponding to one DMU reconstructed with (Corrected) and without (Original) the algorithm for mitigation of the BCO problem, significantly reducing the events around $\sim$ 25 ns [38]. Besides the BCO mitigation algorithm, the two histograms differ in other reconstruction conditions responsible for differences in the rest of the spectrum.

the event is not masked in the affected channels. In contrast, significant signal in B15 implies signal in A16 cell (as the A16 cell is located in front of B15 with respect to the ATLAS IP), leading to masking of majority of the BCO events.

As a result, in signals with $2 < E_{\text{ch}} < 4$ GeV, the tool removes approximately 1% of total events in channel 39 and approximately 0.6% in channels 40 and 41. The remaining events close to +25 ns in channel 39 are compatible with the out-of-time pileup. In channels 40 and 41, events at +25 ns are reduced approximately by a factor of four.

The BCO tool was used during the Run 2 data reprocessing and is currently in use during Run 3.

LB−EB offset

During 2022, it was observed that in roughly half of the runs, the time of the extended barrel channels is shifted by approximately −0.1 ns compared to the long barrel channels. The offset is fully correlated across both gains and detector sides and is visible in the physics and the laser-in-gap data. Comparing mean partition times—using a mean of a Gaussian fit of the partition time distribution in physics data—affected runs are identified (Figure 3.15). This offset was considered during the 2022 data reprocessing, correcting extended barrel timing of the affected runs, and during both the 2023 initial calibration and reprocessing.

The issue was caused by the ATLAS Local Trigger Interface (ALTI)—which is part of the TileCal TTC system and was installed before the Run 3 data taking—

changing the clock delay settings between the calibration and physics runs. The change in settings happened after the first physics run following the calibrations, effectively shifting the timing of the first physics run with respect to the rest. The issue was fixed during the maintenance between the 2023 and 2024 data-taking periods (now, the clock delay settings stay the same for the calibration and physics runs) and is not present in the 2024 data anymore.

Double peak in E cells

During 2023, a double-peak structure was observed in some TileCal channels corresponding to LG signals in E1 and E2 cells (Figure 3.16a), using the standard cuts—cells are parts of selected jets (Section 3.4.1), $15 < E_{\text{ch}} < 50$ GeV.

Using a special set of data, the reconstructed time distributions were produced separately for combinations of all E1 and all E2 cells in the A and C sides of the detector, using the channel energy cut of $15 < E_{\text{ch}} < 50$ GeV (Figure 3.16b). Two peaks of the distributions correspond to the HG and LG signals—LG signal being the one that peaks at the larger reconstructed times.

Therefore, the LG channels in 2023 were calibrated using the corresponding peak in the LG time monitoring histograms. Additionally, an explicit gain cut was added to the monitoring tool producing the time histograms used for the time calibration, as the cut on the channel energy is insufficient for the gain differentiation in the special E1 and E2 cells with large gain value variations. The normal calorimeter channels are unaffected, as the 15 GeV lower threshold is well above the standard gain-switch threshold of approximately 10–12 GeV.

The issue is not expected in the 2024 LG monitoring histograms thanks to the additional gain cut in the time monitoring tool.

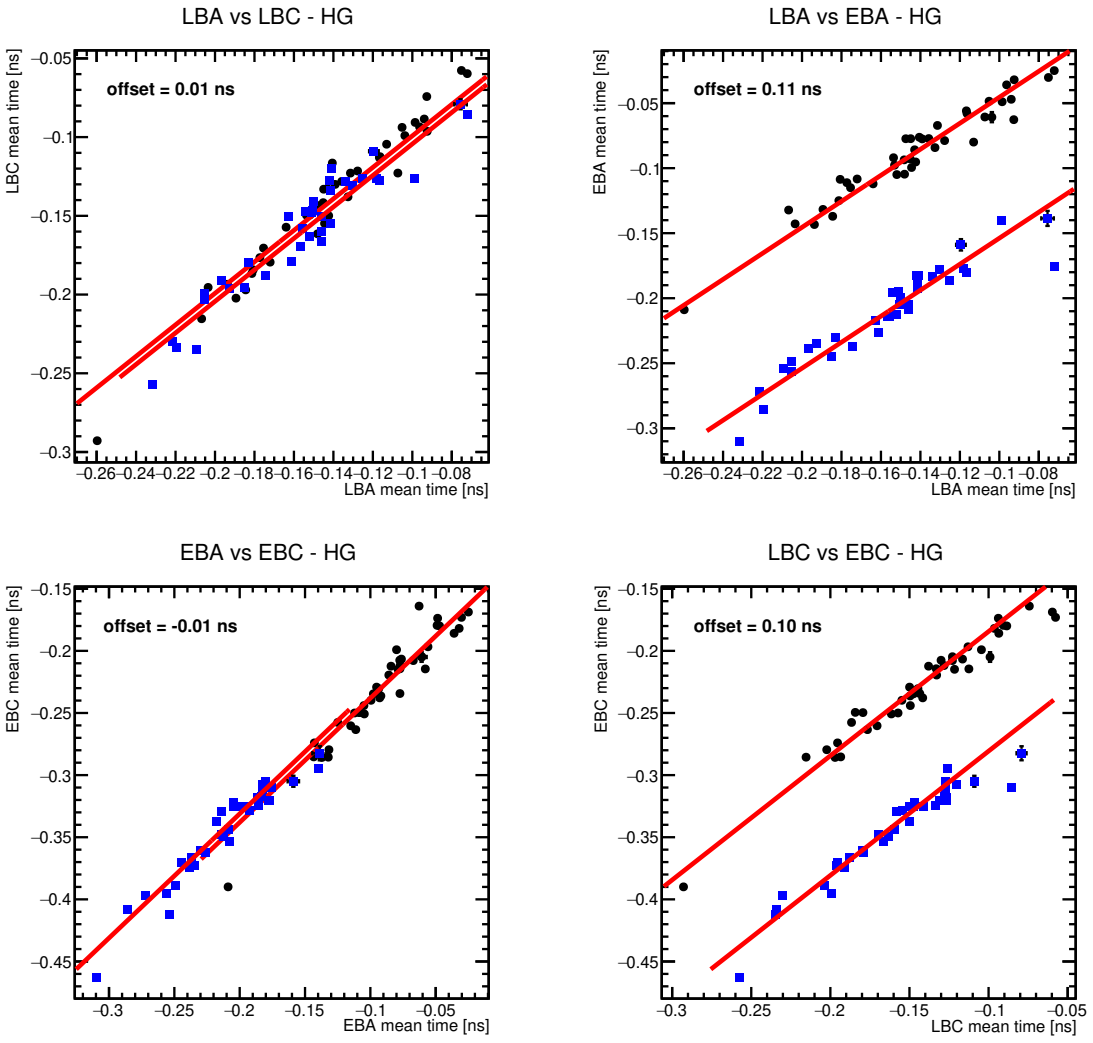

Figure 3.15: The mean partition time in the HG comparing (top left) LBA and LBC, (top right) LBA and EBA, (bottom left) EBA and EBC, and (bottom right) LBC and EBC. Two groups of runs (black circles, blue squares) are fitted by a one-parametric linear function (red line) with a slope equal to one. A displayed difference in the fit parameters of the two run groups shows approximately 0.1 ns offset comparing long and extended barrels. A set of 2023 13.6 TeV p–p collision runs is used. The same offset is observed also in the LG (Appendix A, Figure A.2).

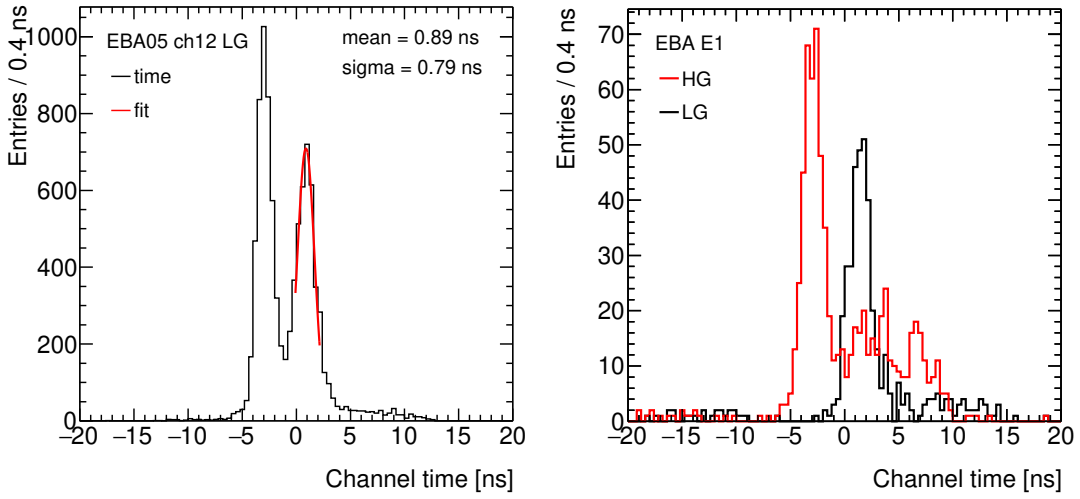

(a) (b)

Figure 3.16: (a) An example of a double peak in the LG time monitoring histogram of one E1 cell in the 2023 p–p collision data (black line). The peak corresponding to the LG signal is fitted by a Gaussian function (red line). Gaussian mean and sigma are displayed. (b) An example of HG (red line) and LG (black line) signals present in E cells using the standard channel energy cut of $15 < E_{\text{ch}} < 50$ GeV. A combination of E1 cells from all EBA modules is used.

4. Jet reconstruction and calibration at ATLAS

Partons (quarks and gluons) originating from the hard-scattering processes in the p–p collisions quickly hadronize due to the quantum chromodynamics (QCD) color confinement [2], producing collimated particle showers—jets.

When traveling through matter, high-energy hadrons undergo inelastic collisions with nucleons in nuclei, producing more hadrons. The secondary hadrons can interact similarly, developing a hadronic shower while they have sufficient energy. The remaining nuclei are left in an excited state—undergoing processes like evaporation, spallation, and fission, they produce more particles.

Pions $\pi^{\pm}$ and π^0, as the lightest hadrons, are created with large multiplicities in the inelastic collisions with nucleons. Neutral pions quickly decay into photon pairs $\pi^0 \to \gamma\gamma$, which develop an electromagnetic (EM) component of the hadronic shower. High-energy photons produce electron–positron pairs—the energy threshold of the pair production is two electron masses $2m_e = 1.022$ MeV [54]. Positrons and electrons produce more photons via Bremsstrahlung. The development of an EM shower stops when electrons and positrons have low enough energy so that ionization energy losses dominate the radiative ones (usually a few MeV to a few tens of MeV, energy threshold is material dependent [2]).

After the shower development stops, the remaining charged particles leave a signal in the active environment of the ATLAS calorimeters through ionization.

4.1 Jet reconstruction

Jets are observed as energy deposits in the ATLAS calorimeters. In addition, charged hadrons also leave tracks in the ATLAS Inner Detector (ID). The exact jet definition depends on the specific algorithm used for the jet reconstruction.

4.1.1 Topoclusters

By grouping of the neighboring calorimeter cells, topological clusters (topoclusters) are built [55].

In the first step, cells with energy deposits above 4σ are located (σ being the expected noise in a given cell), seeding the clusters. The cell noise comes from the pileup and electronics.

Next, all neighboring cells with energy deposits above 2σ are added to the clusters. If one cell is adjacent to multiple clusters, they are merged. This step repeats until there are no neighboring cells with such a significant signal left.

After that, all neighboring cells are added to the cluster no matter their energy to contain shower tails.

To account for the effects of overlapping showers, a cluster-splitting algorithm is used to split previously created clusters according to local energy maxima [55, 56].

Each cluster is assigned total energy (and corresponding momentum) and direction using η–ϕ coordinates with respect to the nominal interaction point

(IP), calculated as an energy-weighted mean using positions of the constituent cells [56].

In each event, the primary vertex is defined as a reconstructed vertex associated with at least two tracks and the largest sum of squared track momenta [57]. Hard-scattering jets are expected to originate from the primary vertex, therefore η and ϕ of each topocluster are corrected so they point to the primary vertex instead of the nominal IP.

4.1.2 Topocluster calibration

The ATLAS calorimeters are non-compensating [17]—the response to hadrons is lower than the response to electrons. Part of the energy of incident hadrons is lost in interactions with nuclei. It is used to release nucleons from nuclei, overcoming the nuclear binding energy, and absorbed by nuclei in the form of recoil. Particles that escape the detector—like muons and neutrinos created in decays of hadrons—also contribute to the invisible energy. Contrary to the linear response of the calorimeters to electrons, the response to hadrons is non-linear and increases with incident hadron energy [45].

There are two calibration schemes on the level of topoclusters—the EM scale calibration and the local cluster weighting (LCW) calibration.

Usually, the energy of topoclusters is derived at the EM scale. The calorimeter response to the EM showers with respect to the true shower energy is close to unity. Jets constructed from the EM calibrated topoclusters are called EM jets. The non-linearity of the response to hadrons is compensated during the jet energy scale (JES) calibration (Section 4.2).

The second approach—LCW—considers the non-linearity of the hadronic response already on the topoclusters level [56, 58]. In the first step, topoclusters are classified as EM or hadronic using shower parameters like shower length, depth, and signal density [58]. Each topocluster is assigned a probability $\mathcal{P}_{\text{cluster}}^{\text{EM}}$ of it being generated by an EM shower. Energy correction weights based on a Monte Carlo (MC) simulation are derived separately for EM and hadronic showers, considering the non-linearity of response to hadronic showers, out-of-cluster corrections (due to noise effects at the shower perimeters), and dead-material corrections (due to energy losses in front of or between the calorimeter modules). Each cell in the topocluster is assigned a new weight according to the probability $\mathcal{P}_{\text{cluster}}^{\text{EM}}$ and cluster energy and direction are recalculated.

The LCW calibration reduces the measured energy fluctuations and therefore improves the energy resolution of jets constructed from the LCW clusters compared to the EM jets [59].

4.1.3 Anti-k_{T} algorithm

Calorimeter jets are built using the anti-k_{T} algorithm [60] (FastJet package [61, 62]). Usage of different inputs to the algorithm yields different types of jets—topoclusters are used to reconstruct topological (Topo) jets, particle flow (PFlow) objects for PFlow jets (Section 4.1.4), and MC simulated particles to obtain the truth-level simulated jets.

The distance d_{ij} between input objects i and j and the distance $d_{i\mathrm{B}}$ between object i and the beam axis are defined as

$$d_{ij} = \min\left(\frac{1}{{k_{\mathrm{T}i}}^2}, \frac{1}{{k_{\mathrm{T}j}}^2}\right)\frac{{\Delta R_{ij}}^2}{R^2}, \tag{4.1}$$

$$d_{i\mathrm{B}} = \frac{1}{{k_{\mathrm{T}i}}^2} \tag{4.2}$$

using their transverse momenta $k_{\mathrm{T}i}$ and $k_{\mathrm{T}j}$, their angular distance ΔR_{ij} (from Equation (2.1)), and chosen jet radius parameter R (often $R = 0.4$). In the first step, the distance variables d_{ij} and $d_{i\mathrm{B}}$ are calculated for all pairs and all single objects, respectively. The minimum of d_{ij} and $d_{i\mathrm{B}}$ is found. If d_{ij} is the minimum, corresponding objects i and j are combined into a new one. If $d_{i\mathrm{B}}$ is the minimum, object i becomes a final jet and is removed from the input list. This process is repeated until all objects are combined into jets.

Using Equations (4.1) and (4.2), the anti-k_{T} algorithm combines objects starting from the ones with the largest k_{T}, proceeding from centers of jets to their edges, being less susceptible to the background noise.

4.1.4 Topological and particle flow jets

Using the calorimeter topoclusters (either EM or LCW calibrated) as an input to the anti-k_{T} algorithm, Topo jets are created [56]. An alternative approach uses the ATLAS ID tracks in addition to the signal of calorimeters to create PFlow jets [63].

In the case of the PFlow jets, a cell-based energy subtraction algorithm is used to remove overlaps of the ID and calorimeter measurements [63]. Each well-measured ID track is matched to a single topocluster, if possible. For all particles corresponding to the tracks, the expected energy deposited in the calorimeter is calculated using the track momentum and the position of the topocluster. The probability of one particle depositing energy in multiple topoclusters is evaluated and if needed, additional topoclusters might be matched to the track to recover the full shower energy. The expected energy deposited in the calorimeter is subtracted on a cell-by-cell basis from the matched topoclusters, removing the topoclusters completely in case the expected energy exceeds the total topocluster energy. The remaining topoclusters and tracks are used as an input to the anti-k_{T} algorithm, producing PFlow jets.

Inclusion of the ATLAS ID tracks to the jet reconstruction results in better energy and angular resolution for low-p_{T} jets compared to the solely calorimeter-based Topo jets [57, 63].

4.2 Jet calibration

No matter the topocluster calibration (EM or LCW) and the type of jets (Topo or PFlow), the principle of the jet energy calibration remains similar (Figure 4.1) [57, 63, 64].

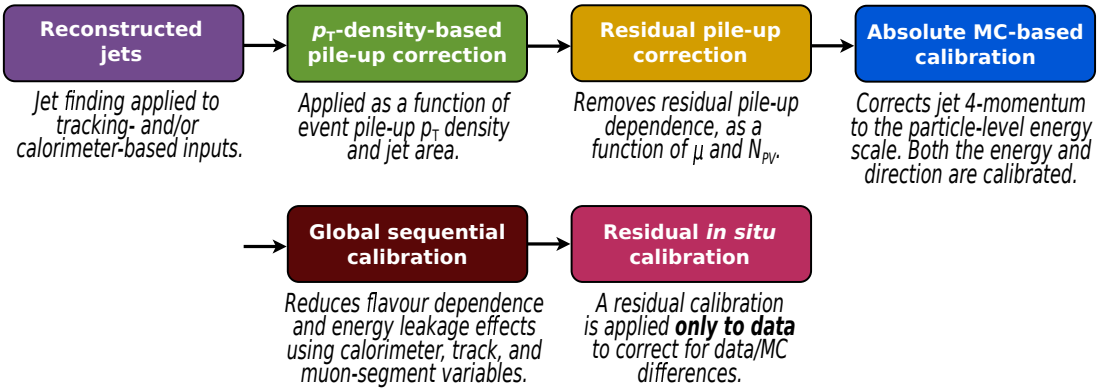

Figure 4.1: Stages of the jet calibration [57].

4.2.1 Pileup corrections

In the first step, jets are corrected for pileup effects based on the jet area [64, 65]. Jet area A (defined in the η–ϕ plane) is estimated using the method of ghost association (more in Ref. [65]). The pileup contribution is characterized using the median p_{T} density $\rho = p_{\mathrm{T}}/A$ of central jets ($|\eta| < 2.0$) in the given event. The reconstructed jet transverse momenta $p_{\mathrm{T}}^{\mathrm{reco}}$ are then corrected by the term $-\rho A$ in Equation (4.3). A residual pileup correction is applied to account for the jet p_{T} dependence on the in-time pileup using the number of reconstructed primary vertices N_{PV} and dependence on the out-of-time pileup using the mean number of interactions per beam crossing $\langle\mu\rangle$, resulting in the last two terms in Equation (4.3). Considering both the area-based and the residual pileup corrections, the corrected transverse momenta $p_{\mathrm{T}}^{\mathrm{corr}}$ of jets are calculated according to

$$p_{\mathrm{T}}^{\mathrm{corr}} = p_{\mathrm{T}}^{\mathrm{reco}} - \rho A - \alpha\,(N_{\mathrm{PV}} - 1) - \beta\langle\mu\rangle, \tag{4.3}$$

using parameters α and β [57].

4.2.2 Jet energy scale and η calibrations

After the pileup correction, a MC-based correction is applied to bring the reconstructed jet energy and momentum up to the truth level—the JES calibration—and to remove a bias in the jet η reconstruction. The calibration is derived using a Pythia 8 [12] MC simulation, using isolated jets reconstructed with the anti-k_{T} algorithm with $R = 0.4$ [57]. The reconstructed jets are geometrically matched to the corresponding truth-level jets within $\Delta R < 0.3$.

Using the selected isolated jets, the average energy response—parameterized as a function of detector rapidity η_{det} and jet energy—is defined as a ratio $E_{\mathrm{reco}}/E_{\mathrm{true}}$ of mean reconstructed and true jet energies (Figure 4.2a).

Using the selected isolated jets, the bias in the jet η reconstruction is defined as a difference between the true η_{true} and reconstructed η_{reco} values. The bias (parameterized again as a function of η_{det} and the jet energy) is the largest in transitional regions between calorimeter partitions using different technology and geometry (Figure 4.2b) The transition between the barrel and end-cap regions is at $|\eta_{\mathrm{det}}| \sim 1.4$ and the transition between the end-cap and forward regions is at $|\eta_{\mathrm{det}}| \sim 3.1$ [57]. The different energy responses in different calorimeter regions

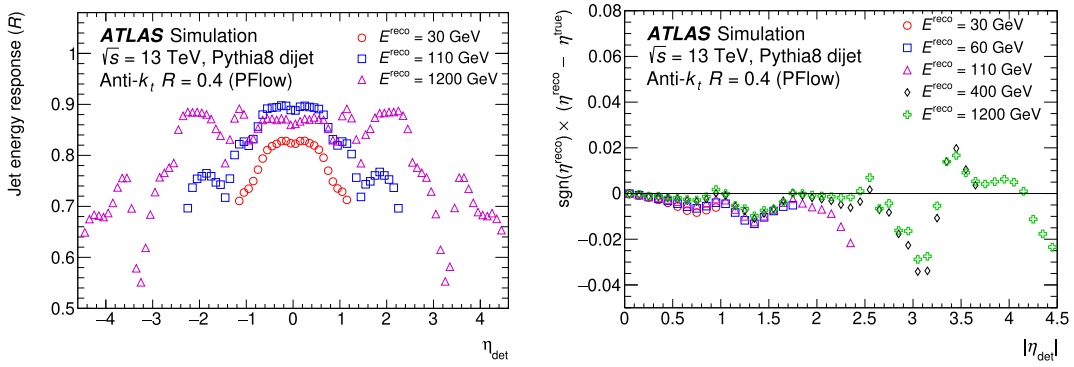

(a) (b)

Figure 4.2: A MC simulation of (a) the average jet energy response and (b) the signed difference between the reconstructed η^{reco} and true η^{true} jet pseudorapidities as functions of detector pseudorapidity η_{det} for different values of the jet reconstructed energy E^{reco} using PFlow jets simulated with Pythia 8 and reconstructed using the anti-k_{T} algorithm with $R = 0.4$ [57].

result in biased reconstruction of jets in the transitional regions—part of the jet in one region is reconstructed with increased energy relative to the other region, shifting the jet axis in the η plane.

4.2.3 Global sequential calibration

After the JES and η calibration based on energy and pseudorapidity of jets, residual dependence of the response on other variables—like jet flavor and shower shape and composition—remains. This residual dependence is corrected during the MC-based global sequential calibration (GSC) [57, 63].

Jets originating from gluons typically contain more soft particles, resulting in wider showers and lower calorimeter response. In comparison, quark-initiated jets contain more higher-p_{T} particles, resulting in longer showers and higher response [57]. The response of high-p_{T} jets that are not fully contained within the calorimeter is also corrected during this step.

Variables used in the GSC include tracking information from the ID, a fraction of the jet energy deposited in different layers of the calorimeter system, and information from the Muon Spectrometer (MS) and they differ for PFlow and Topo jets. The GSC corrections based on selected variables are applied separately as multiplicative constants to the four-momenta of jets, improving the resolution of the JES without changing the average scale.

4.2.4 Residual *in situ* calibrations

In the last step of the calibration procedure, the difference between the detector response to jets in the data and MC simulation is accounted for. The *in situ* corrections are based on balancing the jet p_{T} against other, well-measured reference objects. The detector response is calculated as a ratio of the jet p_{T} over the p_{T} of the reference object and the correction factor, which is applied to the data, is calculated as a ratio of the response in the data and MC.

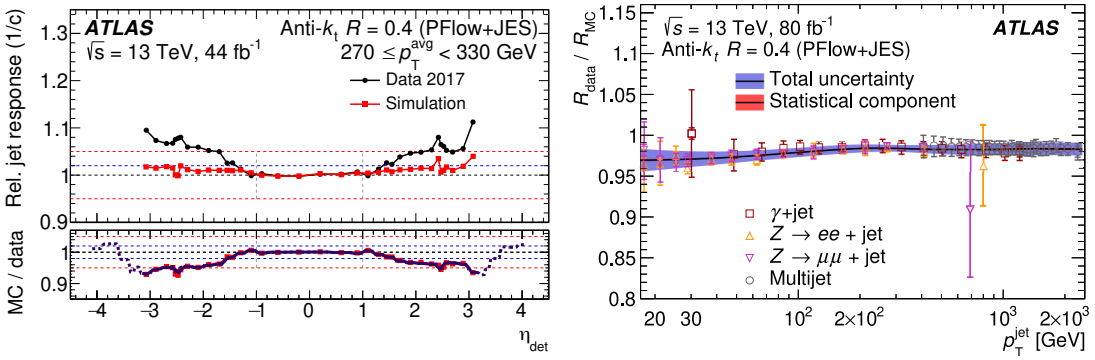

(a) (b)

Figure 4.3: (a) The relative response of PFlow jets in the data (black circles) and simulation (red squares) as a function of η_{det} derived using the η intercalibration method and (b) the data vs MC response ratio of PFlow jets (black line) derived using the γ/Z+jet and MJB methods (points) as a function of jet p_{T} [57].

The first step of the *in situ* corrections is the η intercalibration procedure [57, 66]. Forward jets with $0.8 \leq |\eta_{\text{det}}| < 4.5$ are compared to the well-measured central jets with $|\eta_{\text{det}}| < 0.8$ and the energy scale of the forward jets is adjusted to match the central ones (Figure 4.3a).

Second, the hadronic activity is compared to the well-measured γ and $e^{\pm}$ or $\mu^{\pm}$ from the Z boson decays $Z \to e^+e^-$, $Z \to \mu^+\mu^-$ [57, 67]. The p_{T} of γ and Z is balanced against a full hadronic recoil in the event to mitigate the effects of the pileup, underlying event, and others. The correction factors of this method are derived using jets in the central region $|\eta_{\text{det}}| < 0.8$ (Figure 4.3b)—thanks to the η intercalibration, results also apply to the forward jets.

Last, a multijet balance (MJB) method [57, 68] derives its correction factors using high-p_{T} (up to TeV scale) leading jet produced back-to-back to a recoil system of well-calibrated low-p_{T} jets (Figure 4.3b). The low-p_{T} jets are calibrated in the previous steps of the *in situ* method. Same as the γ/Z+jet method, the correction factors are derived using the central jets only.

Systematic uncertainties of the *in situ* calibrations are propagated sequentially from each method to the next (description of uncertainty components is in Section 5.5.1).

5. The dijet cross-section measurement

The jet production is the dominant high-p_{T} process in proton–proton (p–p) collisions at the LHC. Precise jet cross-section measurements are important high-energy tests of the quantum chromodynamics (QCD), able to probe the strong coupling constant α_{S} and to constrain parton distribution functions (PDFs) describing the proton structure—especially the gluon PDF at large momentum fraction x [2]. Jet events are also a common source of background to other processes at the LHC.

This chapter summarizes the current state of the multi-differential cross-section measurement of the inclusive dijet production in p–p collisions at 13 TeV center-of-mass energy, using the full Run 2 dataset of 139 fb^{-1} of total integrated luminosity.

The particle flow (PFlow) jets are reconstructed using the anti-k_{T} algorithm with a radius parameter $R = 0.4$. The reconstructed spectra are corrected for detector resolution and inefficiency effects using an Iterative, Dynamically Stabilized (IDS) method of data unfolding [69, 70]. The effect of the full set of jet energy scale (JES) and jet energy resolution (JER) systematic uncertainties is evaluated at the unfolded level. The dijet cross-sections are presented double differentially as functions of the invariant dijet mass m_{jj} and either y^* or y_{boost} variables, connected with the rapidity of the two jets (Section 5.1). The y_{boost} variable is used for the dijet cross-section measurement for the first time at ATLAS. The measurement covers the kinematic region of 240 GeV $< m_{\mathrm{jj}} <$ 10 TeV, $y^* < 3.0$, and $y_{\mathrm{boost}} < 3.0$.

The dijet cross-section was measured previously at ATLAS in 7 TeV and 13 TeV (using 2015 dataset of 3.2 fb^{-1}) center-of-mass p–p collisions [71, 72]. Compared to the last 13 TeV measurement, the current one provides a larger dataset (allowing approximately twice as fine binning), additional angular variable y_{boost} (which allows for better PDF sensitivity), and improved treatment of the systematic uncertainties (leading to a reduction of the total uncertainty).

5.1 Cross-section definition

The invariant mass of the dijet system

$$m_{\mathrm{jj}} = \sqrt{(P_1 + P_2)^2}$$

is defined using the four-momenta P_1 and P_2 of the leading and subleading jets. Jets are ordered according to their transverse momenta—leading and subleading jets having the largest and the second largest p_{T} in a given event.

The dijet event topology is described using half the absolute rapidity separation y^* and sum y_{boost} of the two jets

$$y^* = \frac{1}{2}|y_1 - y_2|,$$
$$y_{\mathrm{boost}} = \frac{1}{2}|y_1 + y_2|,$$

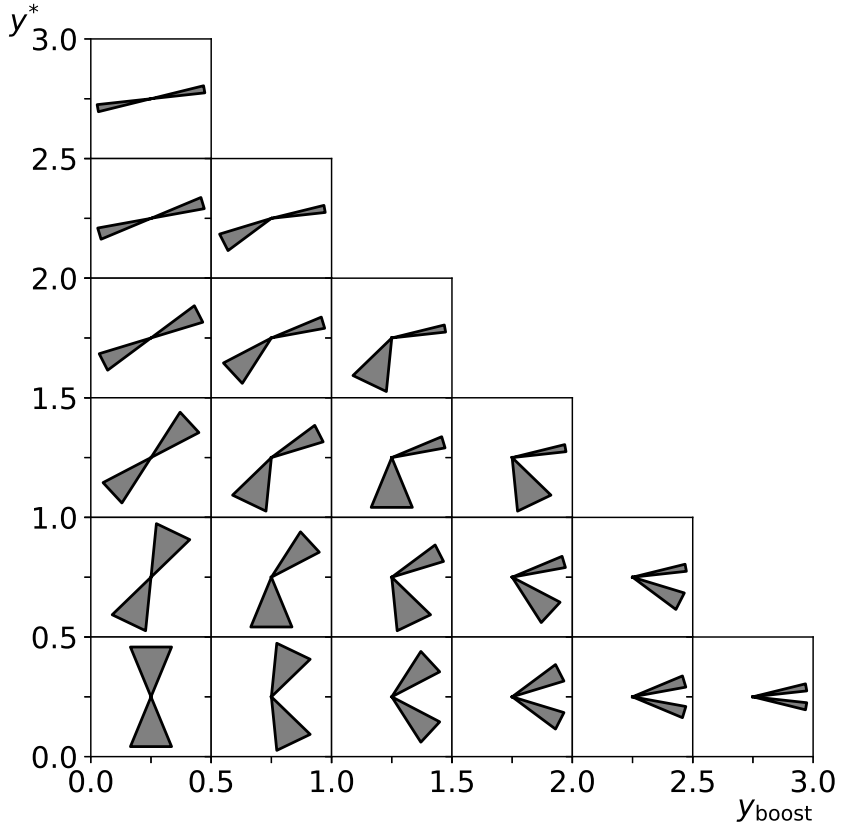

Figure 5.1: The dijet event topology as a function of y^* and y_{boost}. In each bin, the horizontal axis corresponds to the beam direction and the vertical axis corresponds to the x–y plane.

where y_1 and y_2 are the rapidities of the leading and subleading jets, respectively. The y^* variable is Lorentz invariant under boosts along the z-axis, corresponding to the rapidity of jets in the center-of-mass system ($y'_1 = -y'_2 = y^*$), whereas y_{boost} corresponds to the boost of the dijet system (Figure 5.1).

The dijet cross-sections are measured double-differentially using the dijet invariant mass and either the y^* or y_{boost} as

$$\frac{d^2\sigma}{dm_{\text{jj}}dy^*} = \frac{1}{\mathcal{L}}\frac{N_{\text{dijet}}}{\Delta m_{\text{jj}}\Delta y^*}, \tag{5.1}$$

$$\frac{d^2\sigma}{dm_{\text{jj}}dy_{\text{boost}}} = \frac{1}{\mathcal{L}}\frac{N_{\text{dijet}}}{\Delta m_{\text{jj}}\Delta y_{\text{boost}}}, \tag{5.2}$$

where $\mathcal{L}$ is the integrated luminosity of the dataset, N_{dijet} is a number of dijet events corrected for detector effects (after unfolding, Section 5.4), and Δm_{jj}, Δy^*, and Δy_{boost} are bin widths of the corresponding variables.

Both the y^* and y_{boost} variables are divided into six equidistant bins of width 0.5 in a range of $y^* < 3.0$ and $y_{\text{boost}} < 3.0$.

The m_{jj} bins spanning from 240 GeV up to 10 TeV were chosen considering event migrations in Monte Carlo (MC) simulation and statistical uncertainties (Appendix B, Tables B.1 and B.2). Provided the initial binning based on MC,

the last m_{jj} bin in each y^* and y_{boost} bin was determined using ATLAS data so that it contains at least 10 events.

5.2 Datasets

The analysis is performed using PFlow jets reconstructed with the anti-k_{T} clustering algorithm with a radius parameter $R = 0.4$ in the ATLAS data and Pythia MC simulation.

Data

The full LHC Run 2 dataset of p–p collisions at the center-of-mass energy $\sqrt{s} =$ 13 TeV recorded by the ATLAS detector is used. During the Run 2, the LHC delivered 156.1 fb^{-1} of 13 TeV p–p collisions with the nominal 25 ns proton bunch spacing [73]. Using the standard data-quality requirements—rejecting data due to problems and inefficiencies of the detector—results in 139 fb^{-1} of data used in the analysis [73, 74].

Monte Carlo

The jet MC samples were generated using the Pythia 8.186 generator [12] with the NNPDF2.3 leading order (LO) PDF set [75] and A14 tune [76]. It uses LO pQCD matrix elements for the simulation of the hard $2 \to 2$ processes, showering of partons calculated in a leading-logarithmic approximation [77], simulation of the underlying event including multi-parton interactions [78], and the Lund string model of hadronization [11].

The passage of stable particles produced by Pythia through the ATLAS detector was simulated using the Geant4 toolkit [79, 80]. The simulated events were reconstructed and resulting jets were calibrated with the same software tools that were used to process the ATLAS data, producing the reconstructed-level MC jets. The corresponding particle-level (truth) jets built from the stable particles are used as well.

The MC samples are divided into three campaigns MC16a, MC16d, and MC16e, corresponding to the 2015+2016, 2017, and 2018 data-taking conditions, respectively. The full Run 2 dataset is obtained by merging the three campaigns weighted according to the integrated luminosities of the corresponding ATLAS datasets.

Each campaign is divided into 13 slices (JZ0–JZ12) according to the transverse momentum of the leading jet at the particle level (Table 5.1). To improve event-generation efficiency, events were generated in reduced phase space at the hard-process level according to the transverse momentum of outgoing partons. Slices are merged using sample weights proportional to the corresponding cross-sections. Only slices JZ2–JZ12 are used in this analysis, as JZ0 and JZ1 effectively do not contribute to the cross-sections due to the jet selection (Section 5.3).

Table 5.1: Jet MC JZ slices with corresponding minimal outgoing parton transverse momentum $p_{\mathrm{T}}^{\mathrm{parton}}$ and range of leading truth jet transverse momentum $p_{\mathrm{T}}^{\mathrm{jet}}$.

Slice	$p_{\mathrm{T}}^{\mathrm{parton}}$ [GeV]	$p_{\mathrm{T}}^{\mathrm{jet}}$ [GeV]
JZ2	15	60–160
JZ3	50	160–400
JZ4	150	400–800
JZ5	350	800–1300
JZ6	600	1300–1800
JZ7	950	1800–2500
JZ8	1500	2500–3200
JZ9	2200	3200–3900
JZ10	2800	3900–4600
JZ11	3500	4600–5300
JZ12	4200	5300–7000

5.3 Selection

Each event selected for the analysis must contain at least one reconstructed primary vertex (PV) (to reject non-collision events) and at least two jets,

$$N_{\mathrm{PV}} \geq 1, \quad N_{\mathrm{jet}} \geq 2.$$

To reject incomplete data and corrupted Liquid Argon Calorimeter (LAr), Tile Calorimeter (TileCal), and Semiconductor Tracker (SCT) data, events are required to have

`coreFlags == 0`, `larFlags == 0`,
`tileFlags == 0`, `sctFlags == 0`.

To differentiate collision jets from ones originating from non-collision processes (e.g. beam-gas and beam-halo events, cosmic ray muons) and calorimeter noise, an event-level jet cleaning based on internal jet substructure variables

`eventClean_LooseBad == 1`

is implemented.

In each event, both the leading and subleading jets must pass the transverse momentum and rapidity cuts

$$p_{\mathrm{T}} > 75 \text{ GeV}, \quad |y| < 3.0.$$

The scalar sum H_{T} of transverse momenta of the leading and subleading jets p_{T1} and p_{T2} must satisfy

$$H_{\mathrm{T}} = p_{\mathrm{T1}} + p_{\mathrm{T2}} > 200 \text{ GeV},$$

effectively requiring the leading jet to have $p_{\mathrm{T1}} > 100$ GeV. The p_{T}, y, and H_{T} cuts are used for jets in the ATLAS data and for the MC reconstructed-level and truth-level jets.

To exclude miscalibrated jets originating from the out-of-time pile-up in the ATLAS data, the timing cut

$$|t| < 10 \text{ ns}$$

is used for leading and subleading jets.

Table 5.2: HLTs used in (a) 2015, (b) 2016, (c) 2017, and (d) 2018 data. Applied p_{T} ranges of 99.5% efficiency and corresponding integrated luminosities are displayed.

(a)

Trigger	p_{T} [GeV]	Luminosity [fb^{-1}]
HLT_j85	100–135	0.000 490 462
HLT_j110	135–185	0.001 391 1
HLT_j150	185–210	0.005 170 1
HLT_j175	210–310	0.010 323 7
HLT_j260	310–445	0.065 985 7
HLT_j380	445–	3.219 56

(b)

Trigger	p_{T} [GeV]	Luminosity [fb^{-1}]
HLT_j60	90–105	0.002 092 44
HLT_j85	105–140	0.002 181 9
HLT_j110	140–210	0.018 451 6
HLT_j175	210–310	0.132 551
HLT_j260	310–445	0.822 509
HLT_j380	445–	32.9856

(c)

Trigger	p_{T} [GeV]	Luminosity [fb^{-1}]
HLT_j85	100–130	0.007 652 62
HLT_j110	130–200	0.022 802 1
HLT_j175	200–290	0.152 861
HLT_j260	290–400	0.913 47
HLT_j360	400–470	4.808 75
HLT_j420	470–	44.3074

(d)

Trigger	p_{T} [GeV]	Luminosity [fb^{-1}]
HLT_j85	100–130	0.006 865 97
HLT_j110	130–200	0.020 296 2
HLT_j175	200–290	0.148 101
HLT_j260	290–400	0.939 19
HLT_j360	400–470	4.783 68
HLT_j420	470–	58.4501

5.3.1 Data trigger strategy

Besides the selection criteria above, a leading jet trigger strategy is used for the ATLAS data.

The central single-jet High-Level Triggers (HLTs) were used during the data taking, accepting events with leading jets within the pseudorapidity region of $|\eta| < 3.2$ and with E_{T} above certain thresholds specific for the given triggers. The lower-threshold triggers were prescaled—only a predefined fraction of events meeting the trigger criteria were recorded to reduce the event rate to a manageable level. Above a certain threshold, all triggered events—corresponding to unprescaled triggers—were recorded.

This analysis uses one lowest-threshold unprescaled trigger (with thresholds of 380 GeV in 2015, 2016 and 420 GeV in 2017, 2018) and several prescaled triggers (with thresholds as low as 60 GeV in 2016) for each data-taking year (Table 5.2).

For the events to be selected in this analysis, at least one trigger has to be active in the event and the leading jet is required to be within a certain p_{T} range (Table 5.2) corresponding to the trigger efficiency of at least 99.5%. Events corresponding to different triggers are combined using weights equal to the ratio of the effective integrated luminosity of the unprescaled trigger over the luminosity of the active trigger (Table 5.2).

5.3.2 MC cleaning

Pileup in MC is simulated by overlaying the hard-scattering process with minimum bias events. To omit singular MC events containing pileup jets generated with p_{T} above the corresponding JZ slice p_{T} range (Table 5.1), a cut on a ratio

$$p_{\mathrm{T}}^{\mathrm{avg,\,ratio}} = \frac{\left(p_{\mathrm{T1}}^{\mathrm{reco}} + p_{\mathrm{T2}}^{\mathrm{reco}}\right)/2}{p_{\mathrm{T1}}^{\mathrm{truth}}}$$

Table 5.3: Cut thresholds on $p_{\mathrm{T}}^{\mathrm{avg,\,ratio}}$ used in a MC event cleaning.

Slice	$p_{\mathrm{T}}^{\mathrm{avg,\,ratio}}$
JZ2	1.9
JZ3	1.9
JZ4	1.8
JZ5	1.7
JZ6	1.6
JZ7	1.5
JZ8	1.5
JZ9	1.5
JZ10	1.4
JZ11	1.3
JZ12	1.3

of the average transverse momentum of the two leading reconstructed jets $p_{\mathrm{T1}}^{\mathrm{reco}}$ and $p_{\mathrm{T2}}^{\mathrm{reco}}$ over the transverse momentum of the leading truth jet $p_{\mathrm{T1}}^{\mathrm{truth}}$ is used. In each slice of the MC, the value of the cut (ranging from $p_{\mathrm{T}}^{\mathrm{avg,\,ratio}} < 1.3$ for the JZ12 slice to $p_{\mathrm{T}}^{\mathrm{avg,\,ratio}} < 1.9$ for the JZ2 slice) is optimized separately so that a minimal number of events is rejected (Table 5.3).

5.4 Unfolding

The reconstructed spectra are affected by the detector inefficiencies, finite resolution, and other systematic effects. To obtain cross-sections at the particle (truth) level, the detector effects are deconvoluted from the observed spectra using the unfolding procedure based on the MC simulation of the detector response.

5.4.1 Response matrix

To describe the detector response, a response matrix (RM) is built using the reconstructed-level and particle-level MC jets. The RM is filled with events containing truth and reconstructed jets that both pass the selection criteria (Section 5.3).

In addition, the jets are geometrically matched between the truth and reconstructed levels according to their direction in the η–ϕ coordinates using the ΔR_{ij} from Equation (2.1). The truth and reconstructed jets are considered matched if they are the ones closest to each other and the corresponding $\Delta R_{ij} < 0.3$. For the events to be filled to the RM, it is required that the leading and subleading reconstructed jets are matched to the leading and subleading truth jets, no matter their order—the order of the two jets can be swapped between the reconstructed and truth levels due to the resolution effects, allowing for leading-to-subleading and subleading-to-leading matches.

Elements of the RM A_{ij} are defined as the number of matched events generated in a bin i and reconstructed in a bin j.

Dijet events passing the reconstructed-level (truth-level) selection but failing either the truth-level (reconstructed-level) selection or the matching are later

used as purity (efficiency) corrections during the three-step unfolding procedure (Section 5.4.3).

5.4.2 IDS method of data unfolding

The IDS method of data unfolding [69, 70] is used in this analysis as it was shown in previous jet cross-section measurements that it yields the smallest unfolding bias of other tested unfolding methods [71]. The IDS method relies on reasonable modeling of the truth spectra and the detector effects in the MC simulation.

The elements of the unfolding

$$\mathcal{U}_{ij} = \frac{A_{ij}}{\sum_k A_{kj}} \tag{5.3}$$

and folding

$$\tilde{\mathcal{U}}_{ij} = \frac{A_{ij}}{\sum_k A_{ik}}$$

matrices are calculated from the elements of the RM A_{ij}. The sum runs over the truth and reconstructed bins, respectively.

In a series of iterations, an intermediate unfolded spectrum is computed using the unfolding matrix and the truth level MC spectrum is reweighted to match the unfolded data better. The reweighted MC spectrum is then used to modify the RM and to calculate the improved unfolding matrix used in the next iteration.

To prevent the statistical fluctuations from being amplified during the data unfolding and the iterative improvement of the unfolding matrix, the fluctuations are dynamically reduced using a regularization function $f(\Delta x, \sigma, \lambda)$, where Δx is the absolute difference between the data and MC spectra, σ is the corresponding uncertainty, and λ is a regularization parameter. The regularization function $f(\Delta x, \sigma, \lambda)$ is smooth, monotonic, $f(\Delta x = 0, \sigma, \lambda) = 0$ (case of no significant difference between the spectra), and $f(\Delta x \gg \sigma, \sigma, \lambda) = 1$ (case of large significance of the difference).

During the unfolding, a fraction $f(\Delta x, \sigma, \lambda)$ of the data to reconstructed MC spectra difference is distributed to the truth bins using the unfolding matrix $\mathcal{U}_{ij}$ and the rest is left in the original bin (preventing migrations of large but insignificant fluctuations), producing an intermediate unfolded spectrum (the procedure is described in more detail in Ref. [69, 70]).

The difference between the intermediate unfolded and the truth MC spectra is then used to improve the RM—each row of the RM (corresponding to the truth bins) is reweighted according to a fraction $f(\Delta x, \sigma, \lambda)$ of the difference in a truth bin i, distributed to all of the corresponding reconstructed bins j using the folding matrix $\tilde{\mathcal{U}}_{ij}$. A new, improved unfolding matrix is calculated from the improved RM using Equation (5.3).

After the selected number of iterations, the final improved unfolding matrix is used to calculate the final unfolded spectrum.

5.4.3 Three-step unfolding procedure

The number of events N_i^{truth} at the particle level in a bin i is calculated from the number of events N_j^{reco} at the reconstructed level in a bin j in three steps

according to

$$N_i^{\text{truth}} = \sum_j N_j^{\text{reco}} \cdot \mathcal{P}_j \cdot \mathcal{U}_{ij} / \mathcal{E}_i. \tag{5.4}$$

First, the number of events reconstructed in a bin j is multiplied by the matching purity $\mathcal{P}_j$ to account for reconstructed-level events that are not matched to corresponding truth-level events (correcting for reconstructed events originating from pileup or from truth events excluded by the kinematic cuts). The matching purity

$$\mathcal{P}_j = \frac{N_j^{\text{MC, match}}}{N_j^{\text{MC, reco}}}$$

is calculated from MC simulation as a ratio of the number of matched events $N_j^{\text{MC, match}}$ over the total number of reconstructed events $N_j^{\text{MC, reco}}$ in the given bin.

Second, the unfolding matrix $\mathcal{U}_{ij}$ of probabilities of the dijet event reconstructed in a bin j to originate from a truth bin i from Equation (5.3) is calculated within the IDS method after a set amount of iterations. It is applied to the purity-corrected data to account for the event migrations between m_{jj} bins.

Last, the spectrum calculated in the previous step is divided by the matching efficiency $\mathcal{E}_i$ to account for particle-level events originating in a bin i that are not matched to corresponding reconstructed-level events (due to limited detector acceptance and finite resolution). The matching efficiency

$$\mathcal{E}_i = \frac{N_i^{\text{MC, match}}}{N_i^{\text{MC, truth}}}$$

is calculated from MC as a ratio of the number of matched events $N_i^{\text{MC, match}}$ over the total number of truth events $N_i^{\text{MC, truth}}$ in the given bin.

The first m_{jj} bin in each of the y^* and y_{boost} bins (Tables B.1 and B.2) is used during the unfolding to account for migrations of events from and to the final phase space and is not used in the final spectra.

The N_i^{truth} from Equation (5.4) is used as the N_{dijet} in the final cross-section formulae (Equations (5.1) and (5.2)).

5.4.4 Statistical uncertainty

To account for different triggers and JZ slices contributing to the spectra with various weights and to account for event migrations between bins during the unfolding, a statistical uncertainty of the final dijet cross-sections is estimated using the bootstrap method. The effects of the statistical uncertainties of the data and MC simulation are evaluated separately.

For the data, 100 toy spectra are created—the weight of each event contributing to the nominal spectrum is varied 100 times using the Poisson distribution with a mean equal to one. Each toy spectrum is unfolded using the nominal RM. In each bin, the statistical uncertainty corresponding to the data is estimated as a root mean square (RMS) error calculated from the unfolded toy spectra.

Similarly, for the MC simulation, the weights of events contributing to the nominal RM are varied using the Poisson distribution with a mean equal to one, creating 100 toy RMs. The nominal data spectrum is then unfolded using the toy

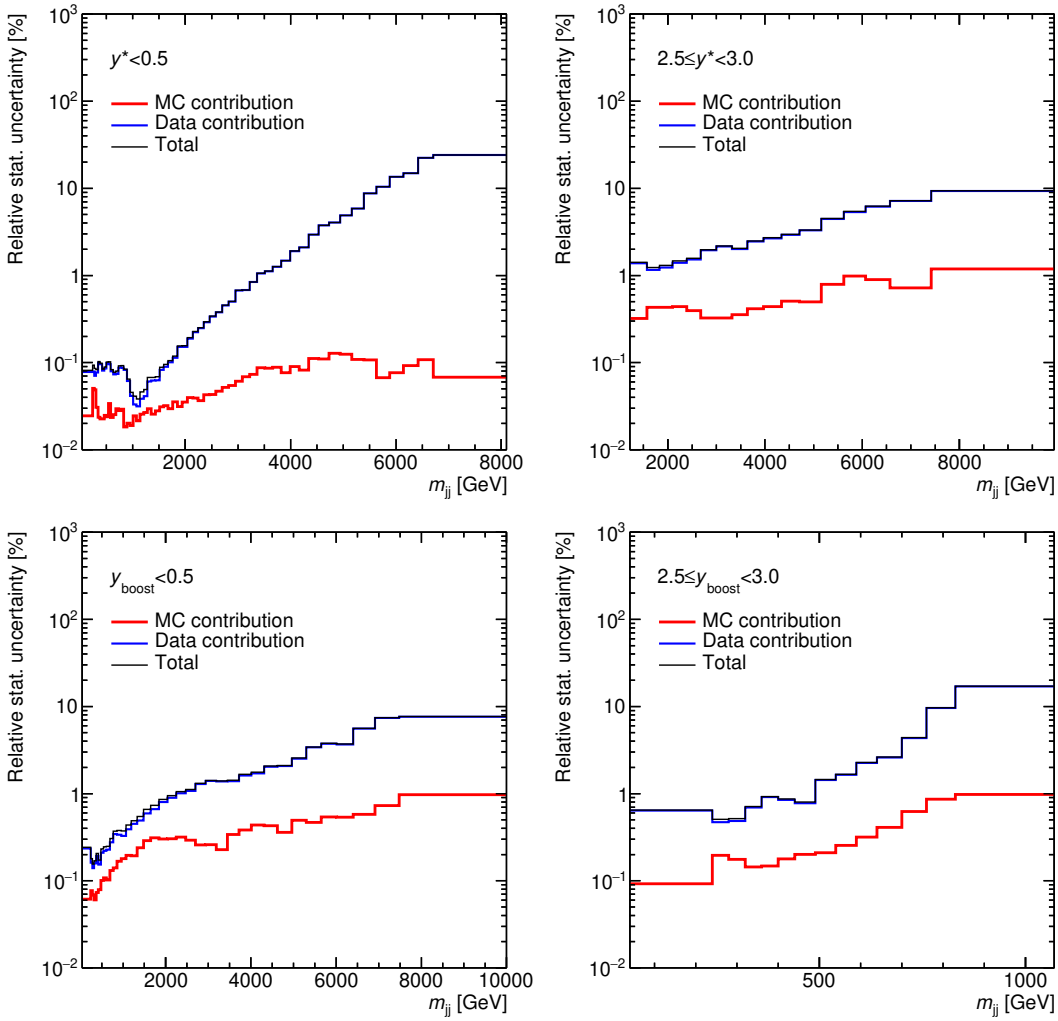

Figure 5.2: The statistical uncertainty corresponding to the MC simulation (MC contribution), data (Data contribution), and total uncertainty (Total) using the IDS unfolding method in the first and last y^* and y_{boost} bins. Plots for the remaining bins can be found in Appendix B, Figures B.1 and B.2.

RMs, resulting in 100 unfolded spectra. Again, the statistical uncertainty—this time corresponding to the MC contribution—is estimated as a RMS error.

Contributions of the data and MC are added in quadrature to obtain the total statistical uncertainty (Figure 5.2). The dominant contribution comes from the data. The total statistical uncertainty stays at a sub-percent level up to a few TeV of dijet mass in most of the y^* and y_{boost} bins and reaches up to few tens of percent in some of the last m_{jj} bins.

5.4.5 Bias of the unfolding

To determine the shape uncertainty of the unfolded spectrum, a data-driven closure test is used [69, 71]. It is assumed that the shape difference between the data and MC spectra on the reconstructed level is caused by improper MC modeling at the truth level.

First, the ratio of the data over the reconstructed-level MC spectra is fitted

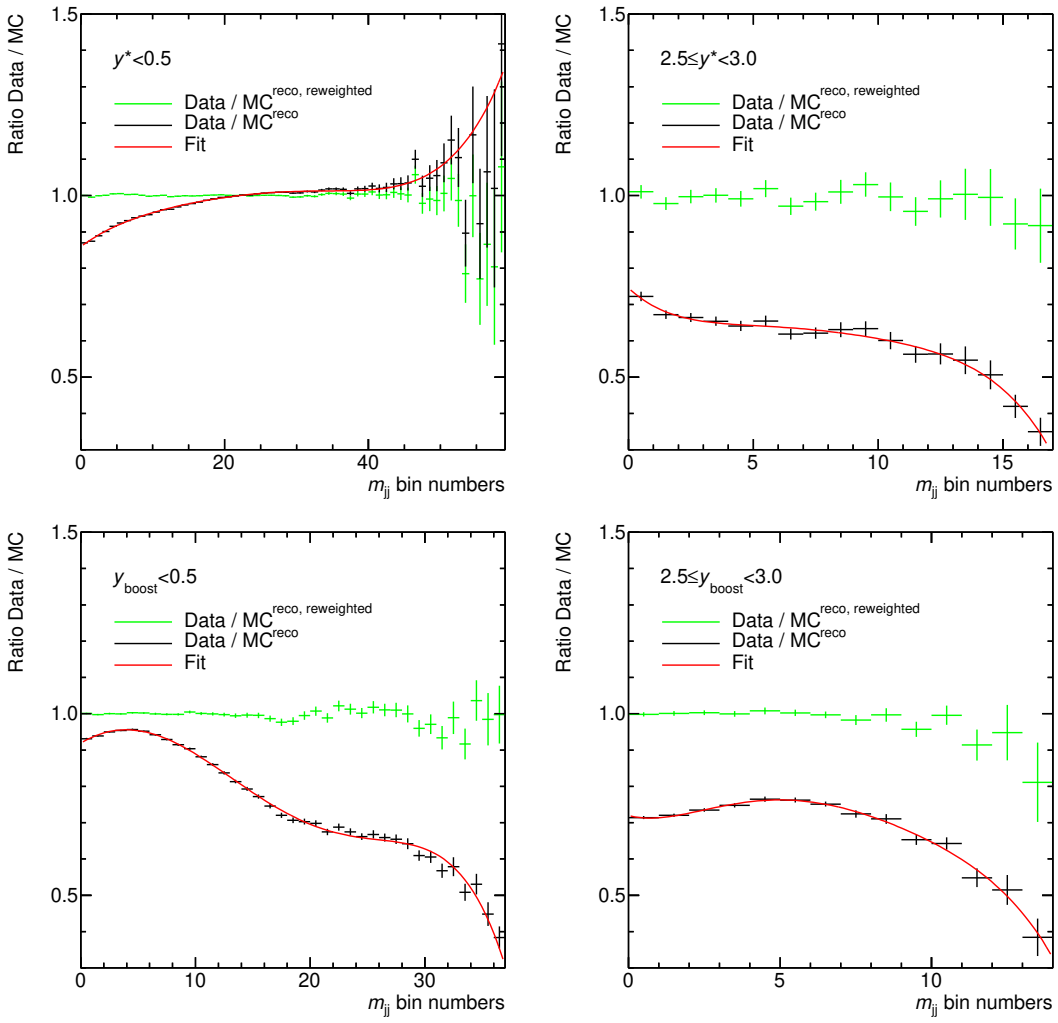

Figure 5.3: The ratio of the data and MC spectra on the reconstructed level (Data / $\mathrm{MC}^{\mathrm{reco}}$) fitted by a smooth function (Fit) and the ratio of the data and reweighted MC spectra (Data / $\mathrm{MC}^{\mathrm{reco,\ reweighted}}$) in the first and last y^* and y_{boost} bins. Plots for the remaining bins can be found in Appendix B, Figures B.3 and B.4.

by a smooth function—fifth order polynomial is used. To improve fit results, ratios are plotted in an equidistant binning using bin numbers instead of actual m_{jj} values (Figure 5.3).

The nominal RM is then reweighted using the fit function by multiplying the RM rows corresponding to the true m_{jj} bins. Reweighted truth-level and reconstructed-level MC spectra are obtained by projecting the RM onto the truth-level and reconstructed-level axes, respectively. This MC modification significantly improves the agreement between the data and MC spectra on the reconstructed level (Figure 5.3)—for the closure test, the agreement does not need to be perfect.

The reweighted reconstructed MC spectrum is then unfolded using the unfolding matrix calculated from the nominal RM and compared to the reweighted truth MC spectrum. This difference is interpreted as a bias of the unfolding (Figure 5.4).

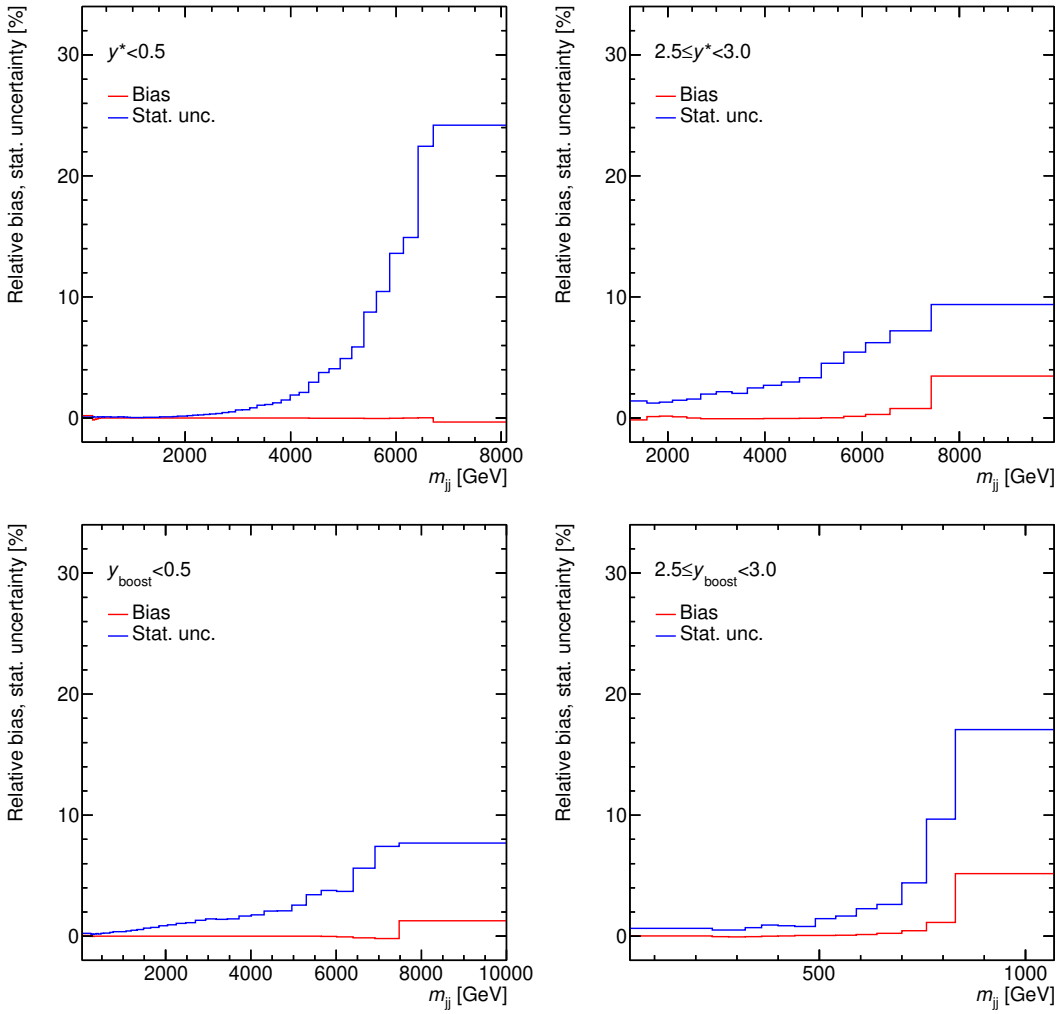

Figure 5.4: Comparison of the smoothed unfolding bias estimate (Bias) and the unfolded spectra statistical uncertainty (Stat. unc.) using one iteration (two iterations) of the IDS unfolding method for the y^* (y_{boost}) variable in the first and last y^* and y_{boost} bins. Plots for the remaining bins can be found in Appendix B, Figures B.5 and B.6.

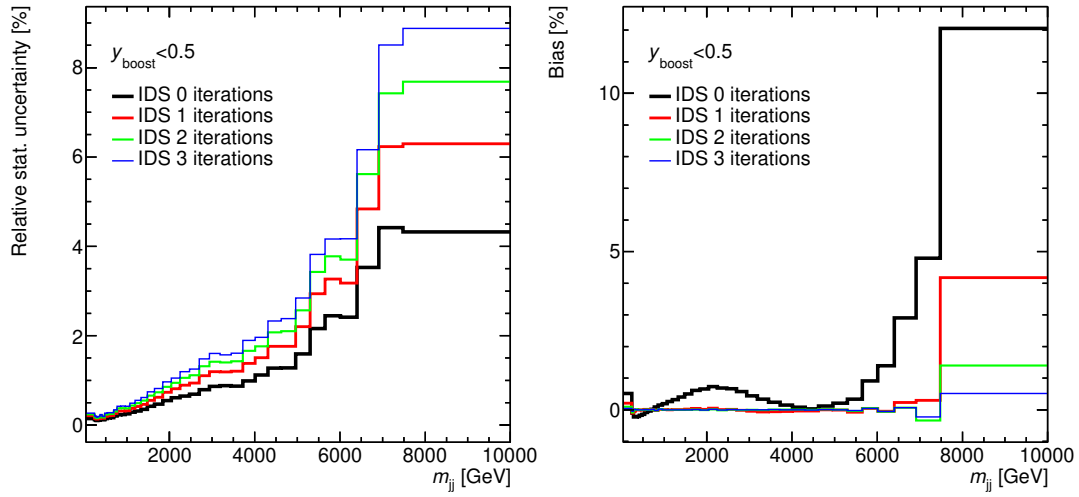

(a) (b)

Figure 5.5: (a) The total statistical uncertainty of the unfolded spectrum and (b) the bias of the unfolding evaluated using zero to three iterations of the IDS unfolding method.

5.4.6 Number of IDS iterations

Both the statistical uncertainty of the unfolded spectrum and the bias of the unfolding are evaluated using zero to three iterations of the IDS unfolding method (Figures 5.5a and 5.5b). With the increasing number of unfolding iterations, the statistical uncertainty increases and the bias decreases. To determine the optimal unfolding parameters, the bias is compared to the statistical uncertainty for each of the selected numbers of iterations (Figure 5.4). Due to clear interpretation and reliable estimation of the statistical uncertainty using the bootstrap method, a large statistical uncertainty is preferred over a large bias. Due to this reason, one iteration of the IDS unfolding method is chosen for the y^* variable and two iterations are chosen for the y_{boost} variable.

5.5 Systematic uncertainties

There are two main sources of the systematic uncertainty of the dijet cross-section measurement—the JES and JER uncertainties. Also, the unfolding bias and precision of the luminosity measurement contribute to the total systematic uncertainty.

5.5.1 Jet energy scale

The JES calibration (Section 4.2) uncertainty is the dominant source of the systematic uncertainty in the dijet cross-section measurement. It was derived using various techniques and measurements from the 2015–2017 ATLAS data [57, 64]. The uncertainty components used in this analysis (Table 5.4) are similar to the ones listed in Ref. [57].

In total, 1182 components of the JES uncertainty are considered—coming from *in situ* measurements, pileup and flavor dependence, and other sources (Table 5.4 and Figure 5.6). The majority of the components correspond to the statistical uncertainty of the η intercalibration modeling uncertainty. The total statistical uncertainty of the η intercalibration is replaced by the 532 individual components (separately for the years 2015–2016 and 2017–2018) corresponding to the p_{T}–η bins used by the η intercalibration technique, which are treated as fully uncorrelated.

All JES uncertainty components are propagated through the unfolding using the MC simulation. For each component, a reconstructed jet p_{T} and energy are shifted up and down by one standard deviation of the corresponding nuisance parameter (NP). The m_{jj} spectra are then recalculated using the shifted p_{T} and energy values and unfolded using the nominal RM (created using the nominal, unaltered p_{T} and energy). The difference between the nominal spectrum unfolded using the nominal RM and the systematically shifted unfolded spectrum is then interpreted as the systematic uncertainty of the cross-section corresponding to the given NP.

Concerning the values derived in Ref. [57], the current measurement uses an improved set of uncertainties (Figure 5.7)—namely the uncertainties related to the extrapolation of the single-particle response at high p_{T} to jets and related to the different calorimeter response to the gluon-initiated and quark-initiated jets [81, 82].

The total JES systematic uncertainty is obtained as a quadrature sum of all of its components. It is at a level of approximately 5–10% throughout most of the spectra, reaching up to approximately 15–20% in some of the last m_{jj} bins.

Recently, a new set of JES systematic uncertainties was released, reducing the total uncertainty even further (especially for high-p_{T} jets) by combining the single particle response and the p_{T}-balance methods. The new components will be propagated through the unfolding procedure to update the values presented in this text for the upcoming publication.

5.5.2 Jet energy resolution

A relative JER of the jet transverse momentum p_{T} is described using the quadrature sum $\oplus$ of the noise N, stochastic S, and constant C terms as

$$\frac{\sigma(p_{\mathrm{T}})}{p_{\mathrm{T}}} = \frac{N}{p_{\mathrm{T}}} \oplus \frac{S}{\sqrt{p_{\mathrm{T}}}} \oplus C.$$

The noise parameter corresponds to the contributions of pileup and electronic noise. The stochastic parameter corresponds to the statistical fluctuations of the deposited energy in the detector. The constant term corresponds to the fluctuations caused by effects like the non-uniformity of the response across the detector and the energy deposition in a passive material.

The 2017 data were used to measure the JER [57]. The stochastic and constant terms were determined using dijet systems by balancing a well-calibrated jet in the central calorimeter region against a probe jet, for which the resolution was measured. The noise term was determined using the random cones method (more in Ref. [57]).

Table 5.4: Components of the JES systematic uncertainty (based on Ref. [57]).

Component	Description
η intercalibration	
Syst. mismodeling	Envelope of the MC, pileup, and event topology variations
Non-closure	Non-closure at high energy and at $\eta \sim \pm 2.4$ (3 components)
Non-closure, 2018	Non-closure at $\eta \sim \pm 1.5$ due to TileCal calibration, 2018 only
Statistical component	Statistical uncertainty (1064 components)
Z+jet p_{T} balance	
Electron scale	Uncertainty of the electron energy scale
Electron resolution	Uncertainty of the electron energy resolution
Muon scale	Uncertainty of the muon energy scale
Muon resolution	Uncertainty of the muon energy resolution
JVT	Jet vertex tagger uncertainty
MC generator	Difference between MC event generators
Showering and topology	Modeling energy flow and distribution in and around a jet
Subleading jet veto	Radiation suppression through second-jet veto
$\Delta\phi$ cut	Variation of $\Delta\phi$ between the jet and Z boson
Statistical component	Statistical uncertainty (28 components)
γ+jet p_{T} balance	
Photon scale	Uncertainty of the photon energy scale
Photon resolution	Uncertainty of the photon energy resolution
Photon purity	Purity of the sample used for the γ+jet balance
JVT	Jet vertex tagger uncertainty
MC generator	Difference between MC event generators
Showering and topology	Modeling energy flow and distribution in and around a jet
Subleading jet veto	Radiation suppression through second-jet veto
$\Delta\phi$ cut	Variation of $\Delta\phi$ between the jet and photon
Statistical component	Statistical uncertainty (16 components)
Multijet p_{T} balance	
α selection	Angle between leading jet and recoil system
β selection	Angle between leading jet and closest subleading jet
p_{T} asymmetry selection	Second jet's p_{T} contribution to the recoil system
Fragmentation	Jet fragmentation modeling uncertainty
JVT	Jet vertex tagger uncertainty
Jet p_{T}	Jet p_{T} threshold
Statistical component	Statistical uncertainty (28 components)
Pileup	
μ offset	Uncertainty of the μ modeling in MC simulation
NPV offset	Uncertainty of the NPV modeling in MC simulation
p_{T} dependence	Uncertainty of the residual p_{T} dependence
ρ topology	Uncertainty of the per-event p_{T} density modeling in MC simulation
Jet flavor	
Flavor composition	Uncertainty of the proportional sample composition of quarks and gluons
Flavor response	Uncertainty of the response of gluon-initiated jets
GenShower, hadronization, shower	Uncertainty of the hadronization and showering modeling
Punch-through	Uncertainty of the global sequential calibration punch-through correction
Single particle response	High-p_{T} jet uncertainty from single particle and test beam measurements

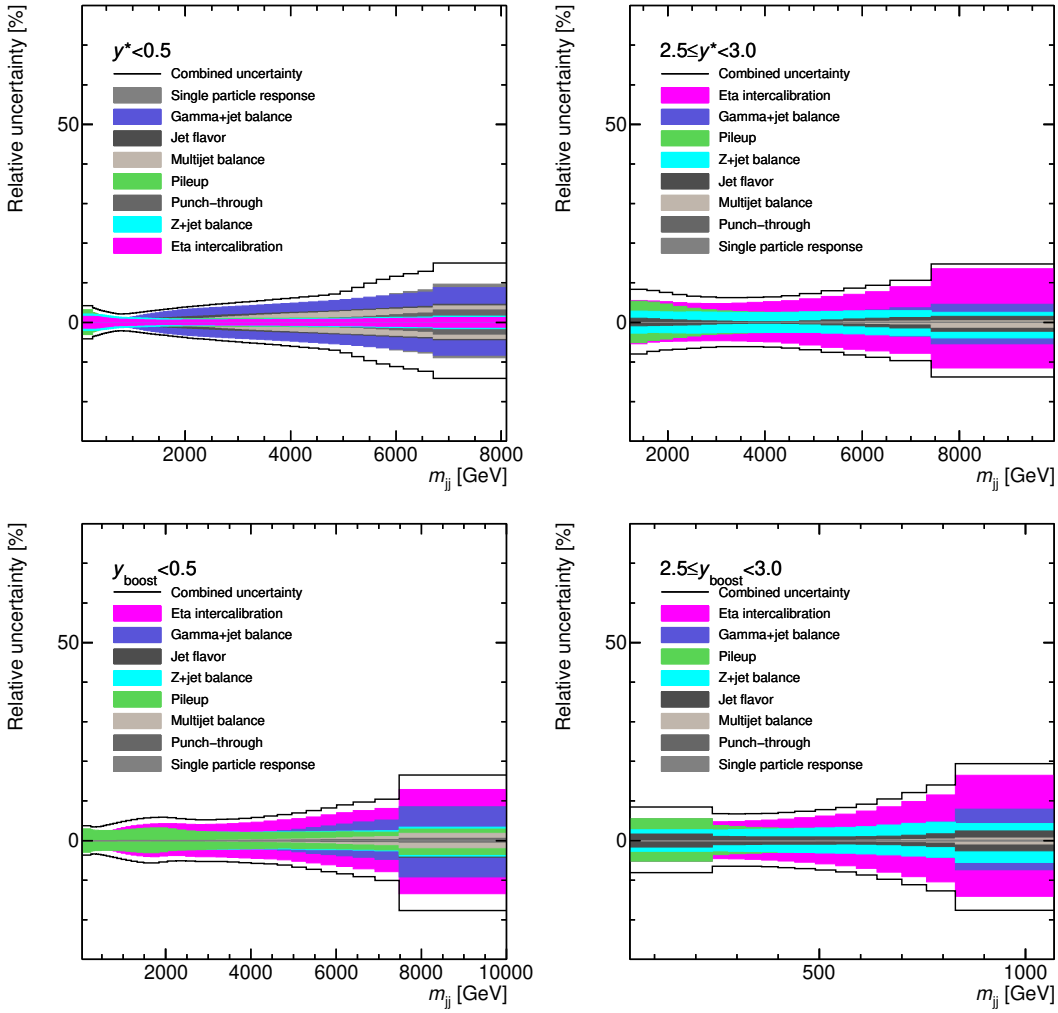

Figure 5.6: Components of the JES uncertainty of the dijet cross-section in the first and last y^* and y_{boost} bins. Plots for the remaining bins can be found in Appendix B, Figures B.7 and B.8.

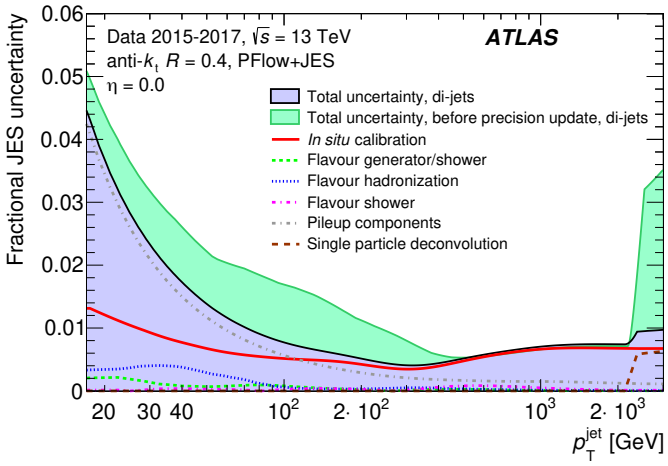

Figure 5.7: The JES uncertainty improvement of the flavor response and single-particle deconvolution components as a function of a jet transverse momentum evaluated using dijet events as described in Ref. [81].

In total, 34 components of the JER uncertainty are considered—1 component corresponds to the absolute JER difference between the data and MC simulation, 19 to the dijet balance method, and 14 to the noise term measurement (Table 5.5 and Figure 5.8).

To propagate the effects of the JER uncertainty, first, it is ensured that the resolution in the MC simulation matches the one in the data. In p_{T} regions in which the resolution in data is worse than in simulation, the MC sample is smeared until its average resolution matches the data. In the opposite case—in p_{T} regions of better data resolution compared to MC—the data remain unaltered and the difference of the resolution in the data and MC is applied as an additional systematic uncertainty.

The JER uncertainty components are propagated to the unfolded level by smearing jets according to a Gaussian function with a width σ_{smear},

$$\sigma^2_{\mathrm{smear}} = (\sigma_{\mathrm{nominal}} + |\sigma_{\mathrm{NP}}|)^2 - \sigma^2_{\mathrm{nominal}},$$

where $\sigma_{\mathrm{nominal}}$ is the nominal JER of the MC (after the smearing to match the data) and σ_{NP} is the variation of the given JER component at a one-sigma level [57].

To account for anti-correlations if one component is positive in part of the phase space and negative in another, the JER degradation is propagated by smearing the p_{T} and energy of jets in the MC used as pseudo-data. In contrast, the JER improvement is propagated by smearing the MC jets used for the RM construction. The difference between the modified pseudo-data spectrum unfolded by the varied RM and the nominal spectrum unfolded by the nominal RM is then interpreted as the corresponding JER systematic uncertainty.

The total JER systematic uncertainty is obtained as a quadrature sum of all of its components.

Recently, a bug was discovered in the release of the MC samples used for the JER systematic uncertainty evaluation, greatly increasing the effects. The values will be recalculated for the upcoming publication using new MC samples—a significant reduction of the JER uncertainty is expected.

5.5.3 Binning

During the binning determination, statistical effects of the MC in the last m_{jj} bins were studied using systematic uncertainties. If needed, the binning was adjusted so that the MC statistical uncertainty does not have too large of an effect on the estimation of the systematic uncertainties.

Multiple components of the JES systematic uncertainty were evaluated in the initial binning, including an estimate of their statistical uncertainties using the bootstrap method. Each event contributing to the systematically varied reconstructed spectrum is weighted 100 times according to the Poisson distribution with a mean equal to one, resulting in 100 replicas of the spectrum. Spectra are unfolded using the nominal RM and compared to the nominal spectrum unfolded using the nominal RM, producing 100 replicas of the corresponding systematic uncertainty estimate. In each bin, the statistical uncertainty is calculated as a RMS error from the replicas.

Table 5.5: Components of the JER systematic uncertainty.

Component	Description
Dijet balance	
Non-closure	MC vs *in situ* non-closure
JES NP	Propagation of JES nuisance parameters (3 components)
JVT	Jet vertex tagger uncertainty
MC generator	Difference between MC event generators
p_{T3}, $\Delta\phi$ cuts	Limit on the p_{T} of the third jet and $\Delta\phi$ of the two leading jets
Statistical component	Statistical uncertainty (12 components)
Noise term	
Constituent scale	Constituent energy scale (2 components)
Scale conversion	JES conversion factor (2 components)
Fit error	Noise fit error (2 components)
Fit range	Noise fit range (2 components)
Non-closure	MC vs *in situ* non-closure (2 components)
Fit instability	Noise fit instability in zero pileup (2 components)
No-pileup uncertainty	Noise term in zero pileup (2 components)
Data vs MC	Absolute JER difference between data and MC simulation

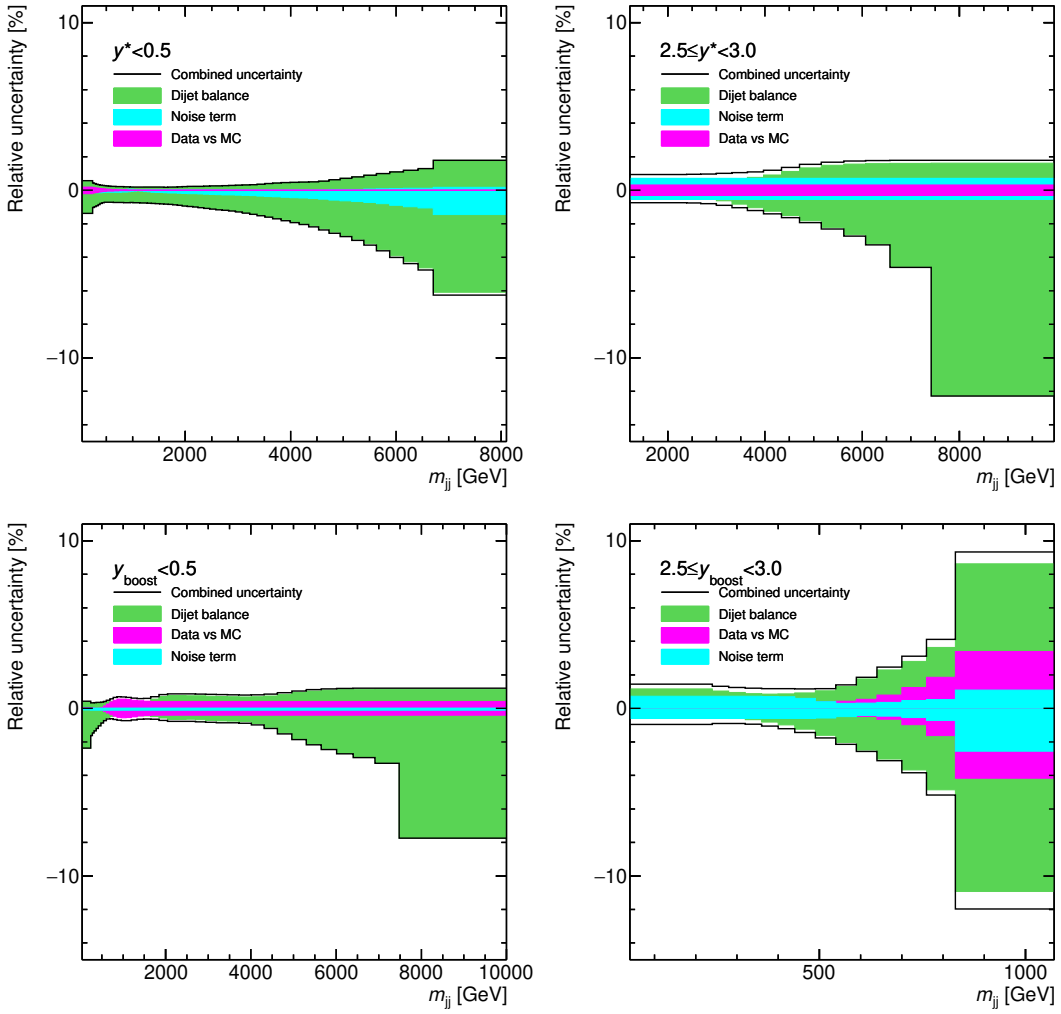

Figure 5.8: Components of the JER uncertainty of the dijet cross-section in the first and last y^* and y_{boost} bins. Plots for the remaining bins can be found in Appendix B, Figures B.9 and B.10.

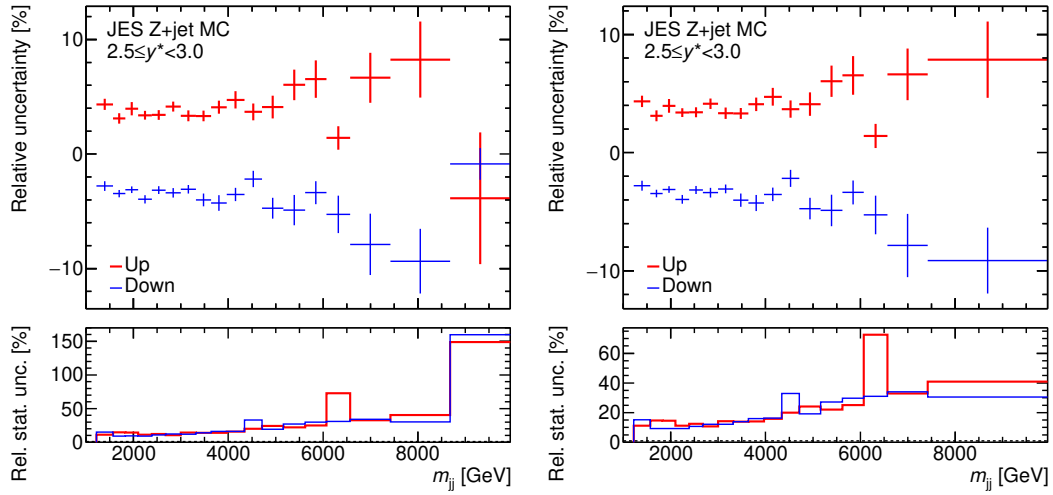

(a) (b)

Figure 5.9: Example of one component of the JES systematic uncertainty (top) and its relative statistical uncertainty calculated using the bootstrap method (bottom) in the last y^* bin (a) in the initial binning and (b) after merging of the last two m_{jj} bins.

In few cases of unreasonably large statistical fluctuations and corresponding statistical uncertainties in the last m_{jj} bin across the studied systematic components, the last two bins were merged (Figures 5.9a and 5.9b), resulting in the final binning used in the analysis (Tables B.1 and B.2).

5.5.4 Smoothing of systematic uncertainties

Systematic uncertainties propagated through the unfolding can suffer from statistical fluctuations. To minimize the effects of the fluctuations, a smoothing procedure is used (Figures 5.10a and 5.10b).

First, the statistical uncertainty of the systematic variations is estimated using the bootstrap method. For each component of the JES and JER systematic uncertainty, 100 pseudo-experiments are created by weighting the events using the Poisson distribution with a mean equal to one and the corresponding statistical uncertainty is calculated as a RMS error separately in each m_{jj} bin. The bootstrap method conserves correlations between the nominal and varied spectra, as for a given event, the set of 100 Poisson weights is always the same (the set is seeded using the run number, event number, and MC dataset identifier), no matter if the event is filled to the nominal or varied spectrum.

Second, the statistical significance of each systematic component is calculated in each m_{jj} bin. Neighboring bins are combined until the significance is larger than two standard deviations. Bins are combined independently in two directions—starting from the leftmost and rightmost bins. The combination that conserves the most bins is used.

Last, the Gaussian kernel smoothing procedure is applied to the rebinned systematic variations. During this process, the original binning is restored. Each m_{jj} bin is recalculated as a weighted average of all m_{jj} bins in the given y^* or

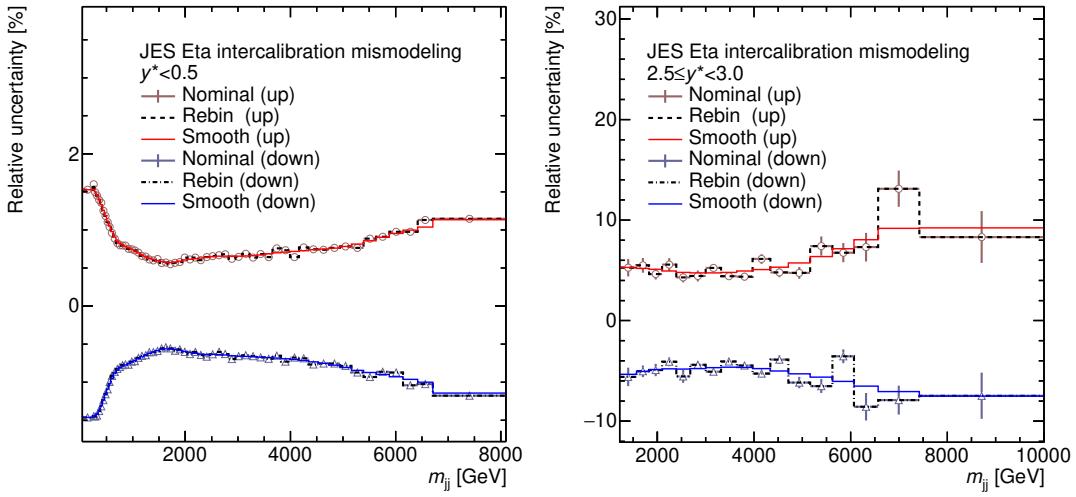

(a) (b)

Figure 5.10: Example of the smoothing procedure for one component of the JES systematic uncertainty. The nominal value of the relative systematic uncertainty (Nominal), rebinned uncertainty until significant (Rebin), and uncertainty after the Gaussian kernel smoothing (Smooth) are plotted. Results are shown for the first and last y^* bins.

y_{boost} bin. Weight w_i of the bin i with center x_i is calculated according to the Gaussian function

$$w_i = \exp\left(-\frac{(x - x_i)^2}{2b^2}\right)$$

centered around the center x of the bin, the content of which is being recalculated. The width b of the Gaussian function varies across the spectra and depends linearly on the bin position x to best reflect the non-equidistant m_{jj} binning—the linear function parameters are derived separately in each of the y^* and y_{boost} bins by fitting the dependence of the bin widths on the bin centers (excluding the first and the last m_{jj} bins from the fit).

5.5.5 Other systematic uncertainties

Besides the JES and JER, the bias of the unfolding procedure and luminosity uncertainty are considered. The effect of TileCal modules that were disabled during the Run 2 data taking will be included in the upcoming publication. Other potential sources of systematic uncertainty were studied and they yielded negligible effects.

Unfolding bias

The bias of the IDS unfolding method (Section 5.4.5) is smoothed in each y^* and y_{boost} bin in a similar way as the JES and JER uncertainty components—using the bootstrap method to estimate the statistical uncertainty of the bias, rebinning, and Gaussian kernel smoothing. The smoothed bias is applied both

in a positive and negative sense to the final cross-sections as a corresponding systematic uncertainty.

Luminosity uncertainty

The total integrated luminosity of the Run 2 p–p collision dataset at 13 TeV passing the standard data quality requirements was measured to be 139.0 ± 2.4 fb^{-1} [73]. The corresponding relative cross-section uncertainty of 1.7% is used across all m_{jj}, y^*, and y_{boost} bins.

As the recent ATLAS Run 2 luminosity measurement improves the result to 140.07 ± 1.17 fb^{-1} corresponding to 0.83% uncertainty [83], the cross-sections and their total uncertainties will be recalculated for the upcoming publication according to the updated luminosity value.

5.5.6 Total systematic uncertainty

The components of the JES and JER systematic uncertainties, the bias of the unfolding method, and the uncertainty of the luminosity measurements are summed in quadrature, separately in all m_{jj} bins (Figure 5.11). The JES being the dominant source, the total uncertainty of the dijet cross-sections is at a level of approximately 5–10% throughout most of the spectra, reaching up to approximately 15–20% in some of the last m_{jj} bins.

As the effects of multiple systematic uncertainty sources were recently reduced (as described in previous sections), the total systematic uncertainty will be recalculated for the upcoming publication and will be reduced as well.

5.6 Results

The two double-differential dijet cross-sections are measured as functions of m_{jj} and either y^* or y_{boost} (Section 5.6). The measurement uses the PFlow jets in 13 TeV p–p collisions recorded during the LHC Run 2 data-taking period, corresponding to the integrated luminosity of 139 fb^{-1}. The jets are reconstructed using the anti-k_{T} clustering algorithm with a radius parameter of $R = 0.4$.

The ATLAS data are unfolded to the particle level using the IDS unfolding method. The JES, JER, and unfolding systematic uncertainties are evaluated using the Pythia 8 MC generated events and are propagated to the unfolded level. The total statistical uncertainty contains both the data and MC contributions.

The results are presented in six equidistant y^* and y_{boost} bins of 0.5 width in a range of $y^* < 3.0$ and $y_{\text{boost}} < 3.0$ and m_{jj} bins of variable width covering a 240 GeV to 10 TeV range.

Compared to the previous ATLAS 13 TeV measurement of the dijet cross-section, the current one provides increased statistics, reduced systematic uncertainties, and an additional angular variable y_{boost}.

The precision of the measurement will be further improved using new, reduced systematic uncertainties corresponding to the luminosity measurement and improved JES and JER uncertainties.

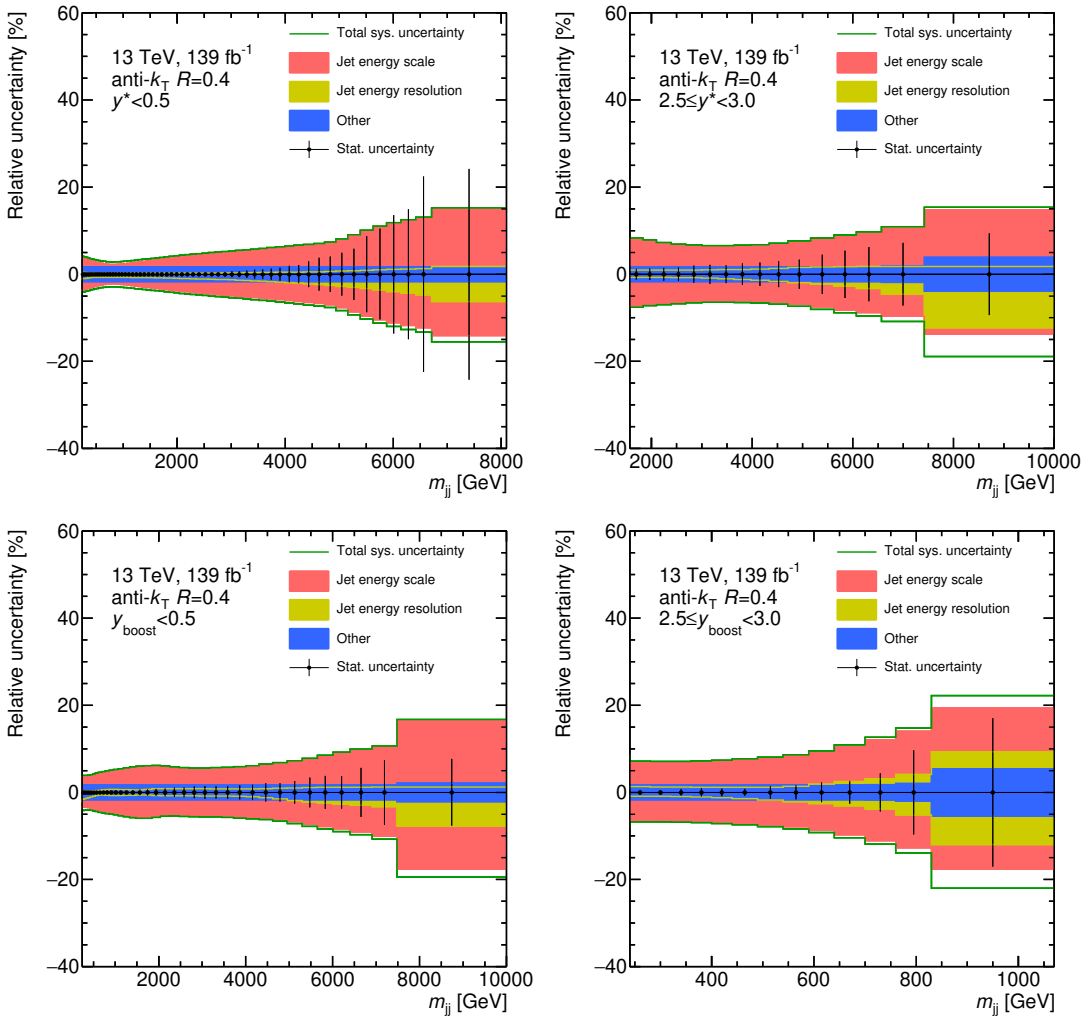

Figure 5.11: Components of the total systematic uncertainty (color bands) and the total statistical uncertainty (black points) of the dijet cross-section in the first and last y^* and y_{boost} bins. Plots for the remaining bins can be found in Appendix B, Figures B.11 and B.12.

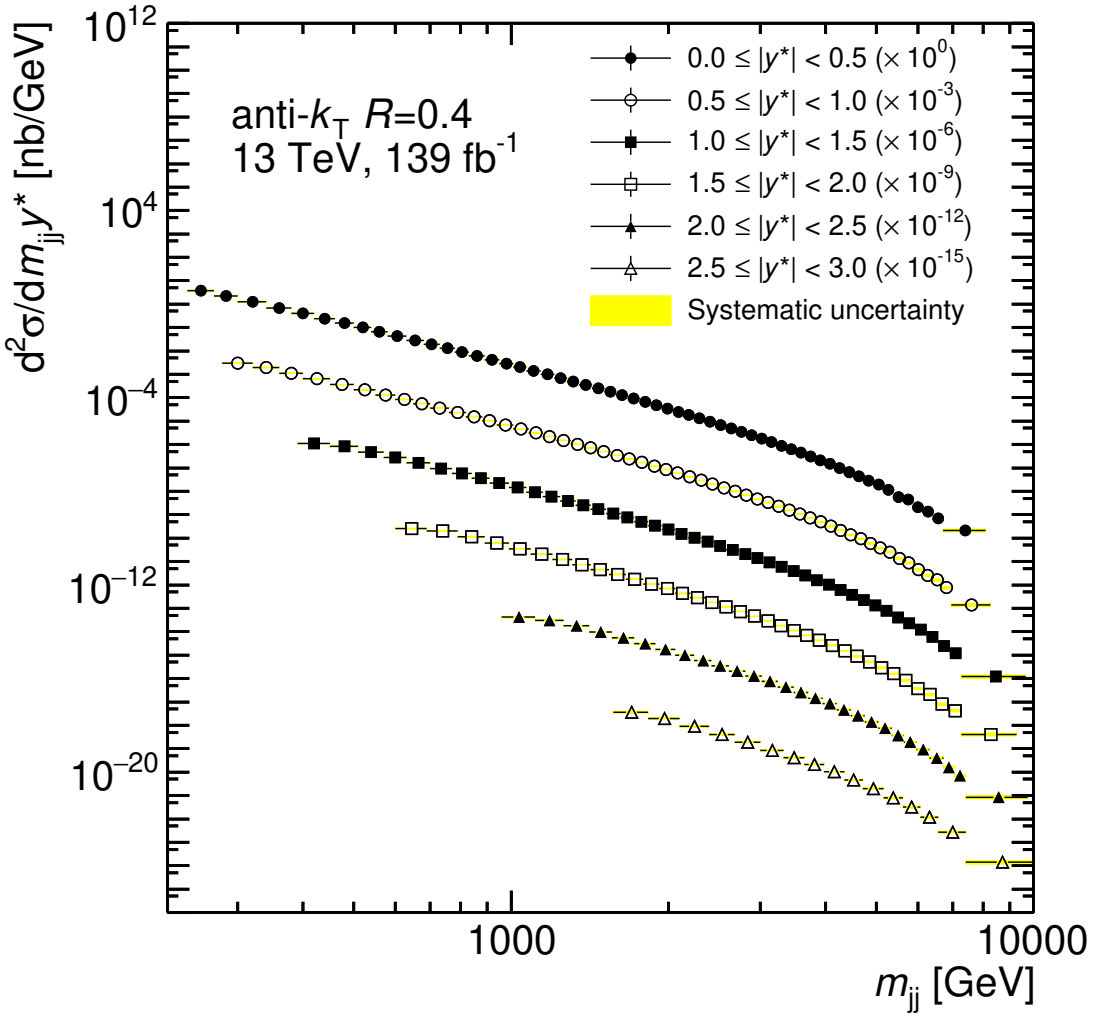

Figure 5.12: The inclusive dijet cross-section as a function of the dijet mass m_{jj} in all six y^* bins for anti-k_{T} PFlow jets with $R = 0.4$. Statistical uncertainties are smaller than the data-point symbols. Total systematic uncertainties are plotted as yellow areas.

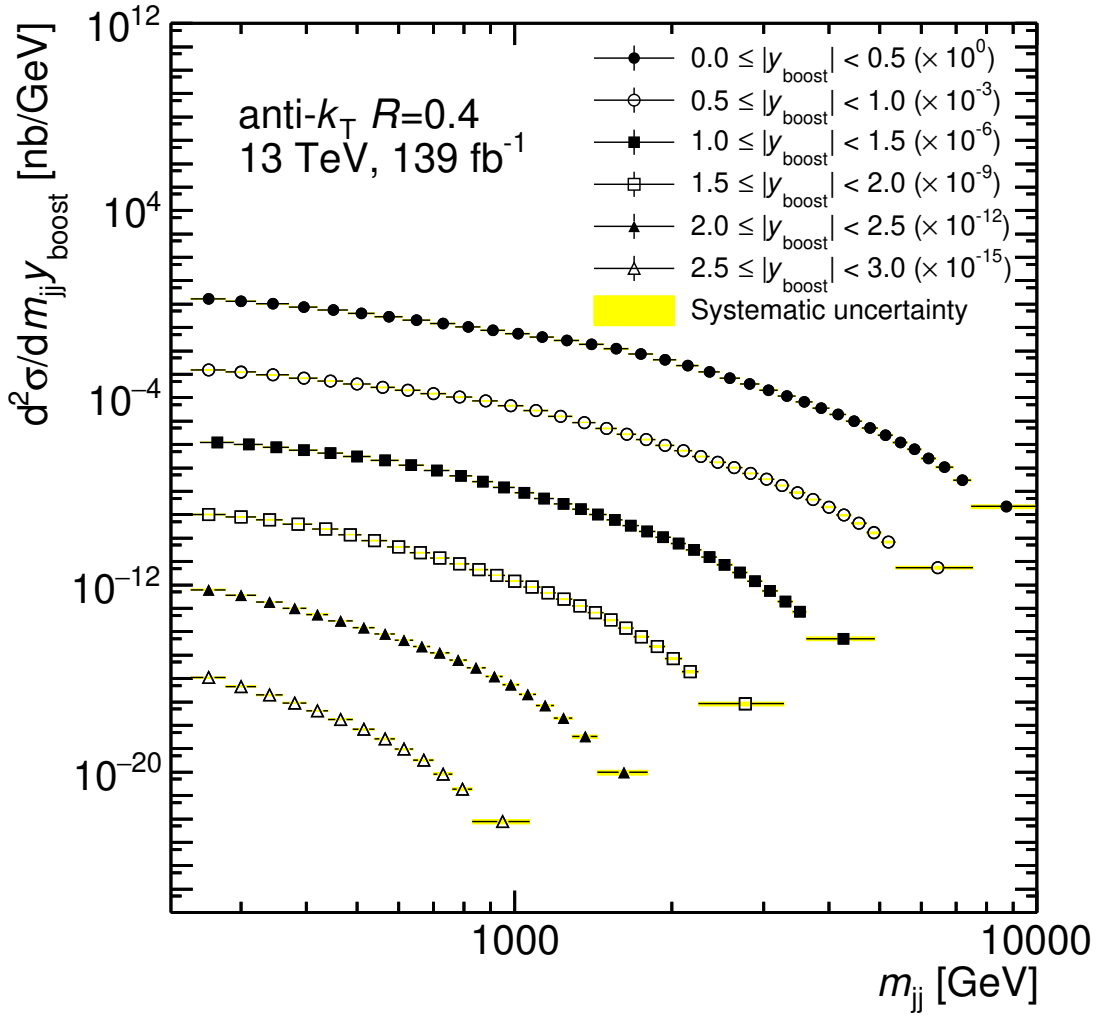

Figure 5.13: The inclusive dijet cross-section as a function of the dijet mass m_{jj} in all six y_{boost} bins for anti-k_{T} PFlow jets with $R = 0.4$. Statistical uncertainties are smaller than the data-point symbols. Total systematic uncertainties are plotted as yellow areas.

Conclusion

The author's contributions to the operation of the ATLAS Tile Calorimeter (TileCal) and to the dijet cross-section measurement are presented.

TileCal is described in detail, including its structure, energy and time calibration and monitoring—the main focus is on the time calibration using jets in collision data. Calorimeter cells contributing to well-reconstructed jets are used to derive time-phase constants in all of the TileCal readout channels. The process of the time calibration during the LHC Run 3 is summarised.

Besides the time calibration using jets, various timing issues and their corrections are presented. The bunch-crossing offset problem is corrected using a specialized software tool developed during a LHC technical stop before Run 3. The LB−EB offset observed in 2022 and 2023 was monitored using collision data and corrected during the data reprocessing at the end of each year. The origin of the problem was fixed before the 2024 data taking. The problem of double peaks in the timing of some of the TileCal readout channels was considered during the calibration in 2023 and an improved version of the monitoring tool is currently in use.

The current state of the double-differential cross-section measurement of the inclusive dijet production in 13 TeV p–p collisions at LHC is summarised. The reconstructed spectra are corrected to the particle level using the Iterative, Dynamically Stabilized method of data unfolding. The final cross-sections are presented as functions of the invariant mass m_{jj} of the dijet system in six equidistant y^* and y_{boost} bins. The total statistical uncertainty—consisting of the data and MC contributions—is evaluated at the unfolded level. Contributions of the jet energy scale (JES), jet energy resolution (JER), unfolding, and the luminosity measurement are included in the systematic uncertainty.

Compared to the previous dijet measurement at ATLAS, the current measurement provides improved statistics, improved systematic uncertainties, and an additional rapidity variable y_{boost}. The precision of the measurement will be further improved using new, reduced systematic uncertainties corresponding to the luminosity measurement and improved JES and JER uncertainties.

Bibliography

[1] J. Hořejší, *Fundamentals of electroweak theory*, Karolinum Press, 2002, ISBN: 80-246-0639-9.

[2] J. Campbell, J. Huston, and F. Krauss, *The Black Book of Quantum Chromodynamics: a Primer for the LHC Era*, Oxford University Press, 2018, ISBN: 978-0-19-965274-7.

[3] P. Skands, *Introduction to QCD*, 2013, arXiv:1207.2389 [hep-ph].

[4] J. Chýla, *Quarks, partons and Quantum Chromodynamics*, 2009.

[5] R. L. Workman et al. (Particle Data Group), *Review of Particle Physics*, Prog. Theor. Exp. Phys. 2022:083C01, 2022.

[6] T. Kinoshita, *Mass singularities of Feynman amplitudes*, J. Math. Phys. 3:650–677, 1962.

[7] T. D. Lee and M. Nauenberg, *Degenerate Systems and Mass Singularities*, Phys. Rev. 133:B1549–B1562, 6B 1964.

[8] N. Nakanishi, *General Theory of Infrared Divergence*, Progress of Theoretical Physics 19 2:159–168, 1958, ISSN: 0033-068X.

[9] G. Altarelli and G. Parisi, *Asymptotic Freedom in Parton Language*, Nucl. Phys. B 126:298–318, 1977.

[10] T. Song and H. Berrehrah, *Hadronization time of heavy quarks in nuclear matter*, Phys. Rev. C 94:034901, 3 2016.

[11] B. Andersson et al., *Parton fragmentation and string dynamics*, Phys. Rept. 97:31–145, 1983.

[12] T. Sjöstrand, S. Mrenna, and P. Skands, *A brief introduction to PYTHIA 8.1*, Computer Physics Communications 178 11:852–867, 2008, ISSN: 0010-4655.

[13] B. Andersson, G. Gustafson, and T. Sjöstrand, *Baryon Production in Jet Fragmentation and γ-Decay*, Physica Scripta 32 6:574, 1985.

[14] A. Buckley et al., *General-purpose event generators for LHC physics*, Physics Reports 504 5:145–233, 2011, ISSN: 0370-1573.

[15] L. Evans and P. Bryant, *LHC Machine*, JINST 3:S08001, 2008.

[16] CERN, *The CERN accelerator complex – August 2018*, 2018, https://cds.cern.ch/record/2636343.

[17] ATLAS Collaboration, *The ATLAS Experiment at the CERN Large Hadron Collider*, JINST 3:S08003, 2008.

[18] ATLAS Collaboration, *ATLAS Inner Detector: Technical Design Report, Volume 1*, ATLAS-TDR-4; CERN-LHCC-97-016, 1997.

[19] ATLAS Collaboration, *ATLAS Inner Detector: Technical Design Report, Volume 2*, ATLAS-TDR-5, CERN-LHCC-97-017, 1997.

[20] ATLAS Collaboration, *Alignment of the ATLAS Inner Detector in Run-2*, Eur. Phys. J. C 80:1194, 2020, arXiv:2007.07624 [hep-ex].

[21] H. H. J. ten Kate, *ATLAS superconducting toroids and solenoid*, IEEE Trans. Appl. Supercond. 15 2 pt.2:1267–1270, 2005.

[22] ATLAS Collaboration, *ATLAS Magnet System: Magnet Project Technical Design Report, Volume 1*, ATLAS-TDR-6; CERN-LHCC-97-018, 1997.

[23] ATLAS Collaboration, *ATLAS Central Solenoid: Magnet Project Technical Design Report, Volume 4*, ATLAS-TDR-9; CERN-LHCC-97-021, 1997.

[24] ATLAS Collaboration, *ATLAS Insertable B-Layer: Technical Design Report*, ATLAS-TDR-19; CERN-LHCC-2010-013, 2010.

[25] ATLAS Collaboration, *ATLAS Liquid Argon Calorimeter: Technical Design Report*, ATLAS-TDR-2; CERN-LHCC-96-041, 1996.

[26] ATLAS Collaboration, *Readiness of the ATLAS liquid argon calorimeter for LHC collisions*, Eur. Phys. J. C 70:723, 2010, arXiv:0912.2642 [hep-ex].

[27] ATLAS Collaboration, *ATLAS Muon Spectrometer: Technical Design Report*, ATLAS-TDR-10; CERN-LHCC-97-022, 1997.

[28] ATLAS Collaboration, *ATLAS Barrel Toroid: Magnet Project Technical Design Report, Volume 2*, ATLAS-TDR-7; CERN-LHCC-97-019, 1997.

[29] ATLAS Collaboration, *ATLAS End-Cap Toroids: Magnet Project Technical Design Report, Volume 3*, ATLAS-TDR-8; CERN-LHCC-97-020, 1997.

[30] G. Avoni et al., *The new LUCID-2 detector for luminosity measurement and monitoring in ATLAS*, JINST 13 07:P07017, 2018.

[31] ATLAS Collaboration, *ATLAS Forward Proton Phase-I Upgrade: Technical Design Report*, ATLAS-TDR-024; CERN-LHCC-2015-009, 2015.

[32] A. Sopczak, *Overview of ATLAS Forward Proton (AFP) detectors in Run-2 and outlook for Run-3 analyses*, 2023, arXiv:2307.09780 [hep-ex].

[33] ATLAS Collaboration, *ATLAS Forward Detectors for Measurement of Elastic Scattering and Luminosity: Technical Design Report*, ATLAS-TDR-18; CERN-LHCC-2008-004, 2008.

[34] ATLAS Collaboration, *Performance of the ATLAS trigger system in 2015*, Eur. Phys. J. C 77:317, 2017, arXiv:1611.09661 [hep-ex].

[35] ATLAS Collaboration, *Operation of the ATLAS trigger system in Run 2*, JINST 15:P10004, 2020, arXiv:2007.12539 [hep-ex].

[36] ATLAS Collaboration, *The ATLAS Trigger System for LHC Run 3 and Trigger performance in 2022*, 2024, submitted to JINST, arXiv:2401.06630 [hep-ex].

[37] ATLAS Collaboration, *ATLAS Tile Calorimeter: Technical Design Report*, ATLAS-TDR-3; CERN-LHCC-96-042, 1996.

[38] ATLAS Collaboration, *Operation and performance of the ATLAS tile calorimeter in LHC Run 2*, 2024, arXiv:2401.16034 [hep-ex].

[39] ATLAS Collaboration, *Approved Tile Calorimeter Plots*, https://twiki.cern.ch/twiki/bin/view/AtlasPublic/ApprovedPlotsTile.

[40] P. Adragna et al., *A PMT-Block test bench*, Nuclear Instruments and Methods in Physics Research Section A: Accelerators, Spectrometers, Detectors and Associated Equipment 564 1:597–607, 2006, ISSN: 0168-9002.

[41] M. Crouau et al., *Characterization of 8-stages Hamamatsu R5900 photomultipliers for the TILE calorimeter*, ATL-TILECAL-97-129, ATL-L-PN-129, Geneva, 1997.

[42] K. Anderson et al., *Design of the front-end analog electronics for the ATLAS tile calorimeter*, Nuclear Instruments and Methods in Physics Research Section A: Accelerators, Spectrometers, Detectors and Associated Equipment 551 2:469–476, 2005, ISSN: 0168-9002.

[43] C. Berglund et al., *The ATLAS tile calorimeter digitizer*, ATL-TILECAL-PUB-2007-007, Geneva, 2008.

[44] ATLAS Collaboration, *Operation and performance of the ATLAS Tile Calorimeter in Run 1*, Eur. Phys. J. C 78:987, 2018, arXiv:1806 . 02129 [hep-ex].

[45] ATLAS Collaboration, *Testbeam studies of production modules of the ATLAS tile calorimeter*, Nucl. Instrum. Meth. A 606:362–394, 2009.

[46] ATLAS Collaboration, *Readiness of the ATLAS Tile Calorimeter for LHC collisions*, Eur. Phys. J. C 70:1193, 2010, arXiv:1007.5423 [hep-ex].

[47] G. Blanchot et al., *The Cesium source calibration and monitoring system of the ATLAS Tile Calorimeter: design, construction and results*, JINST 15 03:P03017, 2020.

[48] ATLAS Collaboration, *Laser calibration of the ATLAS Tile Calorimeter during LHC Run 2*, JINST 18:P06023, 2023, arXiv:2303.00121 [physics.ins-det].

[50] K. J. Anderson et al., *Calibration of ATLAS Tile Calorimeter at Electromagnetic Scale*, ATL-TILECAL-PUB-2009-001, Geneva, 2008.

[51] ATLAS Collaboration, *Selection of jets produced in* 13 *TeV proton–proton collisions with the ATLAS detector*, ATLAS-CONF-2015-029, 2015.

[52] C. Clément et al., *Time Calibration of the ATLAS Hadronic Tile Calorimeter using the Laser System*, ATL-TILECAL-PUB-2009-003, Geneva, 2008.

[53] ATLAS Collaboration, *Public Tile Calorimeter Plots for Collision Data*, https://twiki.cern.ch/twiki/bin/view/AtlasPublic/TileCaloPublicResults.

[54] T. Davídek and R. Leitner, *Elementární částice od prvních objevů po současné experimenty*, Matfyzpress, 2012, ISBN: 978-80-7378-205-4.

[55] W. Lampl et al., *Calorimeter Clustering Algorithms: Description and Performance*, ATL-LARG-PUB-2008-002, 2008.

[56] ATLAS Collaboration, *Topological cell clustering in the ATLAS calorimeters and its performance in LHC Run 1*, Eur. Phys. J. C 77:490, 2017, arXiv:1603.02934 [hep-ex].

[57] ATLAS Collaboration, *Jet energy scale and resolution measured in proton–proton collisions at* $\sqrt{s}$=13 *TeV with the ATLAS detector*, 2020, arXiv:2007.02645 [hep-ex].

[58] T. Barillari et al., *Local Hadronic Calibration*, ATL-LARG-PUB-2009-001-2, 2008.

[59] ATLAS Collaboration, *Determination of jet calibration and energy resolution in proton–proton collisions at $\sqrt{s} = 8$ TeV using the ATLAS detector*, Eur. Phys. J. C 80:1104, 2020, arXiv:1910.04482 [hep-ex].

[60] M. Cacciari, G. P. Salam, and G. Soyez, *The anti-k_t jet clustering algorithm*, JHEP 2008 04:063, 2008.

[61] M. Cacciari, G. P. Salam, and G. Soyez, http://fastjet.fr/.

[62] M. Cacciari, G. P. Salam, and G. Soyez, *FastJet user manual: (for version 3.0.2)*, Eur. Phys. J. C 72 3 , 2012, ISSN: 1434-6052.

[63] ATLAS Collaboration, *Jet reconstruction and performance using particle flow with the ATLAS Detector*, Eur. Phys. J. C 77:466, 2017, arXiv:1703.10485 [hep-ex].

[64] ATLAS Collaboration, *Jet energy scale measurements and their systematic uncertainties in proton–proton collisions at $\sqrt{s} = 13$ TeV with the ATLAS detector*, Phys. Rev. D 96:072002, 2017, arXiv:1703.09665 [hep-ex].

[65] M. Cacciari and G. P. Salam, *Pileup subtraction using jet areas*, Physics Letters B 659 1:119–126, 2008, ISSN: 0370-2693.

[66] ATLAS Collaboration, *Data-driven determination of the energy scale and resolution of jets reconstructed in the ATLAS calorimeters using dijet and multijet events at $\sqrt{s} = 8$ TeV*, ATLAS-CONF-2015-017, 2015.

[67] ATLAS Collaboration, *Determination of the jet energy scale and resolution at ATLAS using Z/γ-jet events in data at $\sqrt{s} = 8$ TeV*, ATLAS-CONF-2015-057, 2015.

[68] ATLAS Collaboration, *TeV-scale jet energy calibration using multijet events including close-by jet effects at the ATLAS experiment*, ATLAS-CONF-2013-003, 2013.

[69] B. Malaescu, *An iterative, dynamically stabilized method of data unfolding*, 2009, arXiv:0907.3791 [physics.data-an].

[70] B. Malaescu, *An Iterative, Dynamically Stabilized (IDS) Method of Data Unfolding*, 2011, arXiv:1106.3107 [physics.data-an].

[71] ATLAS Collaboration, *Measurement of inclusive jet and dijet cross sections in proton–proton collisions at 7 TeV centre-of-mass energy with the ATLAS detector*, Eur. Phys. J. C 71:1512, 2011, arXiv:1009.5908 [hep-ex].

[72] ATLAS Collaboration, *Measurement of inclusive jet and dijet cross-sections in proton–proton collisions at $\sqrt{s} = 13$ TeV with the ATLAS detector*, JHEP 05:195, 2018, arXiv:1711.02692 [hep-ex].

[73] ATLAS Collaboration, *Luminosity determination in pp collisions at $\sqrt{s} = 13$ TeV using the ATLAS detector at the LHC*, ATLAS-CONF-2019-021, 2019.

[74] ATLAS Collaboration, *ATLAS data quality operations and performance for 2015–2018 data-taking*, JINST 15:P04003, 2020, arXiv:1911.04632 [physics.ins-det].

[75] R. D. Ball et al., *Parton distributions with LHC data*, Nucl. Phys. B 867:244, 2013, arXiv:1207.1303 [hep-ph].

[76] ATLAS Collaboration, *ATLAS Pythia 8 tunes to 7 TeV data*, ATL-PHYS-PUB-2014-021, 2014.

[77] T. Sjöstrand and P. Skands, *Transverse-momentum-ordered showers and interleaved multiple interactions*, Eur. Phys. J. C 39 2:129–154, 2005, ISSN: 1434-6052.

[78] T. Sjöstrand and P. Skands, *Multiple Interactions and the Structure of Beam Remnants*, JHEP 2004 03:053–053, 2004, ISSN: 1029-8479.

[79] ATLAS Collaboration, *The ATLAS Simulation Infrastructure*, Eur. Phys. J. C 70:823, 2010, arXiv:1005.4568 [physics.ins-det].

[80] GEANT4 Collaboration, S. Agostinelli, et al., *Geant4 – a simulation toolkit*, Nucl. Instrum. Meth. A 506:250, 2003.

[81] ATLAS Collaboration, *Measurements of jet cross-section ratios in 13 TeV proton–proton collisions with ATLAS*, 2024, arXiv:2405.20206 [hep-ex].

[82] ATLAS Collaboration, *Measurement of the energy response of the ATLAS calorimeter to charged pions from $W^{\pm} \to \tau^{\pm}(\to \pi^{\pm}\nu_{\tau})\nu_{\tau}$ events in Run 2 data*, Eur. Phys. J. C 82:223, 2022, arXiv:2108.09043 [hep-ex].

[83] ATLAS Collaboration, *Luminosity determination in pp collisions at $\sqrt{s} = 13$ TeV using the ATLAS detector at the LHC*, Eur. Phys. J. C 83:982, 2023, arXiv:2212.09379 [hep-ex].

List of figures

List of tables

List of abbreviations

ADC analog-to-digital converter.

AFP ATLAS Forward Proton.

ALFA Absolute Luminosity For ATLAS.

ALTI ATLAS Local Trigger Interface.

ATLAS A Toroidal LHC ApparatuS.

BCO bunch-crossing offset.

CIS charge injection system.

DGLAP Dokshitzer–Gribov–Lipatov–Altarelli–Parisi.

DMU data management unit.

DSP digital signal processor.

EM electromagnetic.

EMB Electromagnetic Barrel.

EMEC Electromagnetic End-Cap.

EW electroweak.

FCal Forward Calorimeter.

GSC global sequential calibration.

HEC Hadronic End-Cap.

HG high gain.

HLT High-Level Trigger.

IBL insertable B-layer.

ID Inner Detector.

IDS Iterative, Dynamically Stabilized.

IP interaction point.

IR infrared.

JER jet energy resolution.

JES jet energy scale.

JVT jet vertex tagger.

KLN Kinoshita–Lee–Nauenberg.

L1 Level-1.

LAr Liquid Argon Calorimeter.

LB luminosity block.

LCW local cluster weighting.

LG low gain.

LHC Large Hadron Collider.

Linac2 Linear accelerator 2.

LO leading order.

LUCID LUminosity Cherenkov Integrating Detector.

MB minimum bias.

MC Monte Carlo.

MJB multijet balance.

MS Muon Spectrometer.

NP nuisance parameter.

NPV number of primary vertices.

OF optimal filtering.

PDF parton distribution function.

PFlow particle flow.

PMT photomultiplier tube.

p*–*p proton–proton.

pQCD perturbative QCD.

PS Proton Synchrotron.

PSB Proton Synchrotron Booster.

PV primary vertex.

QCD quantum chromodynamics.

RM response matrix.

RMS root mean square.

ROD readout driver.

SCT Semiconductor Tracker.

SM Standard Model of particle physics.

SPS Super Proton Synchrotron.

TileCal Tile Calorimeter.

Topo topological.

topocluster topological cluster.

TRT Transition Radiation Tracker.

TTC timing, trigger, and control.

TTCrx TTC receiver chip.

UV ultraviolet.

WLS wavelength-shifting.

ZDC Zero Degree Calorimeter.

List of publications

Papers:
ATLAS Collaboration, *Operation and performance of the ATLAS tile calorimeter in LHC Run 2*, 2024, submitted to Eur. Phys. J. C, arXiv:2401.16034 [hep-ex].

ATLAS Collaboration, *Laser calibration of the ATLAS Tile Calorimeter during LHC Run 2*, JINST 18:P06023, 2023, arXiv:2303.00121 [physics.ins-det].

Conference proceedings:
S. Poláček, *Performance of the ATLAS Tile Calorimeter*, 2024, submitted to PoS.

S. Poláček, *Time calibration and monitoring in the ATLAS Tile Calorimeter*, PoS PANIC2021:106, 2022.

A. Time calibration of the ATLAS Tile Calorimeter

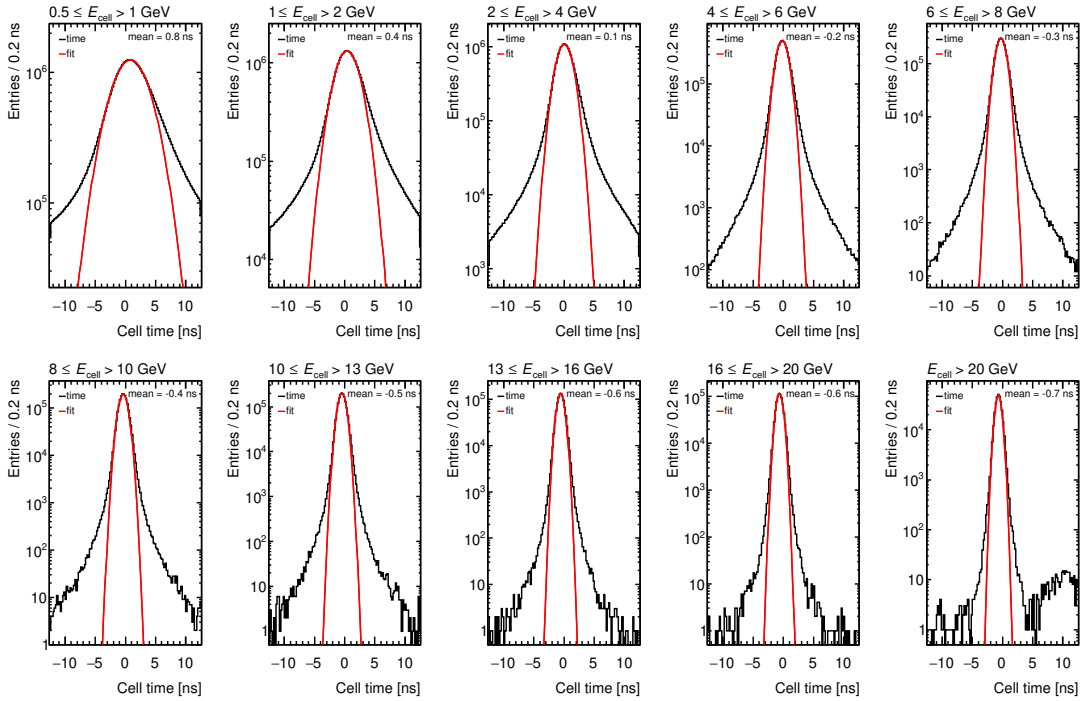

Figure A.1: Examples of TileCal cell reconstructed time distributions (black line) in different E_{cell} energy bins fitted by a Gaussian function (red line). The Gaussian mean is displayed.

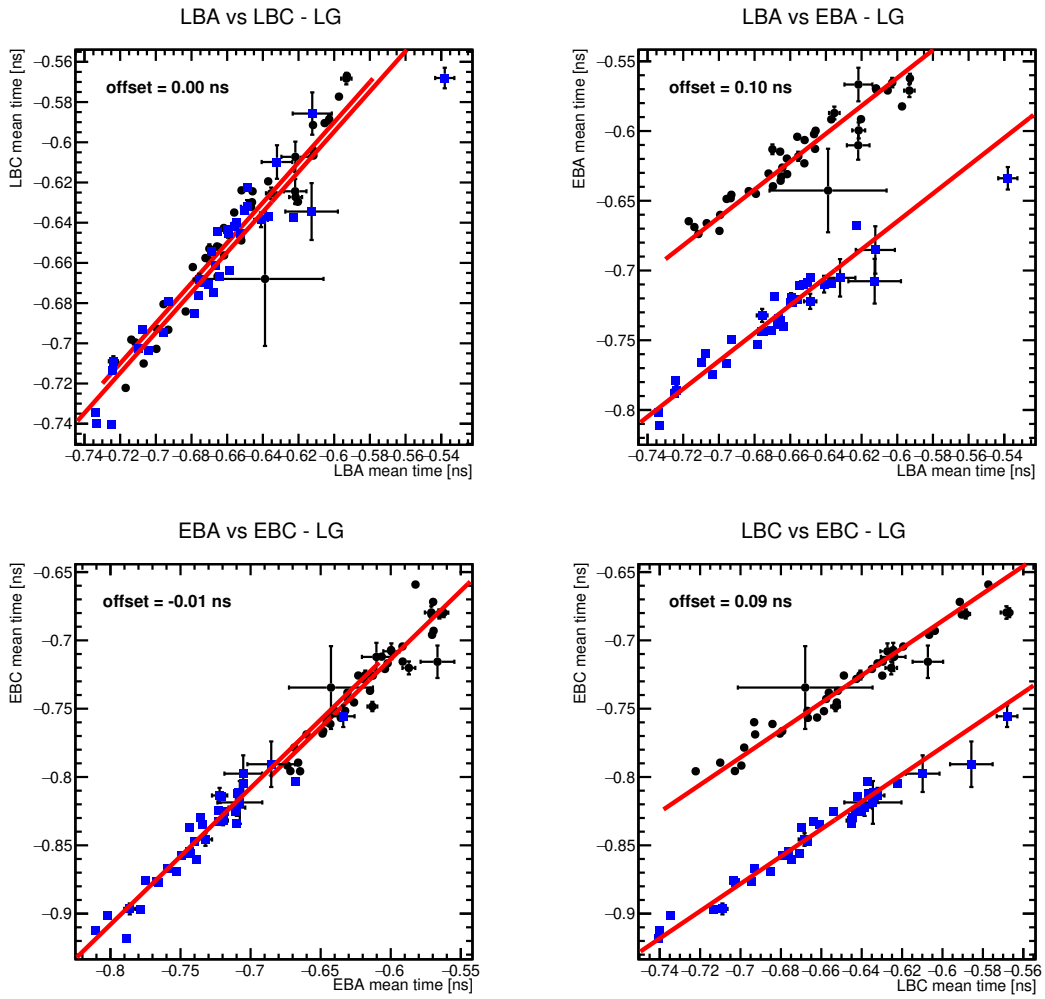

Figure A.2: The mean partition time in the LG comparing (top left) LBA and LBC, (top right) LBA and EBA, (bottom left) EBA and EBC, and (bottom right) LBC and EBC. Two groups of runs (black circles, blue squares) are fitted by a one-parametric linear function (red line) with a slope equal to one. A displayed difference in the fit parameters of the two run groups shows approximately 0.1 ns offset comparing long and extended barrels. A set of 2023 13.6 TeV p–p collision runs is used.

B. The dijet cross-section measurement

Table B.1: The dijet cross-section m_{jj} binning in all six y^* bins.

	m_{jj} binning [GeV]
$y^* < 0.5$	40, 240, 270, 300, 340, 380, 420, 460, 500, 540, 580, 630, 680, 730, 780, 830, 890, 950, 1010, 1070, 1140, 1210, 1280, 1350, 1430, 1510, 1590, 1670, 1760, 1850, 1940, 2040, 2140, 2240, 2350, 2460, 2580, 2700, 2820, 2950, 3080, 3220, 3360, 3510, 3660, 3820, 3990, 4160, 4340, 4530, 4730, 4940, 5160, 5390, 5630, 5880, 6140, 6420, 6710, 8100
$0.5 \leq y^* < 1.0$	110, 280, 320, 360, 400, 450, 500, 550, 600, 650, 700, 760, 820, 880, 940, 1010, 1080, 1150, 1220, 1300, 1380, 1460, 1550, 1640, 1730, 1830, 1930, 2030, 2140, 2250, 2370, 2490, 2620, 2750, 2890, 3030, 3180, 3330, 3490, 3650, 3820, 4000, 4180, 4370, 4570, 4770, 4980, 5200, 5420, 5650, 5890, 6140, 6400, 6670, 6950, 8260
$1.0 \leq y^* < 1.5$	250, 390, 450, 510, 570, 630, 700, 770, 840, 910, 990, 1070, 1150, 1240, 1330, 1420, 1520, 1620, 1720, 1830, 1940, 2060, 2180, 2310, 2440, 2580, 2730, 2880, 3040, 3210, 3380, 3560, 3750, 3950, 4160, 4380, 4610, 4850, 5100, 5360, 5640, 5930, 6240, 6570, 6910, 7280, 9650
$1.5 \leq y^* < 2.0$	450, 600, 690, 790, 890, 990, 1090, 1200, 1310, 1420, 1540, 1660, 1790, 1920, 2060, 2200, 2350, 2500, 2660, 2830, 3010, 3190, 3380, 3580, 3780, 4000, 4230, 4470, 4720, 4980, 5250, 5540, 5840, 6160, 6500, 6870, 7280, 9280
$2.0 \leq y^* < 2.5$	730, 960, 1110, 1260, 1410, 1560, 1720, 1890, 2060, 2240, 2420, 2610, 2810, 3020, 3240, 3470, 3700, 3950, 4200, 4470, 4750, 5040, 5350, 5650, 5970, 6320, 6720, 7060, 7410, 9740
$2.5 \leq y^* < 3.0$	1220, 1570, 1830, 2100, 2390, 2680, 3000, 3320, 3640, 3970, 4340, 4710, 5160, 5620, 6070, 6570, 7420, 10000

Table B.2: The dijet cross-section m_{jj} binning in all six y_{boost} bins.

	m_{jj} binning [GeV]
$y_{\mathrm{boost}} < 0.5$	40, 240, 280, 320, 370, 420, 480, 540, 610, 690, 770, 860, 960, 1070, 1190, 1330, 1480, 1650, 1840, 2040, 2250, 2470, 2700, 2940, 3190, 3450, 3720, 4010, 4310, 4620, 4960, 5300, 5650, 6010, 6400, 6910, 7480, 10000
$0.5 \leq y_{\mathrm{boost}} < 1.0$	40, 240, 280, 320, 370, 420, 470, 530, 590, 660, 740, 830, 930, 1040, 1160, 1290, 1430, 1570, 1710, 1860, 2020, 2190, 2360, 2540, 2730, 2930, 3140, 3360, 3600, 3860, 4130, 4410, 4720, 5030, 5370, 7550
$1.0 \leq y_{\mathrm{boost}} < 1.5$	40, 250, 290, 330, 370, 420, 470, 530, 600, 670, 750, 830, 910, 1000, 1090, 1190, 1290, 1390, 1500, 1610, 1730, 1860, 1990, 2130, 2280, 2440, 2610, 2790, 2980, 3190, 3410, 3620, 4900
$1.5 \leq y_{\mathrm{boost}} < 2.0$	40, 240, 280, 320, 360, 410, 460, 510, 570, 630, 690, 750, 820, 890, 960, 1040, 1120, 1200, 1290, 1380, 1480, 1580, 1690, 1810, 1940, 2090, 2250, 3280
$2.0 \leq y_{\mathrm{boost}} < 2.5$	40, 240, 280, 320, 360, 400, 440, 490, 540, 590, 640, 690, 750, 810, 880, 950, 1020, 1100, 1190, 1290, 1440, 1800
$2.5 \leq y_{\mathrm{boost}} < 3.0$	40, 240, 280, 320, 360, 400, 440, 490, 540, 590, 640, 700, 760, 830, 1070

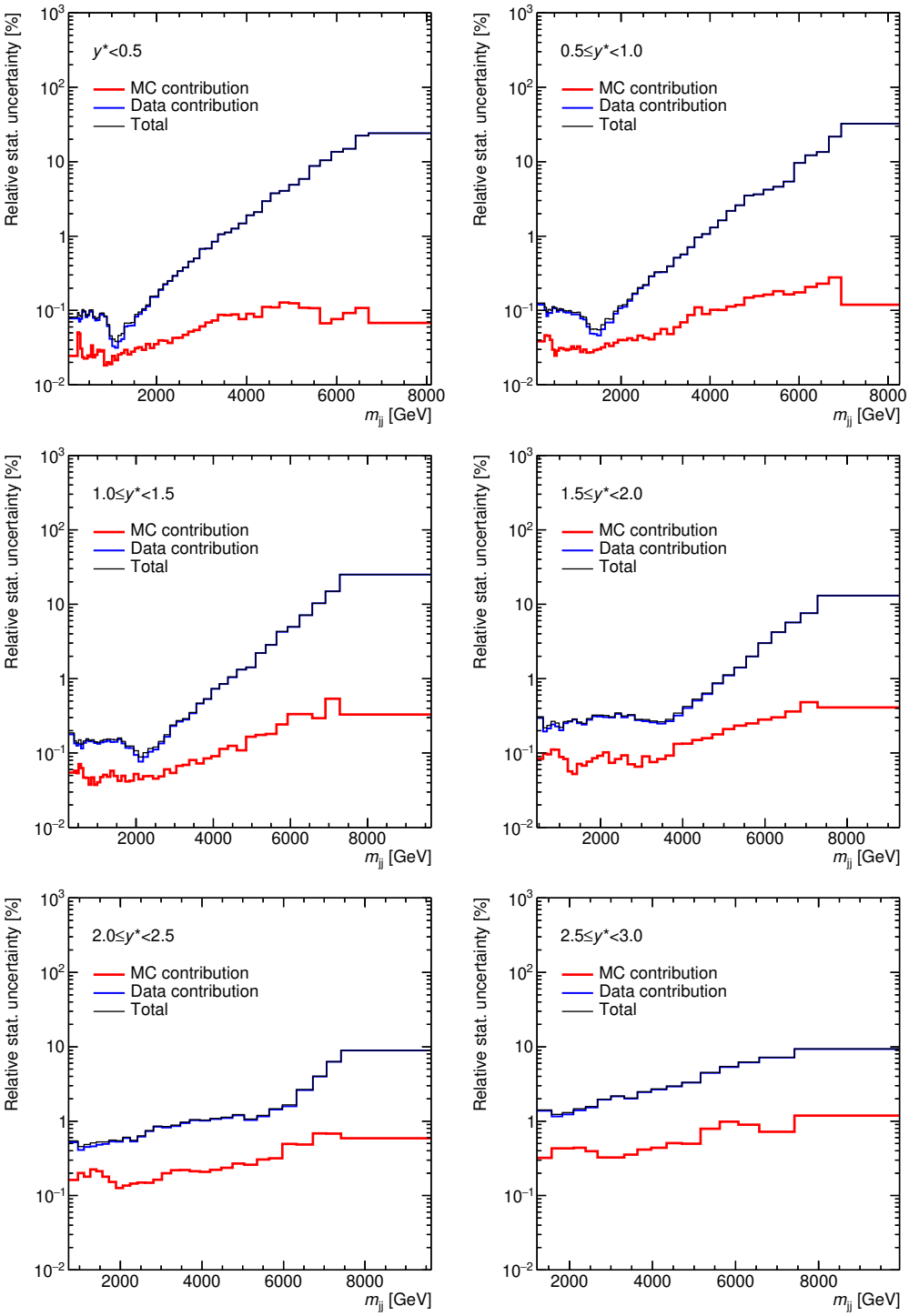

Figure B.1: The statistical uncertainty corresponding to the MC (MC contribution), data (Data contribution), and total uncertainty (Total) using the IDS unfolding method in all six y^* bins.

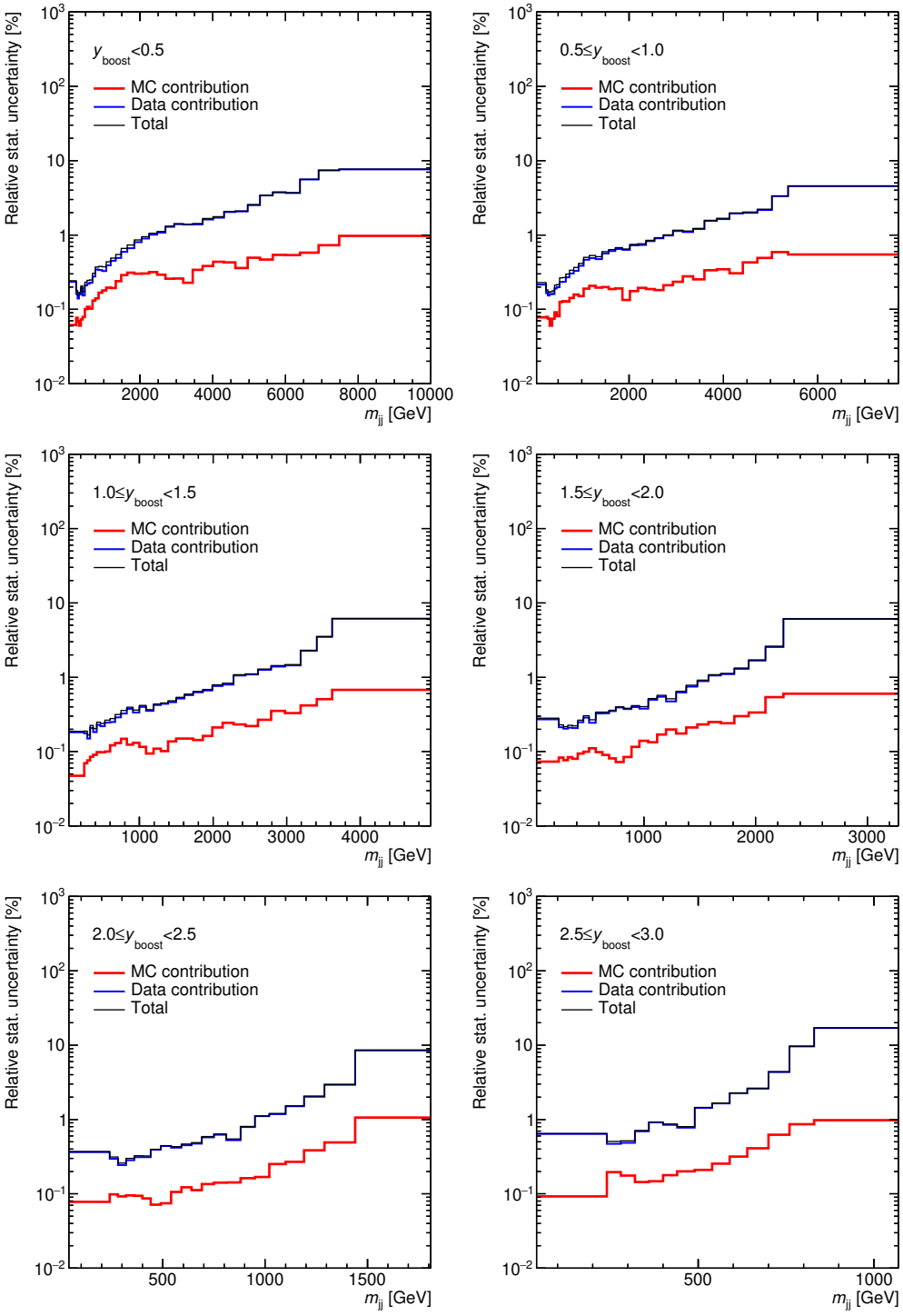

Figure B.2: The statistical uncertainty corresponding to the MC (MC contribution), data (Data contribution), and total uncertainty (Total) using the IDS unfolding method in all six y_{boost} bins.

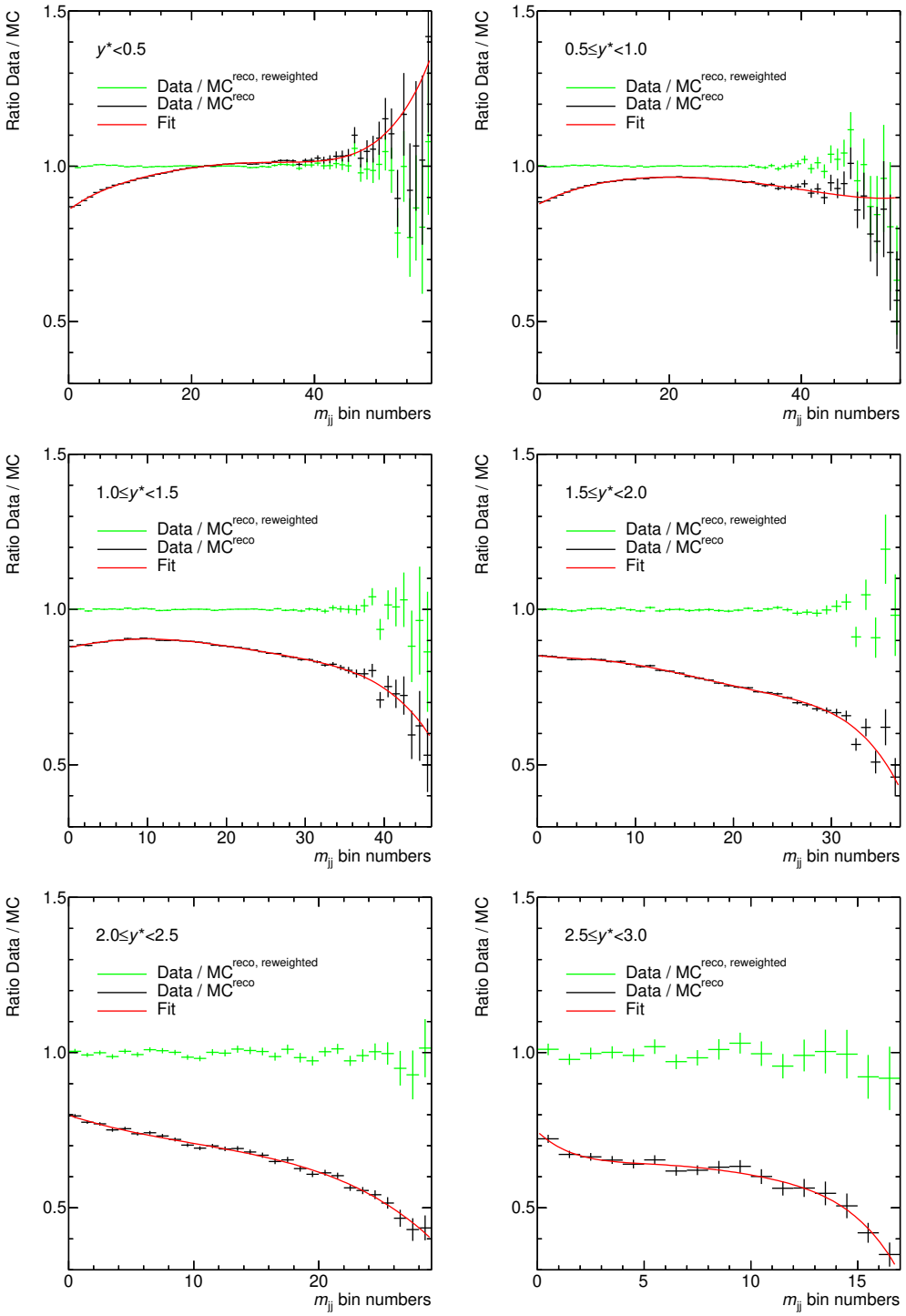

Figure B.3: The ratio of the data and MC on the reconstructed level (Data / MC$^{\text{reco}}$) fitted by a smooth function (Fit) and the ratio of the data and reweighted MC (Data / MC$^{\text{reco, reweighted}}$) in all six y^* bins.

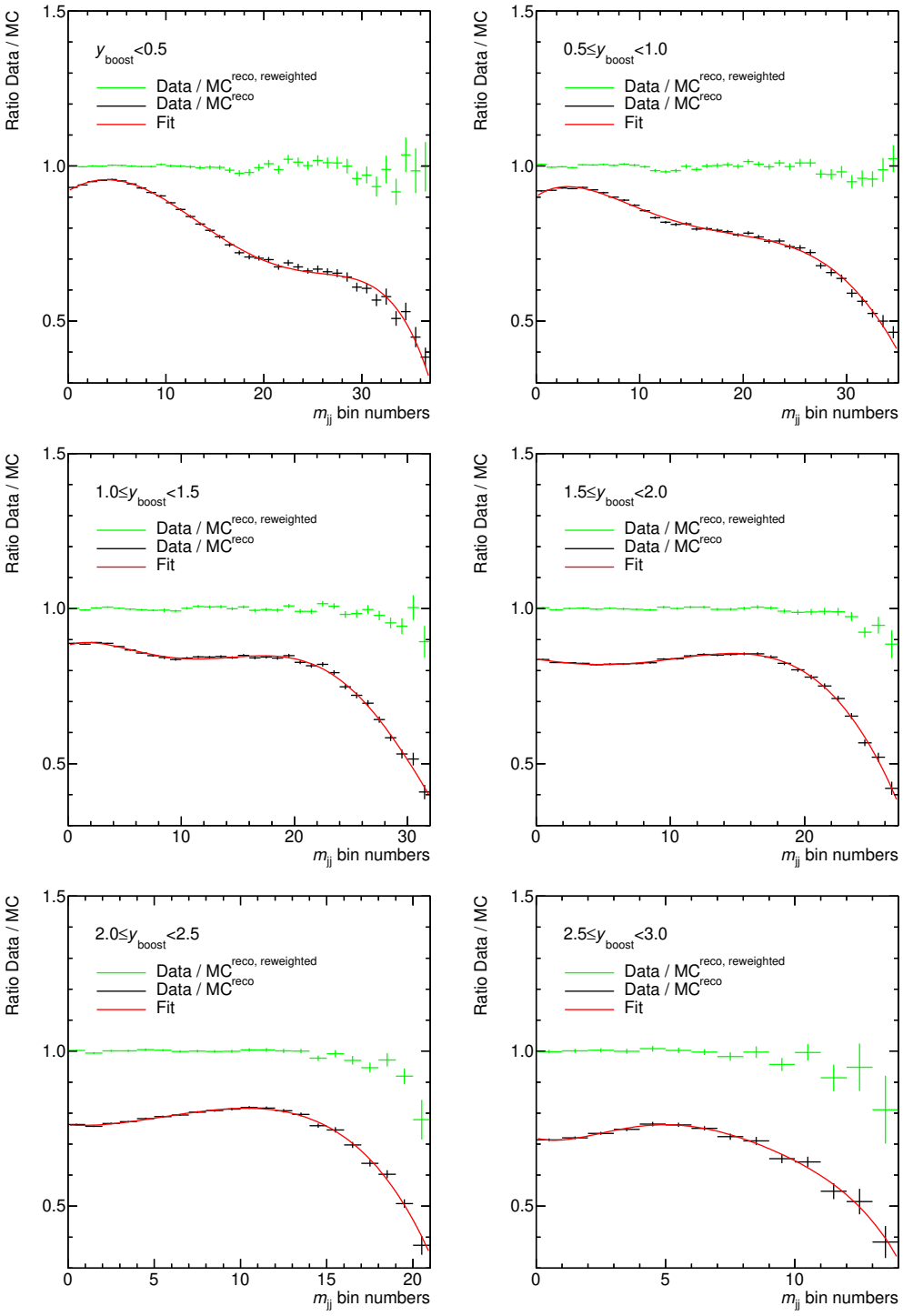

Figure B.4: The ratio of the data and MC on the reconstructed level (Data / MC$^{\mathrm{reco}}$) fitted by a smooth function (Fit) and the ratio of the data and reweighted MC (Data / MC$^{\mathrm{reco,\ reweighted}}$) in all six y_{boost} bins.

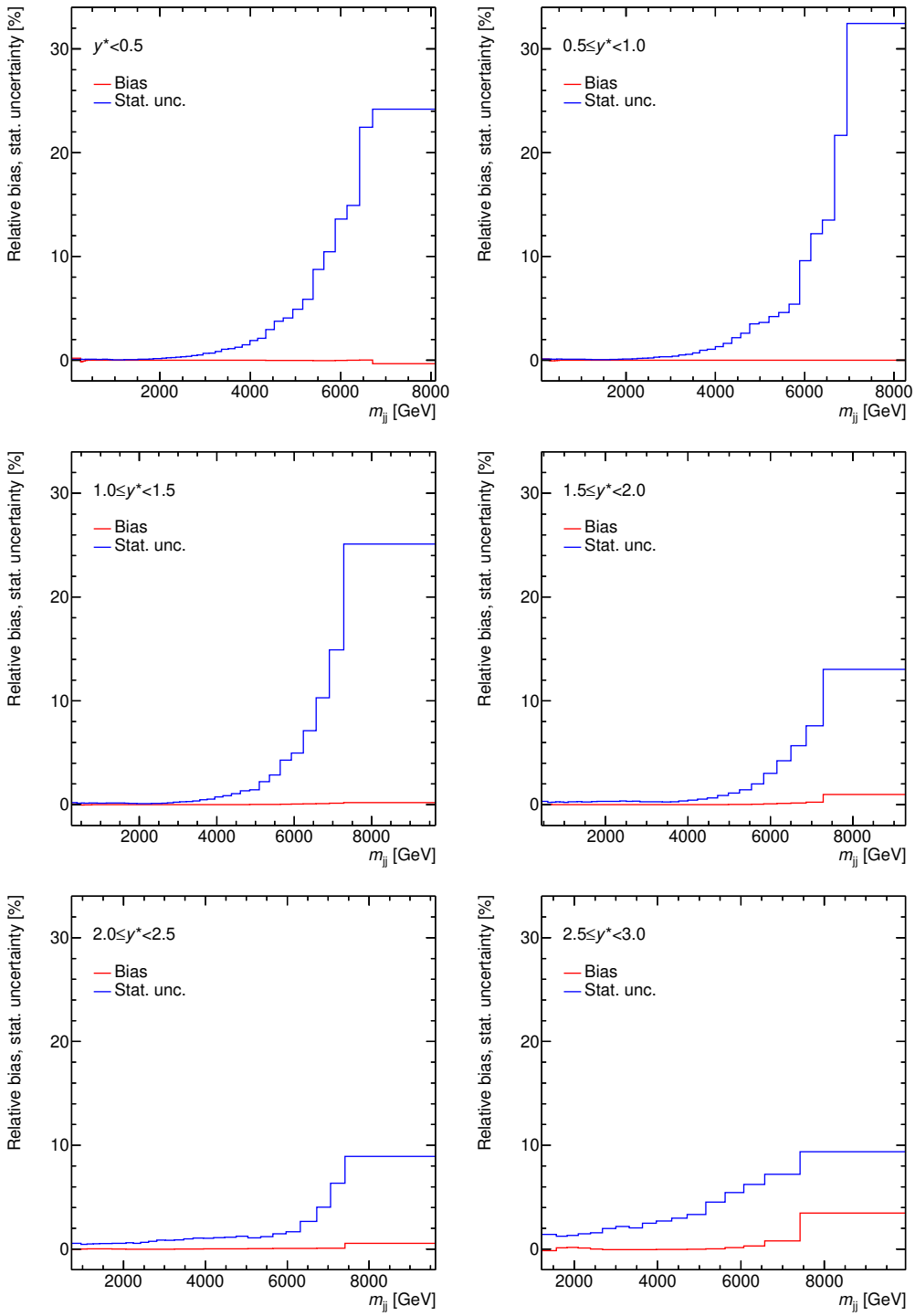

Figure B.5: Comparison of the smoothed unfolding bias estimate (Bias) and the unfolded spectra statistical uncertainty (Stat. unc.) using the IDS unfolding method in all six y^* bins.

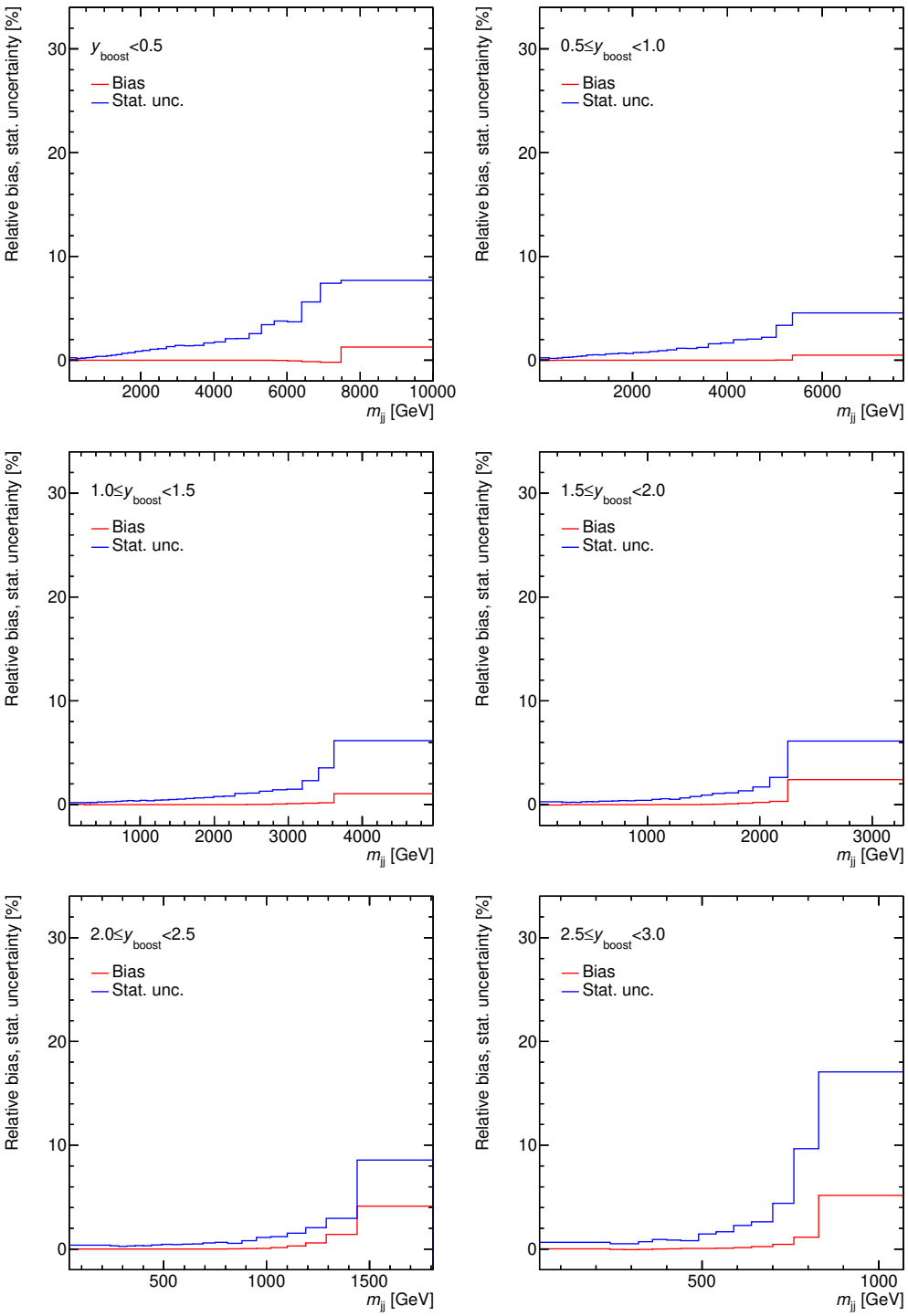

Figure B.6: Comparison of the smoothed unfolding bias estimate (Bias) and the unfolded spectra statistical uncertainty (Stat. unc.) using the IDS unfolding method in all six y_{boost} bins.

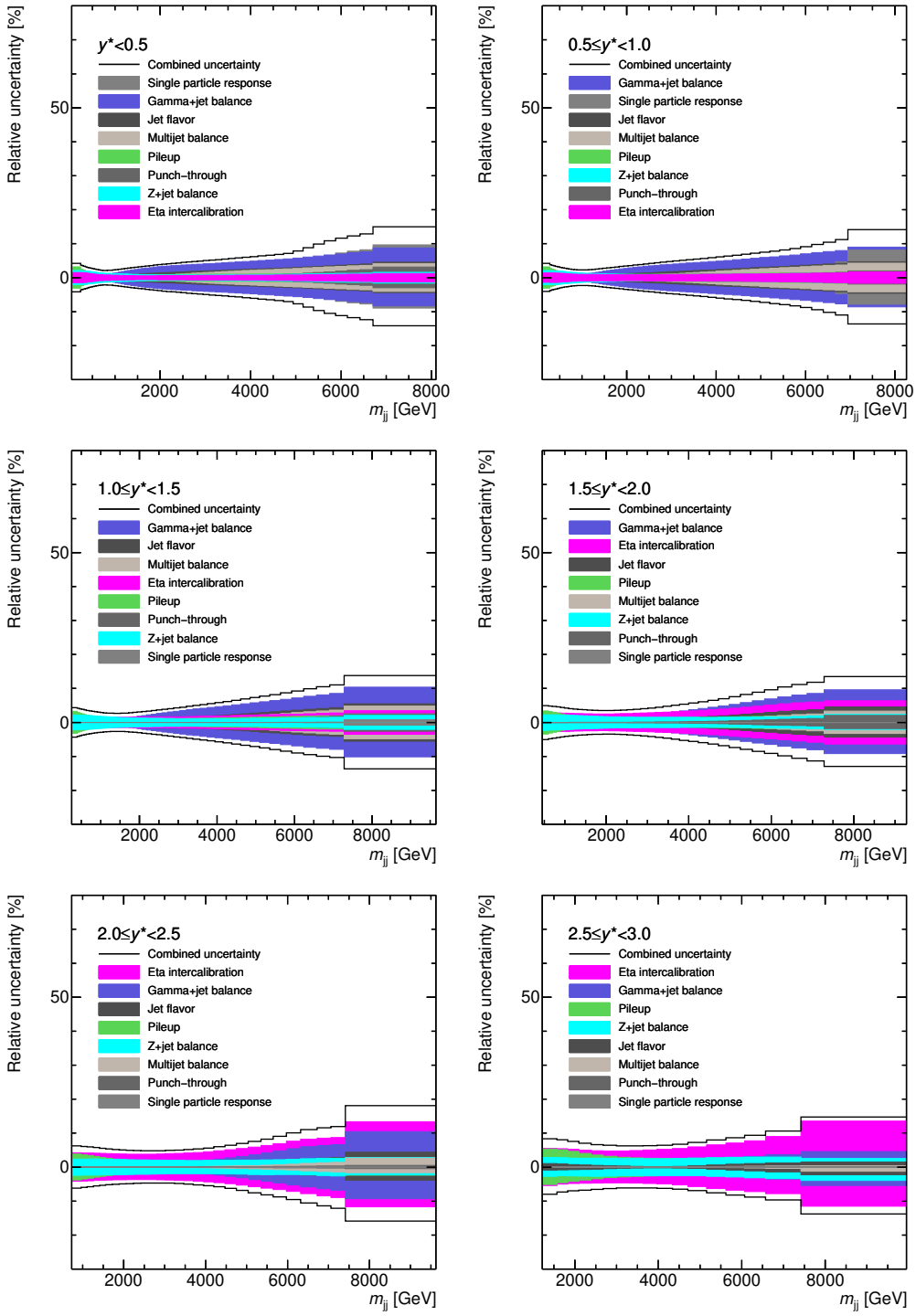

Figure B.7: Components of the JES uncertainty of the dijet cross-section in all six y^* bins.

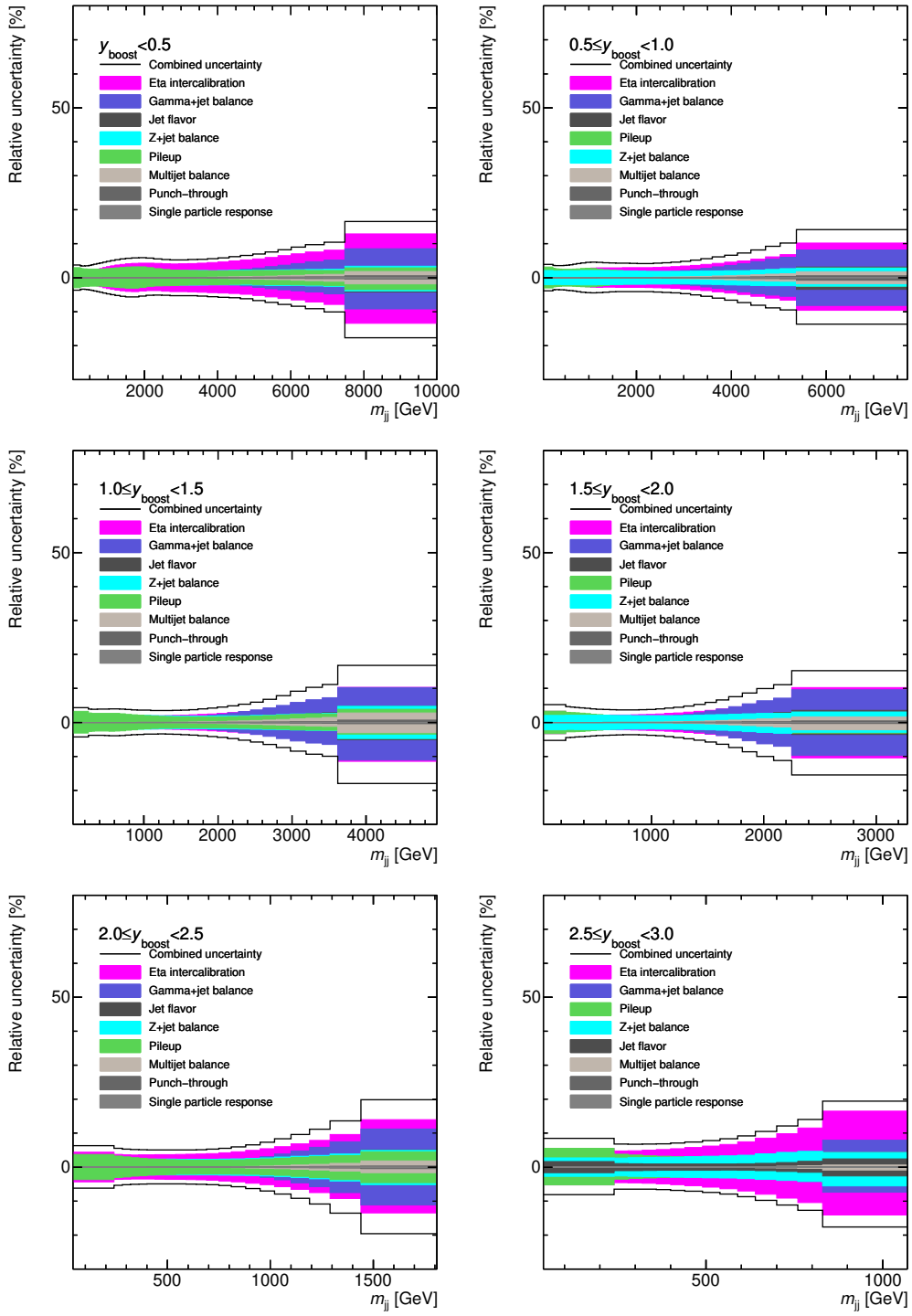

Figure B.8: Components of the JES uncertainty of the dijet cross-section in all six y_{boost} bins.

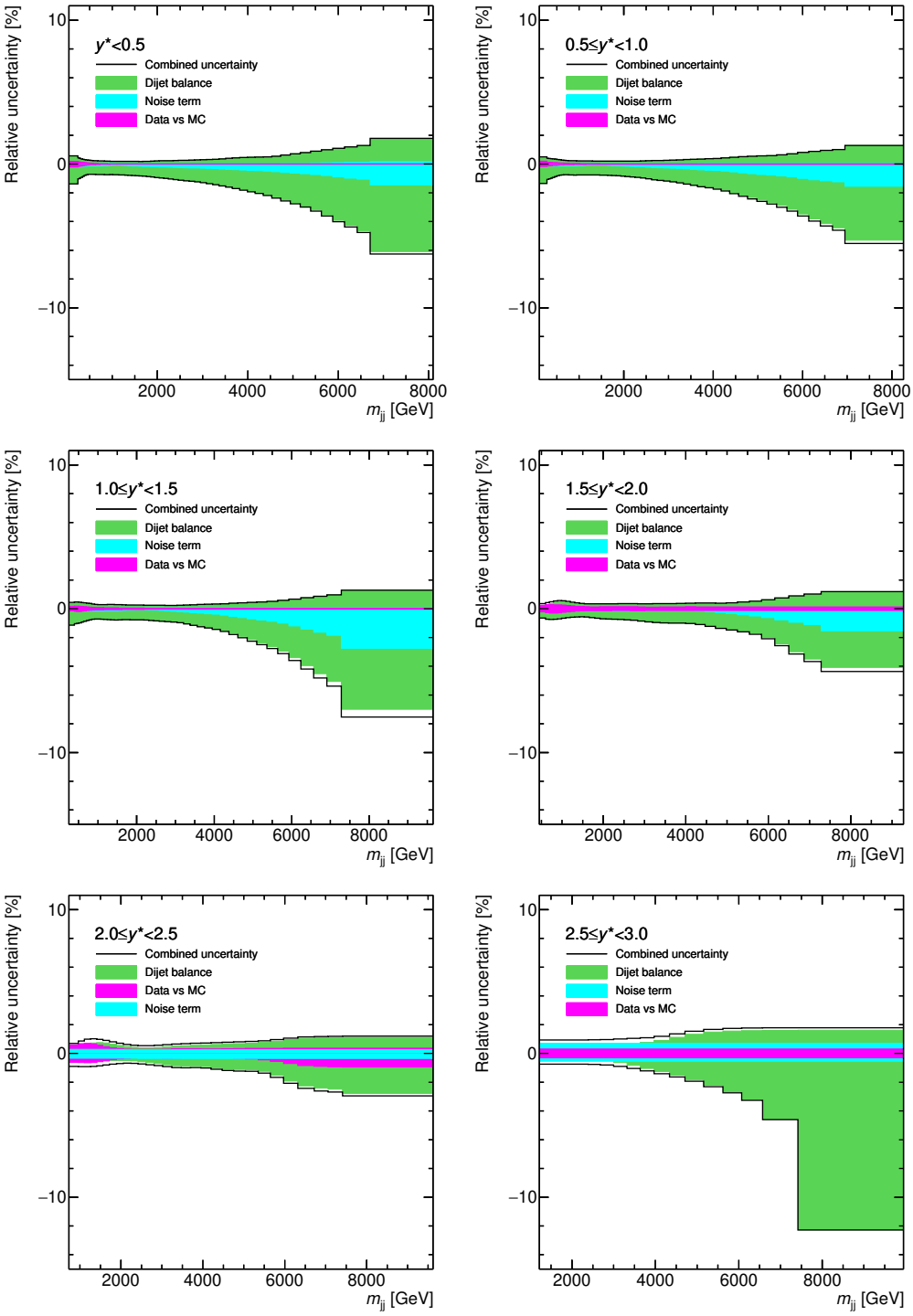

Figure B.9: Components of the JER uncertainty of the dijet cross-section in all six y^* bins.

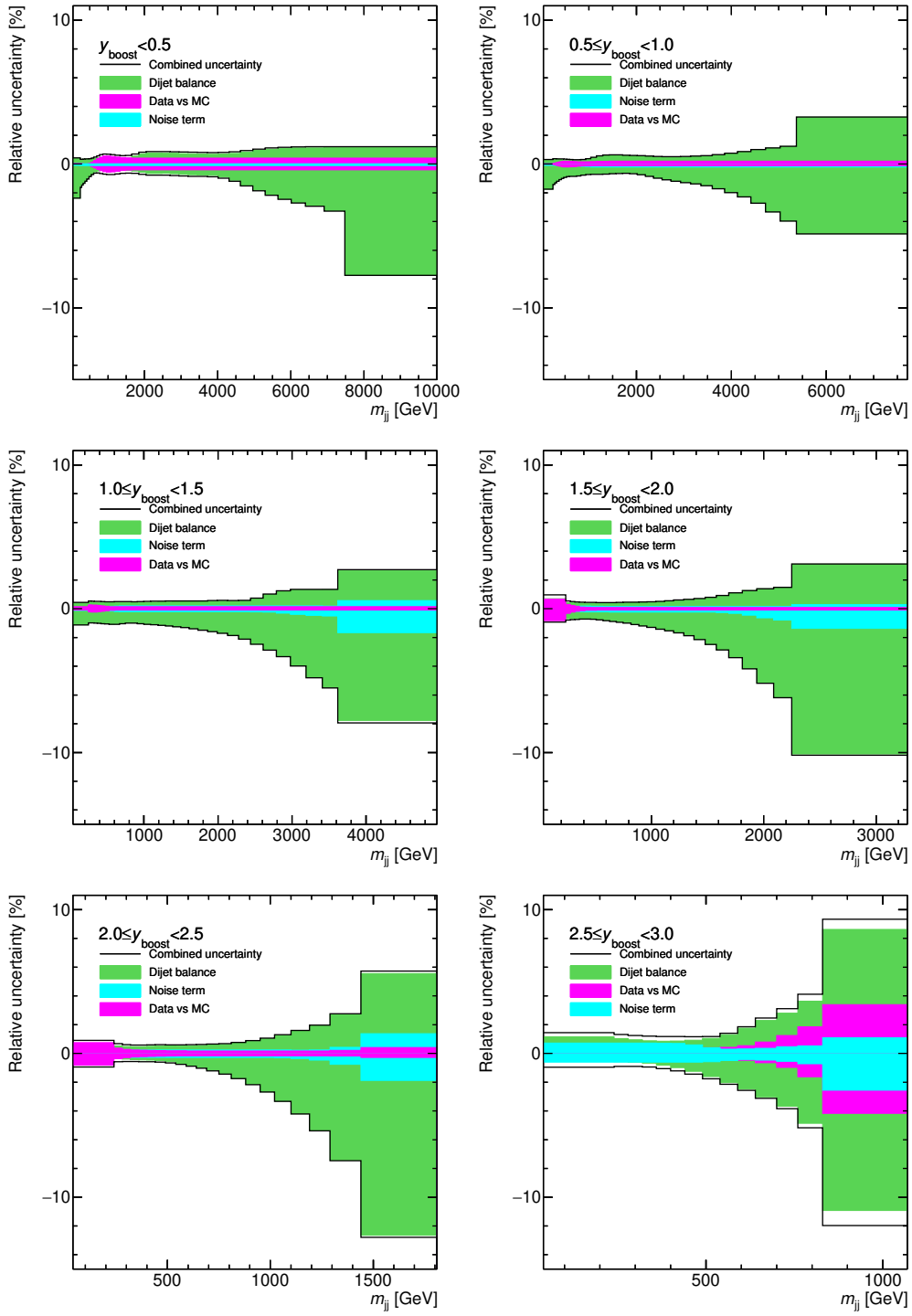

Figure B.10: Components of the JER uncertainty of the dijet cross-section in all six y_{boost} bins.

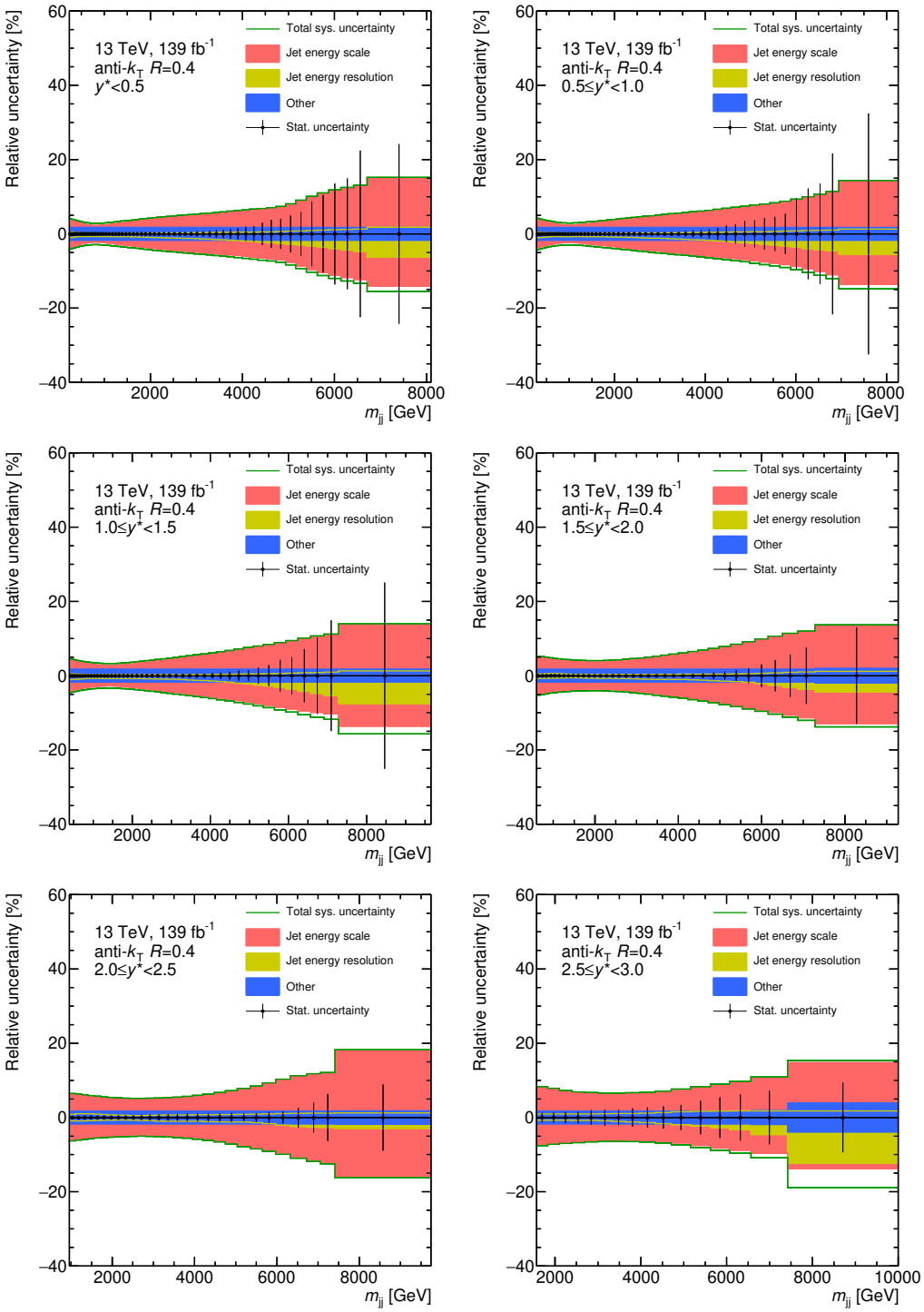

Figure B.11: Components of the total systematic uncertainty (color bands) and the total statistical uncertainty (black points) of the dijet cross-section in all six y^* bins.

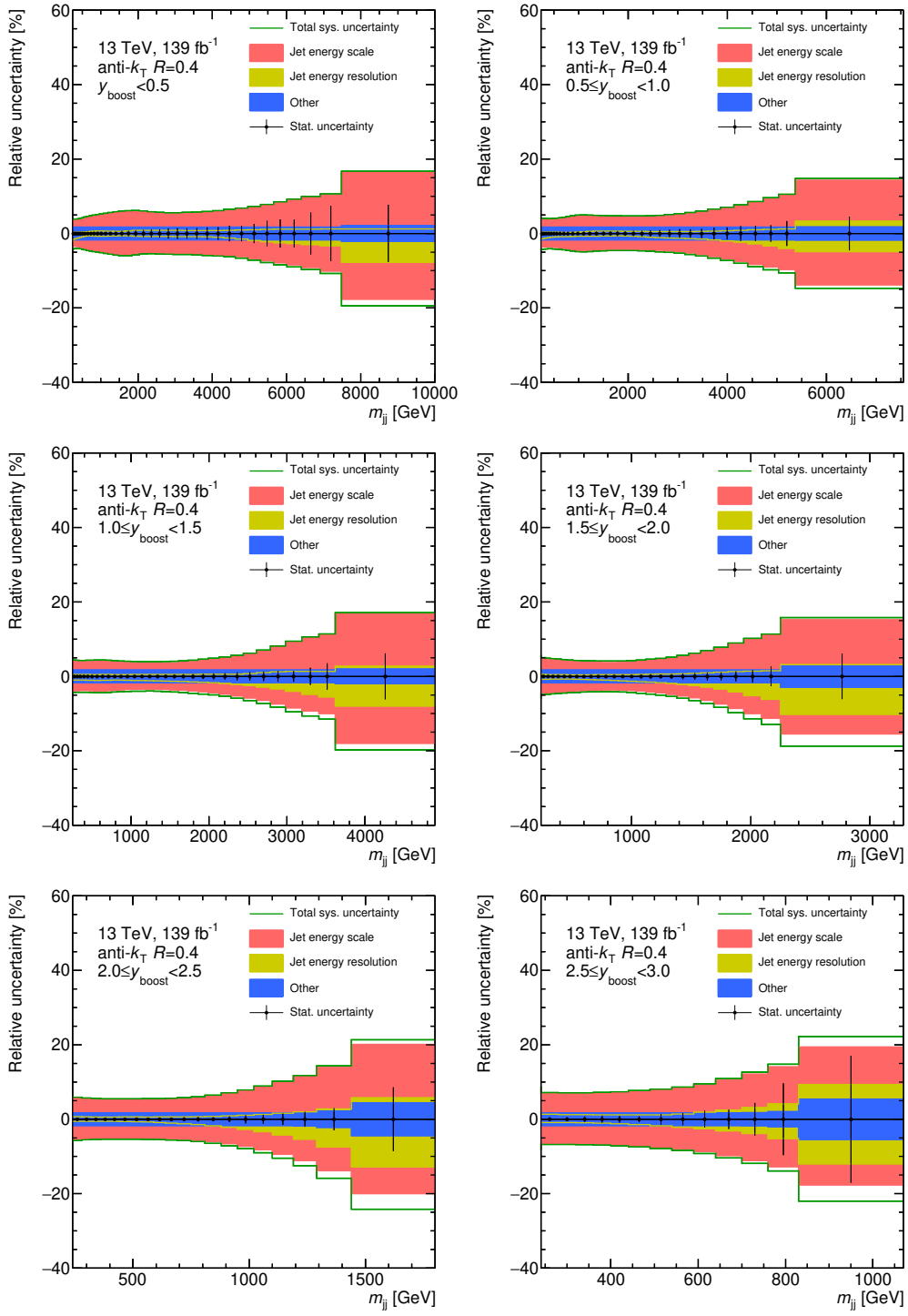

Figure B.12: Components of the total systematic uncertainty (color bands) and the total statistical uncertainty (black points) of the dijet cross-section in all six y_{boost} bins.